TOWARD AN IMPROVED METHOD FOR DETERMINING THE HAMAKER CONSTANT OF SOLID MATERIALS USING ATOMIC FORCE MICROSCOPY

by

Michael C. Stevenson

A Dissertation

Submitted to the Faculty of Purdue University

In Partial Fulfillment of the Requirements for the degree of

Doctor of Philosophy

Davidson School of Chemical Engineering

West Lafayette, Indiana

December 2021

THE PURDUE UNIVERSITY GRADUATE SCHOOL
STATEMENT OF COMMITTEE APPROVAL

Dr. David S. Corti, Co-Chair
Davidson School of Chemical Engineering

Dr. Stephen P. Beaudoin, Co-Chair
Davidson School of Chemical Engineering

Dr. Brett M. Savoie
Davidson School of Chemical Engineering

Dr. Helen A. McNally
School of Engineering Technology, Birck Nanotechnology Center

Approved by:
Dr. John A. Morgan

Dedicated to my wife Caralyn

ACKNOWLEDGMENTS

There are several people whom I would like to acknowledge as this work would not have been possible without their help. I would first like to thank Dr. David Corti and Dr. Stephen Beaudoin for their guidance throughout my four years at Purdue. I would also like to thank those in Dr. Beaudoin's research group whom I would often turn to for help along the way. I would also like to thank Purdue University and the Davidson School of Chemical Engineering for giving me the opportunity to grow as a researcher and help me achieve my goal of obtaining a PhD. Finally, I would like to thank my parents and brother for their support and encouragement.

Last but not least, I would like to thank my wife Caralyn to whom this dissertation is dedicated. You were with me every step of the way at Purdue, and I know I could have never gotten this far without you.

TABLE OF CONTENTS

LIST OF TABLES

LIST OF FIGURES

ABSTRACT

Particle adhesion plays a significant role in a wide range of industries and applications including pharmaceuticals, semiconductors, explosive detection systems, and the processing of bulk solid materials. For neutrally charged materials, particle adhesion arises primarily due to the dominate attractive van der Waals (vdW) force; the study of vdW forces is of particular interest because they are always present in a system. The strength of the vdW force between a pair of interacting materials is quantified by the Hamaker constant, A. Several theoretical and experimental techniques have been developed to quantify the Hamaker constant of a material including Lifshitz theory, the surface force apparatus, centrifuge technique, contact angle goniometer, and atomic force microscope (AFM). The AFM is of particular interest because it can be used to accurately measure electrostatic attraction, liquid bridging, and vdW interactions across a broad range of solid materials at the nanometer length scale. The development of a new AFM-based method for determining the Hamaker constant of solid materials is the focus of this work.

Several AFM-based methods have been proposed to estimate the Hamaker constant of a solid material, each using different parts of the AFM deflection curve which is generated from an AFM force experiment. In particular, for the approach-to-contact region of the deflection curve, previous work established a connection between the Hamaker constant and the deflection of the cantilever at first contact with the surface, d_c. While d_c is well-defined experimentally, the estimation of A from the (average) value of d_c, although consistent with known results, was nonetheless found to introduce a significant degree of uncertainty in the reported value. Inherent material surface roughness has since been shown to be the primary reason for this large uncertainty. Thus, the overall goal of this work is to develop an updated approach-to-contact method to directly account for material surface roughness, thereby providing accurate estimates of the Hamaker constant with a significant reduction in uncertainty for a broad range of solid materials.

First, a novel vdW force model is derived describing the interaction between an AFM cantilever, treated as an effective sphere, and a surface of arbitrary roughness. The underlying material surface geometry and surface roughness is modeled directly using a surface height function, such that the vdW force is computed using the new expression over the full domain of the surface. Then, d_c is determined for any point along the surface from the limit of stability of the cantilever, or critical point, as it approaches the surface. Because of surface roughness,

different values of d_c will be obtained as the tip accesses separate surface positions. As such, a characteristic distribution of d_c-values, or a d_c-distribution, is observed for a given surface, providing a signature of the underlying surface roughness. A study is completed to understand the effects of surface geometry on the resulting d_c-distributions for several model surfaces, or surface height functions.

The aforementioned vdW force model is derived from the limit of quasi-static behavior of the cantilever, in which the cantilever is assumed to always be in mechanical equilibrium up until the critical point and at which the tip then immediately "jumps" into contact with the surface. In practice, however, the cantilever approaches the surface at a finite approach speed, such that mechanical equilibrium cannot truly be maintained (due to inertial effects). Therefore, a model describing the dynamic behavior of the cantilever tip is presented. An effective Hamaker constant is obtained for a particular surface and cantilever approach speed by minimizing the relative entropy, which is a quantitative metric used to determine the "closeness" of two probability distribution functions, between the d_c-distributions generated from the dynamic model and quasi-static limit. The effective A approaches the "true" A at sufficiently slow cantilever approach speeds, and this trend is validated computationally for various model surfaces. Therefore, the behavior of the cantilever is well-described by the quasi-static model and so d_c-values obtained experimentally can be properly compared with those predicted using the previously-developed quasi-static model.

Finally, a robust method to extract an accurate value of A from an experimentally obtained d_c-distribution for a particular substrate is developed. By inputting a range of A-values, the Hamaker constant of a given substrate, with a given surface roughness, is estimated by minimizing the relative entropy between the experimental (or true) and model-predicted (the surface with its given roughness) d_c-distributions. The self-Hamaker constant, A_{11}, of three experimental substrates – amorphous silica, stainless steel, and sapphire – is determined over a range of experimental surfaces with varying topographies. This provides a true test of the method since surface roughness is taken directly into account, and so the self-Hamaker constant, with a small degree of inevitable experimental error, should be constant across each surface for a particular substrate. The A_{11} values were found to be in excellent agreement between surfaces comprised of the same substrate, and the average A_{11} value across all plates for a particular substrate agreed very well with those found in the literature derived from the rigorous theoretical Lifshitz theory.

1. INTRODUCTION

1.1 Particle Adhesion and Intermolecular Forces

Understanding and potentially controlling particle adhesion is important to a variety of industries and applications. For example, particle adhesion often dictates the final properties of pharmaceutical products such as tablets, and uncontrolled particle adhesion can lead to picking and sticking of dye/tablet surfaces leading to a loss of product.[1–5] In addition, controlling the degree of particle adhesion to surfaces is critical in the semiconductor industry where surface contamination poses a significant threat to semiconductor production.[6–8] Finally, particle adhesion plays a role in explosive detection systems, colloidal stability, and the development of biomimetic polymers.[9–15]

Particle adhesion also plays a significant role in the processing of bulk solid materials.[16] For example, ratholing and bridging inside a hopper can occur due to uncontrolled particle adhesion leading to poor flow conditions.[17] Furthermore, the design of pneumatic and mechanical conveyors to transport solid materials is influenced by the degree of particle adhesion of the material.[18] Finally, understanding the adhesion of particles to other particles and to surfaces is crucial for process operations involving size reduction, classification, particle formation and isolation, and product formulation which include granulation, milling, spray drying, roller compaction, and tableting.[5,19–24]

Broadly speaking, particle adhesion occurs due to the presence of intermolecular forces between polar or nonpolar molecules and include capillary and electrostatic forces, permanent/induced dipole forces, and van der Waals (vdW) forces.[25–29] For neutrally charged materials, particle adhesion arises primarily due to the dominant attractive vdW force.[30] Capillary forces dominate in water-rich environments where liquid bridging occurs at the contact site

between two surfaces, and electrostatic forces occur as a result of charged particle surfaces.[31,32] Dipole interactions exist between polar molecules as a result of unequal sharing of electrons within the electron cloud between molecules.[33] vdW forces are of particular interest because they are always present in a system[9,34] compared to the other types of intermolecular forces which are present under certain conditions. The strength of the vdW force between a pair of interacting materials (or like materials) is quantified by the Hamaker constant, A.[25,35] As such, this work is concerned with the development of a reliable method to quantify the Hamaker constant (and, in turn, the strength of the vdW force) across a range of solid materials.

1.2 The Hamaker Constant: Quantifying the Strength of the vdW Force

The vdW force between interacting atoms and molecules consists of a combination of three forces: Debye, Keesom, and London dispersion.[25] Debye forces are present between permanent and induced dipoles while Keesom forces exist between two permanent dipoles. London dispersion forces result from instantaneous dipoles that form due to fluctuations between electrons within adjacent electron clouds between atoms or molecules.[25] London quantified this dispersion effect between two spherically symmetrical atoms or molecules and found the interaction energy to be of leading order[36]

$$U = -\frac{C}{R^6} \tag{1.1}$$

where R is the separation distance between the interacting bodies and the constant, C, is related to the polarizability of the electron clouds of each molecule or atom. Hamaker then expanded upon the work of London by calculating the vdW interaction between two interacting bodies through a pairwise additive approach (*i.e.* calculating the interaction force between each pair of atoms

between bodies and summing over the total volume).[35,37] The total energy (or potential) of interaction between two particles is therefore

$$U = -\int_{V_1} dv_1 \int_{V_2} dv_2 \frac{\rho_1 \rho_2 \lambda_{12}}{R^6} \tag{1.2}$$

where dv_1, dv_2, V_1, V_2 are the volume elements and volumes of each particle, ρ_1 and ρ_2 are the density of each particle, λ_{12} is the London vdW constant between the particles (particle "1" interacting with particle "2"), and R is the separation distance between particles. The Hamaker constant describing the interaction of two bodies (or particles), 1 and 2, is therefore defined to be[35]

$$A_{12} = \rho_1 \rho_2 \lambda_{12} \tag{1.3}$$

In general, the Hamaker constant describes the interaction between materials i and j through a medium k, or A_{ikj}. In the limit of a vacuum, there is no effect of the medium on the vdW force. In the case where the medium is air and the separation distance between the bodies is very small, *e.g.,* less than 10 nm, the effect of the air is negligible. In either of these cases, A_{ikj} is instead denoted as A_{ij}, or henceforth simply as A. If the two interacting materials are the same, the self-Hamaker constant is written as A_{ii} or A_{jj} and, to a good approximation[38]

$$A = A_{ij} \approx \sqrt{A_{ii} A_{jj}} \tag{1.4}$$

Typical values of the Hamaker constant range from 4-500 zJ in a vacuum. For example, the self-Hamaker constant of diamond is approximately 300 zJ, 150 zJ for sapphire, 65 zJ for silica, 40 zJ for Teflon, and 200-500 zJ for metals.[25]

From eq 1.2, the vdW force between two bodies can be determined for a given set of material properties and geometries. For example, the vdW force between two infinitely flat plates separated by distance z is given as[25]

$$F_{vdW} = \frac{A}{6\pi z^3} \tag{1.5}$$

where the force is the negative derivative of the potential, U, with respect to the separation distance, z. Other common geometries for which vdW force expressions have been derived include two flat plates, two spheres, and two parallel cylinders or rods.[25] If the value of the Hamaker constant is known for a material or system, the vdW force can then be computed using the appropriate analog of eq 1.5 to describe the geometry of the system.

Several methods have been developed to study the particle adhesion of a system and quantify the Hamaker constant of a material. Lifshitz determined the Hamaker constant of materials using a continuum mechanics approach by rigorously deriving the vdW interaction potential from electro-optical properties of the interacting materials.[39–45] While this method provides an accurate quantification of the Hamaker constant, proper implementation requires dielectric response information for a material to be obtained over the entire electromagnetic spectrum, which is difficult to obtain experimentally. Therefore, this type of data has been acquired for only a small fraction of materials. As a result, more practical experimental methods have been developed to determine the Hamaker constant including the surface force apparatus, centrifuge technique, contact angle goniometer, and atomic force microscope (AFM).[46,47] The surface force apparatus is a direct force measurement technique that can be used to measure a range of surface forces but is limited to materials with perfectly smooth surfaces.[48] The centrifuge technique correlates the force of adhesion to the inertial force required to remove particles of varying sizes from a plate as a function of rotational speed. This method is applicable, however, to determining the force of adhesion of bulk powders only, as opposed to single particles.[49] The Hamaker constant may also be estimated from the surface energy of a material using a contact angle goniometer, but requires information regarding the intermolecular spacing in the bulk

material.[38,50] The AFM is of particular interest because it can be used to accurately measure electrostatic attraction, liquid bridging, and vdW interactions across a broad range of solid materials at the nanometer length scale.[51–58] The development of a new AFM-based method for determining the Hamaker constant of solid materials is the focus of this thesis.

1.3 The Principle of Atomic Force Microscopy

An AFM, through the use of a flexible cantilever, is capable of producing high resolution topographical images of surfaces, as well as determining the attractive force between the cantilever tip and a surface. Figure 1.1 is a schematic of an AFM showing key components. A sample is mounted to a piezoelectric column which expands or contracts in response to an applied voltage. The sample is therefore able to approach or retract from a cantilever which is fixed in place. As the sample approaches the cantilever tip, the cantilever begins to deflect due to the attractive vdW force between the sample and tip. This change in deflection is measured by a photodetector from a laser which shines on the tip and is reflected by a mirror to the photodetector. By calibrating the deflection sensitivity (which is given in units of nm/V) against a nondeformable material such as sapphire, the total deflection of the cantilever can be determined. During an AFM force experiment, the deflection of the cantilever is measured as the sample is brought towards and then away from the cantilever at a specific speed.

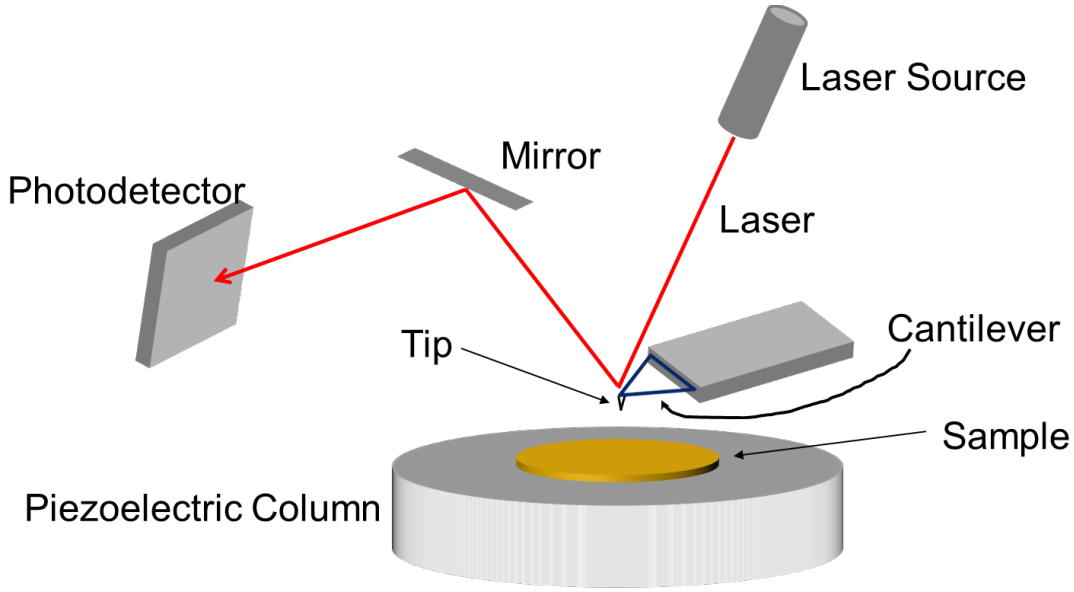

Figure 1.1 Schematic of an atomic force microscope. The deflection of a flexible cantilever is measured as the relative separation distance between a sample mounted to a piezoelectric column and cantilever tip varies.

By measuring the resulting deflection as a function of the relative separation of the tip and surface as the cantilever approaches the surface, a deflection curve is generated (Figure 1.2) from which an estimate of the Hamaker constant can be determined. At point A, the cantilever tip and surface are sufficiently far from each other such that the vdW force is weak, and so no deflection of the cantilever is observed. As the surface approaches the cantilever, the attractive tip-surface force causes the cantilever to deflection towards the surface. Beyond a critical tip-surface separation distance, or limit of stability (point B), the magnitude of the vdW force exceeds the restoring force of the cantilever. As a result, the tip spontaneously jumps into contact with the surface (point C). Finally, the surface retracts from the cantilever, eventually reaching a point where the restoring force exceeds the vdW force (point D), and the cantilever "pulls off" from the surface. Utilizing the "pull-off" portion of the force curve to infer the force of adhesion is a relatively simple and popular method to describe the adhesion of a system across a variety of applications.[59–66]

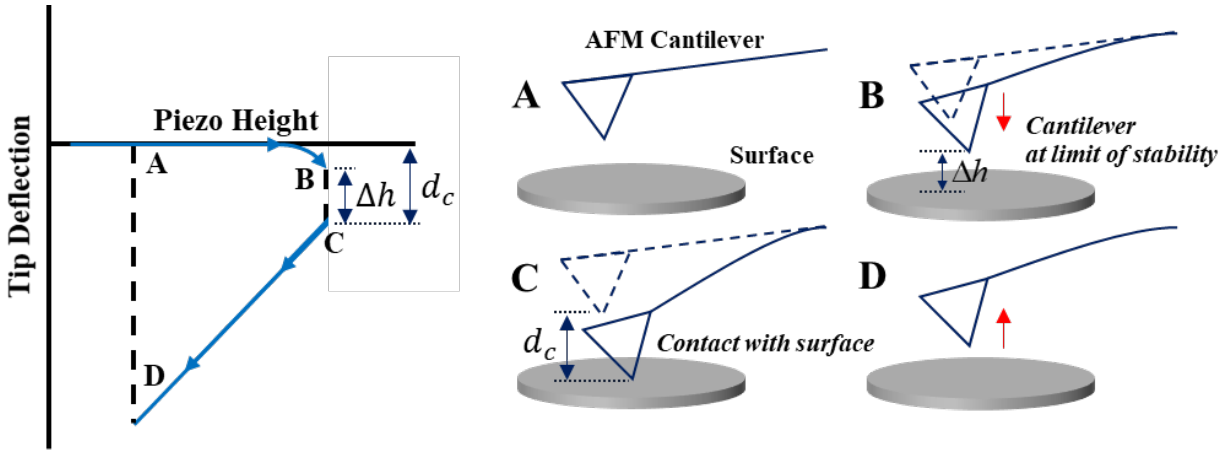

Figure 1.2 AFM deflection curve generated from a force experiment. Initially (point A), the AFM cantilever and surface are sufficiently far from each other such that no deflection of the cantilever is observed. As the cantilever is brought close to the surface, the cantilever begins to deflect, eventually reaching a critical point, or limit of stability (point B). At the next instant beyond the critical point, the cantilever jumps into contact with the surface (point C). Finally, the cantilever jumps out of contact (point D) when the restoring force of the cantilever overcomes the attractive tip-surface force.

Several AFM-based methods have been proposed to estimate the Hamaker constant of a solid material, each using different parts of the AFM deflection curve. For example, the Hamaker constant can be related to the experimentally measured maximum attractive force required to separate the cantilever tip from the surface after the tip has been placed in direct contact with the surface (commonly referred to as the "pull-off" portion of the deflection curve). However, this "pull-off" method is sensitive to materials with rough surfaces[67–71] and difficult to implement on deformable surfaces.[72–74]

The behavior of the cantilever in the approach-to-contact portion of the deflection curve has been analyzed,[75–80] leading to various approaches towards quantifying the Hamaker constant. In this part of the deflection curve, the behavior of the tip is assumed to be quasi-static; the tip is taken to be in mechanical equilibrium at each instant during its approach. In this model or description of the deflection of the tip, the attractive tip surface vdW force is assumed to always

be balanced by the restoring (Hookean spring) force of the cantilever. Even for this model, mechanical equilibrium cannot be satisfied for all tip-surface separations. Beyond a critical tip-surface separation distance, or limit of stability, the magnitude of the vdW force always exceeds the restoring force of the cantilever. As a result, the tip immediately jumps into contact with the surface in the quasi-static limit, and the magnitude of this jump (the difference in cantilever deflection between points B and C or Δh in Figure 1.2), can be related to the Hamaker constant.[77] However, it was later found[80] that since the surface approaches the cantilever tip with a non-zero approach speed during an AFM experiment, the quasi-static model fails to capture the inertial behavior of the cantilever tip. In addition, because an experimental deflection curve is composed of a set of discrete data, the precise location of the limit of stability is dependent on the sampling resolution of the experiment. Therefore, the limit of stability is extremely difficult to obtain consistently, if at all, from an AFM deflection curve.

1.4 The Approach-to-Contact AFM Method

Fronczak *et al.*[80] revisited the quasi-static assumption and developed a new approach-to-contact method that relates A to a new parameter, the deflection of the tip at first contact with the surface, d_c. The deflection at first contact can be found more reliably from AFM experiments, though it is weakly dependent on the approach speed. When the approach speed is sufficiently slow that inertial effects become unimportant, d_c reaches a limiting value that can be obtained using the quasi-static model. Thus, upon treating the cantilever tip as a sphere with an effective radius of R_{eff}, one finds for a sufficiently low approach speed that for a sphere and infinitely flat plate[80]

$$A = \frac{8}{9}\frac{k_c(d_c)^3}{R_{eff}} \tag{1.6}$$

where A is the Hamaker constant describing the interaction between the surface and the tip and k_c is the spring constant of the cantilever. (Since eq 1.6 is based on the assumption of pair-wise additive interactions between elements in the sphere and in the smooth substrate, A is, by construction, only relevant to other force models that likewise invoke the pair-wise additive assumption.) Substituting eq 1.4 into eq 1.6 gives the following

$$A_{ii} = \frac{8}{9}\frac{k_c^2 (d_c)^6}{A_{jj} R_{eff}^2} \tag{1.7}$$

and estimates of A_{ii} were obtained for several materials that were in good agreement with the predictions of the Lifshitz approximation.[79,80] Fronczak *et al.*[80] also discussed how to determine the effective radius of the cantilever tip through the use of a "calibration" surface with a known (or reliable) Hamaker constant, thereby avoiding the previous need to visually fit the shape of the cantilever tip prior to running an AFM experiment.

The proper implementation of eq 1.7 strictly requires that the chosen surfaces be ideally smooth, *i.e.*, no surface roughness. For such surfaces, only a single value of d_c should in principle be obtained from AFM measurements, regardless of the location along the surface for which the cantilever tip and surface are brought together. But some degree of surface roughness is experimentally unavoidable. Even for nominally smooth amorphous silica and a silicon nitride AFM tip, Fronczak *et al.*[80] reported a distribution of d_c-values, shown in Figure 1.3, with an average value of 4.98 nm and range between ~4-6 nm.

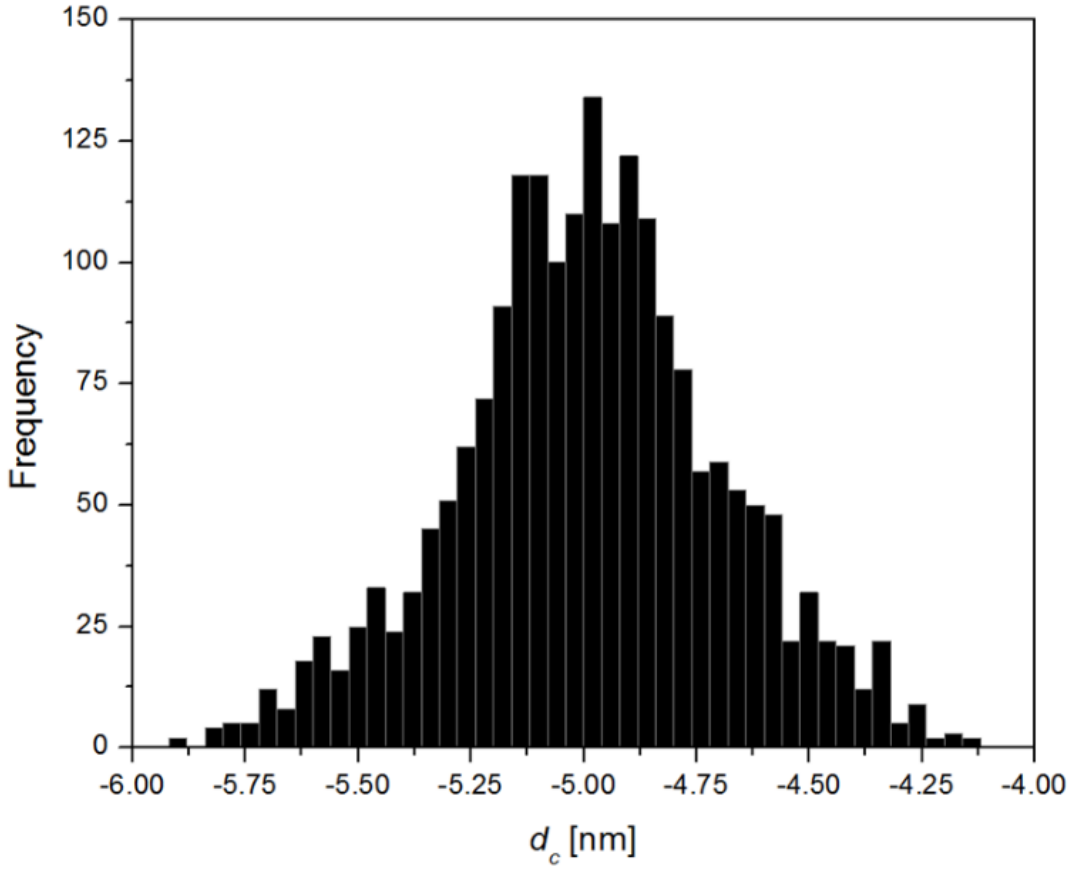

Figure 1.3 Experimentally-obtained distribution of deflection at contact for amorphous silica shown in Figure 6 of Ref 80.

As noted before, this average value, when substituted into eq 1.7 (along with the corresponding cantilever properties), yields a self-Hamaker constant of amorphous silica that is in excellent agreement with the Lifshitz approximation. Yet, the measured range of d_c-values spanned about 2 nm where some contacts yielded a magnitude of d_c as large as ~5.8 nm or as small as ~4.2 nm. Furthermore, since eq 1.7 corresponds to an A_{ii} that is proportional to the sixth power of d_c, even the small relative errors in the reported d_c-values are greatly propagated in the calculation of the self-Hamaker constants.

Inherent surface roughness is the primary reason for the emergence of the broad distribution of deflections at first contact, even for a "relatively" smooth surface like amorphous

silica. Because of surface roughness, different values of d_c should be obtained as the tip accesses spatially separate surface positions (*i.e.*, probes the "global" roughness), and as the tip attempts to access the same surface position but cannot do so exactly (*i.e.*, probes the "local" roughness) due to the inevitable horizontal drift of the cantilever.[81–84] The magnitude of the vdW force at each location probed by the cantilever tip directly influences d_c and therefore, for a rough surface, varies over each measurement.

For completeness, other effects may give rise to a distribution of d_c-values, although their associated magnitudes appear to be much smaller than the range of d_c-values observed experimentally for amorphous silica. For example, the root mean square deflection of the thermal noise of an AFM cantilever with a spring constant of 0.1 N/m is on the order of 0.1nm at 22°C.[85] The possible deformation of the amorphous silica surface likewise seems to be negligible as the deformation of the surface (assumed to be an infinite flat plate) due to a silicon nitride sphere is on the order of an angstrom.[86,87]

Given that the resulting d_c-distribution should be directly influenced by the inherent surface roughness, key improvements to the approach-to-contact AFM method developed by Fronczak *et al.*[79,80] will be obtained by explicitly accounting for the topography of the given surface. If the effects of surface roughness can be included in an appropriate extension of eq 1.7, the Hamaker constant will therefore be related to a d_c-distribution, instead of just a single value of d_c. Hence, this updated approach-to-contact method should, in principle, yield the same value of *A* for all surfaces comprised of the same material, though not necessarily with the same degrees of roughness (nor with the same resulting d_c-distributions). As an additional benefit, any pre-treatment or smoothing of the surface prior to the start of an AFM measurement may no longer be required, thereby extending the range of solid surfaces that could be analyzed with the approach-

to-contact method. Moreover, the incorporation of surface roughness into the method, via the direct connection of A to a given surface's characteristic d_c-distribution, should lead to more accurate estimates of the Hamaker constant with a significant reduction in their uncertainties.

1.5 Project Motivation and Summary

The overall goal of this work was to develop an updated approach-to-contact AFM method to directly account for material surface roughness and to obtain accurate estimates of the self-Hamaker constant for a range of solid materials from a distribution of deflections at contact. First, a novel vdW force model was derived describing the interaction of an AFM cantilever tip interacting with an arbitrary surface. Since the topography of the surface is incorporated in the method, such that the resulting vdW force varies locally along the surface, a distribution of deflections at contact was obtained for a series of model surfaces. The analysis of the resulting d_c-distribution revealed that local surface curvature has a large impact on the measured cantilever deflections.

A dynamic model of the AFM cantilever approaching a surface of arbitrary roughness was then developed including an analysis of the approach speed, v_c, on the shape and magnitude of the resulting model-predicted d_c-distribution. An effective Hamaker constant was obtained for a particular surface and v_c, by minimizing the relative entropy between the d_c-distributions generated from the dynamic model and quasi-static limit (*i.e.* when $v_c \rightarrow 0$). (The relative entropy is a quantitative metric used to determine the "closeness" of two probability distribution functions.) The effective A approached the "true" A at sufficiently slow cantilever approach speeds, and this trend was validated computationally for various model surfaces. Therefore, the behavior of the cantilever was well-described by the quasi-static model and so d_c-values obtained experimentally

could be properly compared with those predicted using the previously-developed quasi-static model.

A robust method to extract an accurate value of A from an experimentally obtained d_c-distribution for a particular substrate was then developed. By inputting a range of A-values, the Hamaker constant of a given substrate, with a given surface roughness, was estimated by minimizing the relative entropy between the experimental (or true) and model-predicted (the surface with its given roughness) d_c-distributions. A self-consistency check of the method was first performed computationally to ensure that the outputted Hamaker constant was similar to that of the chosen input value for various surface geometries and for various slow-enough AFM cantilever approach speeds. Due to the difficulty in performing AFM imaging and force experiments on the exact same region on the surface, another method was developed utilizing the spatial Fourier transform of the surface in order to generate representative images of the surface with the same overall surface characteristics.

Finally, the updated approach-to-contact method was validated by determining the self-Hamaker constant of several solid materials (*e.g.* amorphous silica, stainless steel, and sapphire) experimentally from an AFM surface scan of the given substrate and using a series of cantilevers with defined radius. The topographies of the materials were systematically polished to varying degrees of roughness to ensure a variety of resulting experimental d_c-distributions with different magnitudes and shapes. The A_{11} values were found to be in excellent agreement between plates of the same material and the average A_{11} value across all plates for a particular substrate agreed well with those found in the literature derived from Lifshitz theory.

The subsequent chapters that comprise this work are as follows. Chapter 2 presents a general description of the vdW force between the cantilever tip and surface that fully captures the

effects of surface topography; the cantilever is modeled as an effective sphere and the sphere is considered to interact with any arbitrary surface (as opposed to a semi-infinite flat plate). Thus, the analogue of eq 1.7 is derived, thereby providing the needed connection between the Hamaker constant and the resulting distribution of d_c-values. The deflection at contact is obtained along any point on the arbitrary surface based on calculation of the critical point (or limit of stability) of the sphere above the surface and the contact point that the sphere makes with the surface. The quasi-static model is utilized to determine the critical point conditions and a method is discussed to determine the contact point between the sphere and surface.

Chapter 3 investigates the impact of surface topography on "contact locus" curves (for surfaces that vary solely in the x-direction) and "contact mesh" plots (for surfaces that vary in both the x- and y-directions) as the sphere samples each portion of the surface. Furthermore, with the d_c-distribution yielding an apparent signature of the underlying surface roughness, for various model surfaces with a given value of A, the impact of the surface topography on the obtained d_c-distribution is considered.

Chapter 4 details a model describing the dynamic behavior of the cantilever tip as it approaches and interacts with an arbitrary surface. From a quantitative comparison of the d_c-distributions generated with both the quasi-static and dynamic models, a specific threshold cantilever approach speed is determined, in which the difference between these two distributions becomes unimportant. This difference is quantified by the relative entropy between the quasi-static and dynamic distributions. By selecting approach speeds below this threshold value, subsequent experimentally-obtained d_c-distributions can therefore be confidently compared to the corresponding quasi-static d_c-distribution. Hence, the proposed method for estimating A requires only the determination of the quasi-static d_c-distribution for a particular surface, thereby avoiding

the additional computational expense of generating the dynamic d_c-distributions. A method is then presented whereby the resulting d_c-distribution of a given substrate can be directly mapped onto a single value of A with, in general, high certainty. A computational test of this method is discussed, showing that the determined values of A for various model surfaces match the inputted values of A within relatively small uncertainties. Moreover, it is demonstrated that nearly identical values of A are still extracted from the method when the substrates are comprised of the same material (*i.e.*, the same inputted A) but nonetheless have very different underlying surface roughness features.

Chapter 5 discusses a method for generating representative or reconstructed AFM surface height maps by expanding on a previously developed discrete Fourier transform (DFT) method.[88,89] The motivation for such a method arises due to the fact that deflection and imaging experiments cannot necessarily be conducted along the same exact portion of a surface. This DFT method ensures that the root-mean-squared (RMS) roughness of each representative surface height map remains constant and matches that of the original surface scan, while also generating surfaces with nearly identical distributions of the various peak heights. Chapter 5 also provides a comprehensive discussion of the mathematics of DFT applied to one-dimensional and two-dimensional surface height functions.

Chapter 6 considers a full experimental validation of the method, where the self-Hamaker constant of various materials is determined and compared (favorably) to literature-established values. By systemically varying the roughness across a range of sample surfaces for a particular material and implementing the approach-to-contact method, a single self-Hamaker constant is extracted for each sample and averaged to obtain a final Hamaker constant value for a particular material. While the shape of the individual d_c-distributions varies slightly between each of the

sample surfaces for a material, the difference between the individual Hamaker constants corresponding to each sample surface is minimal.

Finally, Chapter 7 discusses, in addition to concluding remarks, future work that considers extending the modified approach-to-contact model to (1) fluid environments, (2) deformable materials, and (3) roughness on the AFM cantilever (*i.e.*, roughness on the sphere). The introduction of roughness on the sphere and extending the analysis to fluid environments as well as to deformable materials would provide a robust extension to the AFM based method developed herein to determine the self-Hamaker constant of a whole range of materials for a wide variety of applications.

2. DETERMINATION OF CANTILEVER DEFLECTIONS FOR A SURFACE WITH ARBITRARY ROUGHNESS: QUASI-STATIC MODEL

2.1 Introduction

The development of the modified approach-to-contact method begins with the derivation of a new expression describing the vdW force between an AFM cantilever tip, treated as an effective sphere, and a surface of arbitrary roughness. The underlying material surface geometry and surface roughness can be modeled directly using a surface height function, h, and the vdW force can be computed using the new expression over the full domain of the surface. Corresponding critical point conditions are then derived under the quasi-static assumption in order to determine the deflection of the cantilever at contact with the surface, d_c. In addition, a method is discussed to determine the point of first contact between the sphere and any point on an arbitrary surface.

2.2 The vdW Force Between a Spherical AFM Tip and an Arbitrary Surface

Previous descriptions of the behavior of an AFM tip in the approach-to-contact regime are based on the quasi-static model, in which the cantilever tip is assumed to always be in mechanical equilibrium at sufficiently large separation distances from the surface.[75–77] With only the spring or restoring force, F_{spr}, and the attractive tip-surface force, F_{surf}, acting on the cantilever tip (both in the vertical direction only as no twisting of the cantilever is assumed in the other directions), the quasi-static assumption requires that

$$F_{surf} + F_{spr} = 0 \tag{2.1}$$

The tip-surface force is a function of the separation distance between the cantilever tip and the surface while the spring force depends on the cantilever deflection, d. The cantilever is typically

assumed to deform elastically, and so the restoring force is described using Hooke's law, $F_{spr} = -k_c d$, where a negative deflection results in an upward (away from the surface) spring force.

The functional form of F_{surf} depends on the specific geometries of the two interacting bodies. Fronczak *et al*.[79] found that the vdW force interaction between a flat plate and a truncated pyramid with a spherical cap (a typically chosen description of the shape of the cantilever tip) is well modeled by a sphere with an appropriately chosen effective radius interacting with the same flat plate.

All surfaces exhibit some degree of roughness, however, which should be accounted for when attempting to model the force interaction between the tip and surface (regardless of how the tip geometry is being described). Thus, while always treating the cantilever tip as a sphere of radius R, a general vdW force expression describing the interaction between a sphere and a surface of arbitrary roughness is derived below.

The system of interest is shown in Figure 2.1, in which a sphere, or the AFM cantilever tip, interacts with an arbitrary surface described by a height function $h(x, y)$. The surface is taken to be semi-infinite, extending to infinity in both the positive and negative x- and y-directions, and extending to negative infinity in the z-direction. The topography of the surface is fully captured by the given surface height function. To simulate the cantilever, the top of the sphere is attached to a horizontal platform with a Hookean spring.

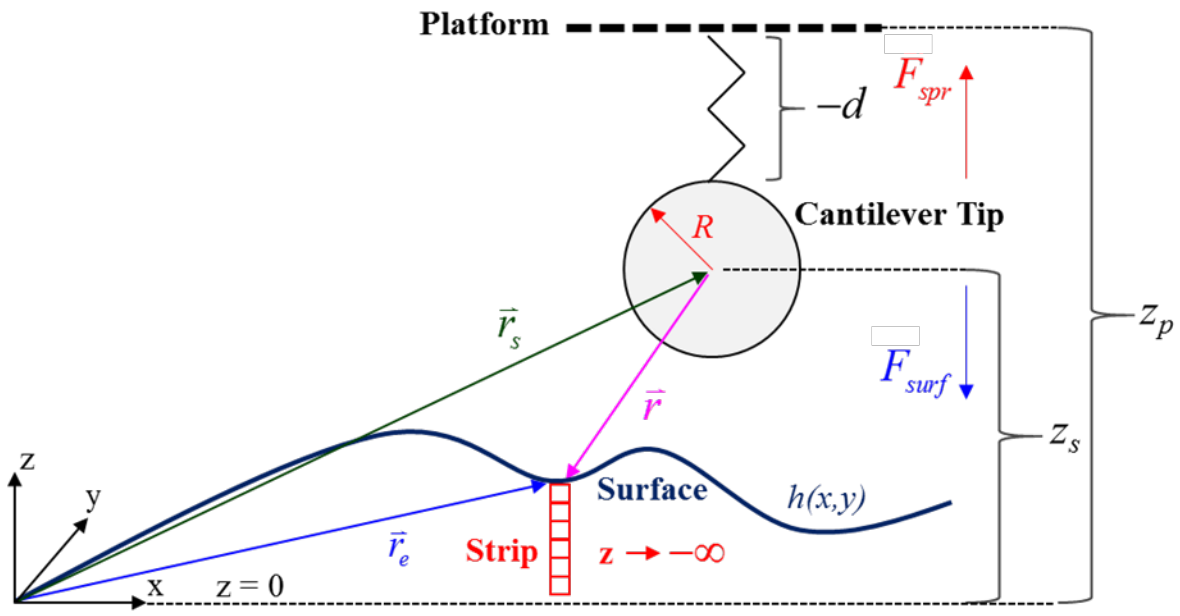

Figure 2.1 Schematic of an AFM cantilever tip modeled as a sphere attached to a horizontal platform by a Hookean spring, in which the sphere also interacts with an arbitrary surface described by the surface height function $h(x, y)$. z_s and z_p are the vertical locations of the sphere and platform, respectively, from $z = 0$, R is the radius of the sphere, $\vec{r}_s$ is a vector from the origin to the center of the sphere, $\vec{r}_e$ is a vector describing the location of a differential volume element within the substrate from the origin, and $\vec{r}$ is a vector from the center of the sphere to the differential volume element. d is the deflection of the spring.

The platform is located at a vertical distance z_p away from an arbitrarily chosen $z = 0$ plane, and the center of the sphere is located at the vector $\vec{r}_s$, the z-component of which, or z_s, denotes the vertical position of the sphere center. The x- and y-components of this vector are denoted as x_s and y_s, respectively. The deflection, d, of the spring is determined by $z_s + R - d = z_P$, such that $d < 0$ indicates that the sphere resides below the platform (*i.e.,* the cantilever deflects downward toward the surface). A differential volume element residing within the substrate is located at $\vec{r}_e$. The vector $\vec{r}$ pointing from the center of the sphere to this differential element is given by $\vec{r} = \vec{r}_e - \vec{r}_s$. The z-components of the spring and surface forces are positive when in the upward direction, and negative in the downward direction.

The derivation of the vdW force expression begins by determining the vdW interaction potential energy, $u(r)$, between a sphere of radius R and a differential volume element located a distance z from the surface of the sphere, in which $r = z + R$ is the distance between the element and the center of the sphere as shown in Figure 2.2. (Due to the symmetry inherent to the sphere, the relative three-dimensional orientation of the volume element with respect to the sphere is irrelevant, and the final result will depend only on $r = z + R$.)

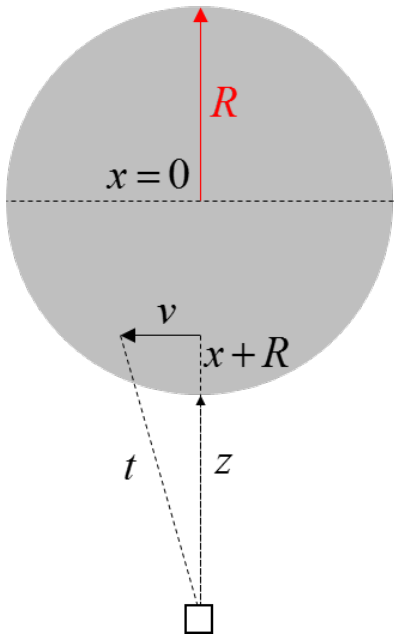

Figure 2.2 A sphere of radius R (shaded circle) interacting with a differential volume element (open square) separated by a distance $z > 0$ from the surface of the sphere, in which $z + R$ is the distance between the element and the center of the sphere. The distance from this element to another differential volume element residing within the sphere is denoted by t. The vertical distance from the center of the sphere is denoted by x, for which $-R \leq x \leq R$. Hence, the vertical distance between the two elements is $z + x + R > 0$. The radial distance between the midpoint of the sphere and an element within the sphere is denoted by v, in which $0 \leq v \leq (R^2 - x^2)^{1/2}$.

Now, any two elements with differential volumes dV_1 and dV_2 that are separated by a distance t will give rise to a vdW potential energy of interaction equal to $-(\rho_1 \rho_2 C dV_1 dV_2)/t^6$, where we have assumed the usual (non-retarded) inverse sixth-power law for the vdW interaction

between two bodies[90,91], ρ_1 and ρ_2 are the number densities of the elements, respectively, and c is the vdW interaction parameter between materials 1 and 2. If dV_2 represents a volume element within the sphere, and assuming pairwise additivity[90,91], the vdW interaction potential energy (per volume element dV_1) and the entire sphere, denoted by $u(z)$, is given by

$$u(z) = -2\pi\rho_1\rho_2 c \int_{-R}^{R}\int_{0}^{(R^2-x^2)^{1/2}} \frac{1}{t^6} v dv dx \tag{2.2}$$

where dV_2 has been replaced by the circular ring $2\pi v dv dx$ at the given t and the variables v and x are defined in Figure 2.1. Noting that $t^2 = v^2 + (z + x + R)^2$, eq 2.2 is rewritten as

$$u(z) = -\frac{2A}{\pi}\int_{-R}^{R}\int_{0}^{(R^2-x^2)^{1/2}} \frac{1}{[v^2 + (z + x + R)^2]^3} v dv dx \tag{2.3}$$

in which $A \equiv \pi^2\rho_1\rho_2 c$. Performing the two integrations, and again noting that $r = z + R$, yields

$$u(r) = \frac{A}{2\pi}\left[\frac{2R}{(r-R)^2(r+R)^2} + \frac{1}{3(r+R)^3} - \frac{1}{3(r-R)^3}\right] \tag{2.4}$$

In general, the force between two bodies separated by a center-to-center distance r is given by $\vec{f}(r) = -\nabla u(r)$, where ∇ is the gradient operator. Since the torsional movement of the cantilever is typically assumed to be negligible compared to its vertical deflection as the tip approaches the surface, only the z-component of the vdW force on the sphere due to the dV_1 substrate element is determined. The force on the sphere in the z-direction per volume element dV_1 is therefore evaluated via (where, in this case, ∇ represents the partial derivatives with respect to the coordinates of the center of the sphere)

$$f_z = -\frac{\partial}{\partial z_s}u(r) = -\frac{\partial u}{\partial r}\cdot\frac{\partial r}{\partial z_s} \tag{2.5}$$

where z_s is the vertical height of the center of the sphere. Referring to Figure 2.1, in which (x_e, y_e, z_e) is the location of the substrate element and (x_s, y_s, z_s) is the location of the sphere center, the distance r from the center of the sphere to the element is given by

$$r = [(x_e - x_s)^2 + (y_e - y_s)^2 + (z_e - z_s)^2]^{1/2} \tag{2.6}$$

With eqs 2.4 and 2.6, eq 2.5 indicates that

$$f_z = \frac{8AR^3}{\pi} \frac{(z_e - z_s)}{(r^2 - R^2)^4} \tag{2.7}$$

which is always negative (i.e., an attractive force) as long as the vertical height of the element is always below that of the sphere center (i.e., $z_e < z_s$). This force diverges when the element touches the sphere at any point along its surface, for which $r = R$. To obtain the total force acting on the sphere in the z-direction due to the entire surface, eq 2.7 is first integrated over the height of a vertical and semi-infinite differential strip (located at x_e, y_e) that extends from the top of the surface, located at $h(x_e, y_e)$, down to $-\infty$. Since x_e and y_e are constant for this strip, the result is

$$F_{strip} = \int_{-\infty}^{h(x_e,y_e)} f_z dz_e = -\frac{4}{3}\frac{AR^3}{\pi} \frac{1}{[(x_e - x_s)^2 + (y_e - y_s)^2 + (h(x_e, y_e) - z_s)^2 - R^2]^3} \tag{2.8}$$

Then, eq 2.8 is integrated in the x- and y-directions, or over all the differential vertical strips comprising the surface. The final result, after introducing the following nondimensional variables $x_e^* = x_e/R, y_e^* = y_e/R, x_s^* = x_s/R, y_s^* = y_s/R, h^* = h/R, z_s^* = z_s/R$, is

$$F_{surf} = -\frac{4}{3}\frac{A}{\pi R} \int_{-\infty}^{\infty} \int_{-\infty}^{\infty} \frac{dx_e^* dy_e^*}{[(x_e^* - x_s^*)^2 + (y_e^* - y_s^*)^2 + (h^*(x_e^*, y_e^*) - z_s^*)^2 - 1]^3} \tag{2.9}$$

Eq 2.9 allows for the underlying material surface geometry, or surface roughness, to be modeled directly using an appropriate (and essentially arbitrary) surface height function, h. If h is known, eq 2.9 provides a rigorous expression for the tip-surface vdW force interaction (for the

assumptions of pairwise additivity and the inverse sixth power dependence on separation distances for the potential energies of interaction). The function h can, in principle, be obtained from an AFM operating in tapping mode (or any other AFM mode which tracks the topography of the surface), thereby producing a high-resolution topographical image of some portion of the surface.

If the surface height function only depends on a single variable, say x_e^*, or $h^*(x_e^*)$, then the integration over y_e^* can be done analytically. To do so, first note that[92]

$$\int_{-\infty}^{\infty} \frac{dy}{(ay^2+c)^n} = \frac{(2n-3)!!}{(2n-2)!!}\frac{\pi a^{n-1}}{(ac)^{n-1/2}} \tag{2.10}$$

For $n = 3$, the double factorials are evaluated as follows

$$\frac{(2n-3)!!}{(2n-2)!!} = \frac{3!!}{4!!} = \frac{3\times 1}{4\times 2} = \frac{3}{8} \tag{2.11}$$

Comparing eq 2.10 to eq 2.9, and letting $c = (x_e^* - x_s^*)^2 + (h^*(x_e^*) - z_s^*)^2 - 1$ and $a = 1$, one finds that

$$F_{surf} = -\frac{1}{2}\frac{A}{R}\int_{-\infty}^{\infty} \frac{dx_e^*}{[(x_e^* - x_s^*)^2 + (h^*(x_e^*) - z_s^*)^2 - 1]^{5/2}} \tag{2.12}$$

Most of the previously developed approach-to-contact methods explicitly ignored the roughness inherent to any surface, and simply treated the surface as being an infinitely flat plate. [76–80,93] For a semi-infinite flat plate, the surface height function is a constant at all locations. Setting $h^* = 0$ for convenience, eq 2.12 can be further integrated analytically if the surface height function is a constant, which corresponds to the substrate being a semi-infinite flat plate. In this case, note that[92]

$$\int_{0}^{\infty} \frac{dx}{(x^2+c)^{n+3/2}} = \frac{(-2)^n}{(2n+1)!!}\frac{\partial^n}{\partial c^n}\left(\frac{1}{c}\right) \tag{2.13}$$

Letting $h^*(x_e^*) = 0$ for convenience, then with $c = (z_s^*)^2 - 1$ and $n = 1$, and given that the integrand of eq 2.12 is an even function of x_e^* (along with the bounds of the integral in eq 2.12 being from $-\infty$ to ∞), eq 2.13 indicates that eq 2.12 becomes

$$F_{surf,plate} = -\frac{2}{3}\frac{A}{R}\frac{1}{[(z_s^*)^2 - 1]^2} \tag{2.14}$$

matching a previously obtained expression for a flat plate (which was derived in a different manner).[2] Note that the sphere comes into direct contact with the flat plate when $z_s^* = 1$ (or $z_s = R$). Hence, z_s^* can be replaced with $1 + D^*$ (where $D^* = D/R$) in eq 2.14. For $D^* \ll 1$, *i.e.,* $D \ll R$, eq 2.14 reduces to eq 2.15 below. Eq 2.14 is valid for all values of z_s^*, or sphere-surface separation distances.

Previous attempts have been made to quantify the magnitude of the vdW force between two materials of varying geometries and incorporating material surface roughness directly into corresponding models. For example, the vdW attractive force between a sphere of radius R and a semi-infinite flat plate as originally derived by Hamaker[35] is given by

$$F_{vdW} = -\frac{AR}{6D^2} \tag{2.15}$$

where D is the separation distance between the bottom of the sphere and the surface. Eq 2.15 is only valid in the limit of $D << R$. To account for material surface roughness, some approaches have maintained the simple form of eq 2.15, introducing extensions of the flat plate result. For example, classical Rumpf theory models surface roughness as small hemispherical asperities, with radii much smaller than that of the interacting spherical particle, extending from an infinitely flat plate.[94] Rabinovich *et al.*[95] extended the work done by Rumpf by relating the height of the spherical asperities to the root-mean-square (RMS) roughness of the surface. Suresh *et al.*[65,96] developed a similar model by approximating surface roughness as hemispherical asperities. Fuller

and Tabor[97] modeled surface roughness as asperities with a distribution of heights following a Gaussian distribution. Finally, an adhesion simulator was developed[34,88,98] which considered the roughness of both the interacting particle and surface, but calculates the vdW force in an approximate manner. The particle and surface are both discretized into a series of cylinders, and only those pairs of cylinders that are vertically aligned are assumed to interact. The resulting vdW force is calculated approximately using the force equation for two flat surfaces.[25] An updated but still approximate scheme for including interactions between off-axial cylinders was developed[99], but has yet to be fully implemented in the simulator.

2.3 Critical Point Conditions for the Quasi-Static Assumption

Given that the tip-surface force diverges when the sphere comes into contact with the surface while the restoring force of the cantilever remains finite, a critical point, or limit of stability, is ultimately reached within the quasi-static assumption. For locations of the sphere closer to the surface than this critical point, $|F_{surf}| > |F_{spr}|$, and so the sphere can no longer be maintained in mechanical equilibrium.

Figure 2.3 is a graphical analysis illustrating the critical point phenomenon which is essentially a saddle-node bifurcation problem.[100] Eq 2.1 can be rewritten as $F_{surf} = -F_{spr}$ where F_{spr} is linear with respect to z_s, or $F_{spr} = -k_c d = -k_c(z_s - z_p + R)$. The blue and red curves, which are plotted separately, show the general shape of F_{surf} and F_{spr}, respectively. F_{surf} diverges to -∞ as $z_s \to R$ and goes to 0 as $z_s \to \infty$ (the curve is always negative). $-F_{spr}$ is always linear, with an intercept related to z_p. In Figure 2.3(a), as the cantilever approaches the surface, there are two equilibrium points, one stable point (green) and one unstable point (black). Small perturbations around the stable equilibrium point (*i.e.*, at large distances from the critical point)

result in the cantilever returning to its equilibrium position. If the cantilever were to reach the unstable critical point due to a large perturbation, the surface force would dominate, and the cantilever would jump into contact with the surface (this is very unlikely to physically occur). $-F_{spr}$ maintains the same slope since k_c is fixed. As the cantilever continues to approach the surface, the critical point, or saddle-node fixed point is ultimately reached as shown in Figure 2.3(b). This is where the two solutions merge or become a double root. Graphically, $-F_{spr}$ is tangent to F_{surf} at the saddle-node fixed point.

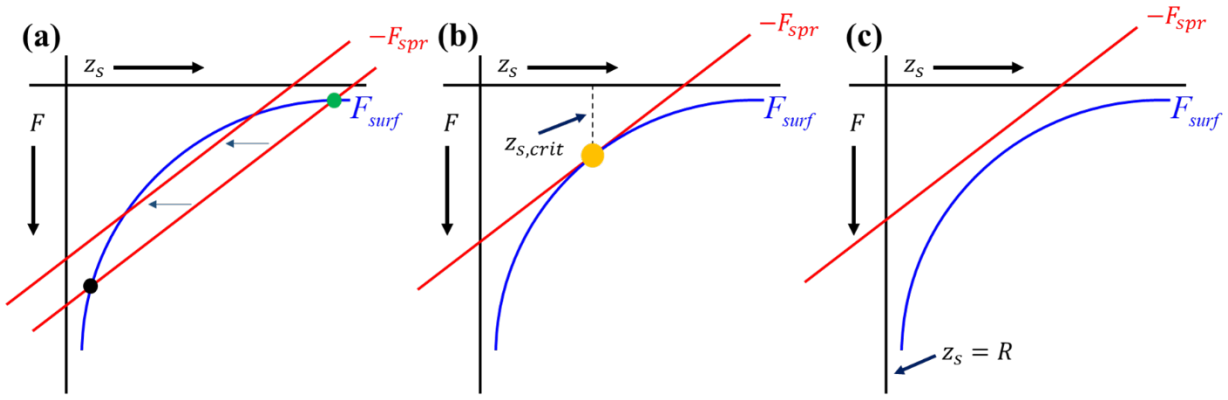

Figure 2.3 A graphical analysis illustrating the critical point phenomenon which occurs as the AFM cantilever approaches the surface of a material. This is a saddle-node bifurcation problem; (a) there are two equilibrium points, one stable point (green) at sufficiently far distances from the surface (*i.e.*, large z_s) and one unstable point (blue) close to the surface (*i.e.*, small z_s), (b) one equilibrium point, or a saddle-node fixed point at the critical point distance from the surface, and (c) no equilibrium points where the surface force dominates and the cantilever jumps into contact with the surface. The point at which the sphere touches the surface ($z_{s,contact}$) occurs at $z_s = R$.

Beyond this point, no equilibrium points exist, as shown in Figure 2.3(c), and the cantilever jumps into contact with the surface as the surface force dominates. (The critical point is an unstable point[79] and so when this point is reached, the cantilever will also jump to the surface.)

From Figure 2.3(b), the critical point is located at the point where $-F_{spr}$ is tangent to F_{surf}; therefore, the following two conditions are valid[79]

$$F_{surf} + F_{spr} = 0$$
$$\frac{\partial F_{surf}}{\partial z_s} + \frac{\partial F_{spr}}{\partial z_s} = 0 \tag{2.16}$$

Utilizing eq 2.9, and again noting that $d = z_s + R - z_P$, the critical point for a sphere interacting with an arbitrary surface is obtained from[101]

$$-\frac{4}{3\pi}\left(\frac{A}{k_c R^2}\right)\int_{-\infty}^{\infty}\int_{-\infty}^{\infty}\frac{dx_e^* dy_e^*}{\left[(x_e^* - x_s^*)^2 + (y_e^* - y_s^*)^2 + \left(h^* - z_{s,crit}^*\right)^2 - 1\right]^3} = z_{s,crit}^* - z_{p,crit}^* + 1 \tag{2.17}$$

$$\frac{8}{\pi}\left(\frac{A}{k_c R^2}\right)\int_{-\infty}^{\infty}\int_{-\infty}^{\infty}\frac{\left(z_{s,crit}^* - h^*\right)dx_e^* dy_e^*}{\left[(x_e^* - x_s^*)^2 + \left(y_e^* - y_s^*\right)^2 + \left(h^* - z_{s,crit}^*\right)^2 - 1\right]^4} = 1 \tag{2.18}$$

where $z_{s,crit}^* = z_{s,crit}/R$ and $z_{p,crit}^* = z_{p,crit}/R$ are the dimensionless z-positions of the sphere and platform, respectively, at the critical point.

Only $z_{s,crit}^*$ appears in eq 2.18, which is a consequence of the linear cantilever restoring force. Thus, for a given surface height function and value of A (as well as k_c and R), eq 2.18 is first solved for $z_{s,crit}^*$. This value of $z_{s,crit}^*$ is then substituted into eq 2.17 to determine $z_{p,crit}^*$. With $z_{s,crit}^*$ and $z_{p,crit}^*$ now known, the dimensionless deflection at first contact, $d_c^* = d_c/R$, can then be obtained. Since the critical point is also an unstable equilibrium location[79], upon reaching $z_{s,crit}^*$ the sphere then immediately jumps into contact with the surface while the location of the platform remains fixed at $z_{p,crit}^*$. Denoting the z-position of the center of the sphere when it first comes into contact with the surface as $z_{s,contact}$, the quasi-static deflection of the sphere at first contact is therefore given by[101]

$$d_c^* = z_{s,contact}^* - z_{p,crit}^* + 1 \tag{2.19}$$

where $z_{s,contact}^* = z_{s,contact}/R$.

For surfaces height functions of the form $h = h(x_e)$ (surfaces that are still two-dimensional because the shape in the x-direction is repeated without change in the y-direction), the simplifications of eqs 2.9, 2.17, and 2.18 for can be obtained by integrating each relation over the y-domain, and are as follows[101] (the simplification of eq 2.9 is eq 2.12)

$$-\frac{1}{2}\left(\frac{A}{k_c R^2}\right)\int_{-\infty}^{\infty}\frac{dx_e^*}{\left[(x_e^*-x_s^*)^2+\left(h^*-z_{s,crit}^*\right)^2-1\right]^{\frac{5}{2}}}=z_{s,crit}^*-z_{p,crit}^*+1 \tag{2.20}$$

$$\frac{5}{2}\left(\frac{A}{k_c R^2}\right)\int_{-\infty}^{\infty}\frac{\left(z_{s,crit}^*-h^*\right)dx_e^*}{\left[(x_e^*-x_s^*)^2+\left(h^*-z_{s,crit}^*\right)^2-1\right]^{\frac{7}{2}}}=1 \tag{2.21}$$

Similar to a previous method[79], the above general critical point conditions also connect A to the experimentally obtainable parameter d_c. Hence, eqs 2.17, 2.18, and 2.19 provide a means to infer the value of the Hamaker constant from known values of d_c. Because the deflection at first contact depends in general upon the horizontal location of the sphere as it approaches the surface the critical point conditions do not yield a single value of d_c. For each x_s and y_s, a different value of d_c may be obtained, and consequently a distribution of deflections at first contact or a d_c-distribution will develop for a given surface shape (and value of A). Since the surface height function is independent of x_s and y_s for a flat plate, there is only one relevant value of d_c for this surface. Thus, the d_c-distribution for a flat plate is a delta function. For other surface shapes, the resulting d_c-distribution will reflect the varying strengths of the vdW attractive force for different locations along the surface. Consequently, for a given Hamaker constant, the obtained d_c-distribution provides a "signature" of the effect of surface height variations, or roughness, on the resulting tip-surface vdW interactions. The approach-to-contact method presented previously[79,80], which "maps" a single (average) value of d_c to a corresponding value of A should

therefore be modified to instead "map" an experimentally obtained d_c -distribution to a corresponding (and presumably unique) value of A. A discussion of the effects of surface topography on the resulting d_c-distribution across a range of model surfaces is given in Chapter 3.

2.4 Determining the Point of First Contact between the Sphere and an Arbitrary Surface

The determination of d_c from eq 2.19 requires knowledge of $z_{s,contact}$, which is not obtained from the critical point conditions. Instead, a separate analysis must be performed to determine the vertical location of the sphere when it first comes into contact with the surface. For a sphere approaching a flat, nondeformable plate, the value of $z_{s,contact}$ is always equal to R, as the sphere always touches the surface at the same point located at the very bottom of the sphere. However, for a rough surface the very bottom of the sphere is not necessarily the point of first contact between the sphere and surface. Moreover, the point of first contact along the sphere surface will vary with the horizontal location of the sphere. This section considers the determination of $z_{s,contact}$ for surface height functions of two forms, $h = h(x_e)$ and $h = h(x_e, y_e)$.

Figure 2.4(a) shows a sphere in direct contact with a flat plate. If $x_{contact}$ denotes the x-position of that point along the sphere surface that is in contact with the surface, then for a flat plate, $x_s = x_{contact}$ (*i.e.,* the point of contact is directly below the center of the sphere)[101]. In addition, since for a flat plate $x_{contact}$ corresponds to the lowest vertical height on the sphere surface, then $z_{s,contact} = R$ (in which the plate is located at $z = 0$). Consequently, eq 2.19 indicates that $d_c^* = 2 - z_{p,crit}^*$.

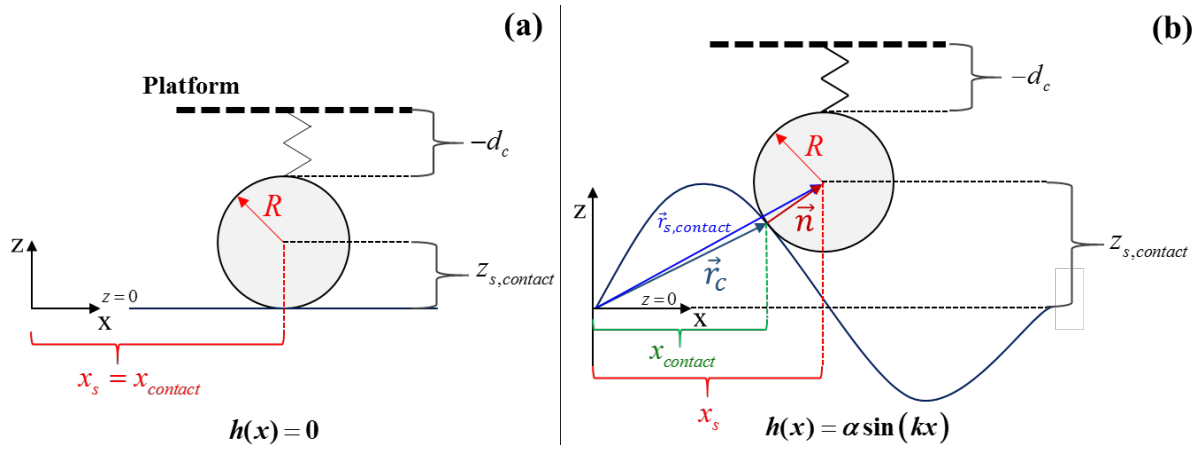

Figure 2.4 Schematic of an AFM cantilever tip (modeled as a sphere on a spring) making contact with (a) a flat plate and (b) a surface described by a sine wave with amplitude α and wavelength $2\pi/k$ (in which k is the wavenumber). R is the radius of the sphere, $z_{s,contact}$ is the vertical location of the sphere at contact, d_c is the deflection of the sphere at first contact, $\vec{r}_c$ is a vector from the origin to the point of contact of the sphere with the surface, $\vec{n}$ is a unit normal vector from the surface at the point of contact, and $\vec{r}_{s,contact}$ is a vector from the origin to the center of the sphere when in contact with the surface. x_s and $x_{contact}$ are the x-locations of the center of the sphere and the point of contact, respectively, both relative to the origin.

In Figure 2.4(b), the sphere (whose center is at the horizontal location x_s) is now in contact with a sine wave which is non-flat and nondeformable. In this case, $x_{contact} \neq x_s$ and $z_{s,contact} \neq R$, with $x_{contact}$ no longer representing that point on the surface of the sphere with the lowest vertical height. Now, $x_{contact}$ and ultimately $z_{s,contact}$ can be obtained through the use of the vectors defined in Figure 2.4 (b). The unit normal $\vec{n}$ pointing outward from the surface is given by[102]

$$\vec{n} = \frac{-h'\hat{\imath} + \hat{k}}{(1 + (h')^2)^{1/2}} \tag{2.22}$$

where h' is the first derivative of the surface height function with respect to x, and $\hat{\imath}$ and $\hat{k}$ are the unit vectors in the x- and z-directions, respectively. When the sphere touches the surface, the line between the sphere's center and point of contact is normal to the surface or perpendicular to the local surface tangent. Consequently, this point of contact and the center of the sphere are collinear

with $\vec{n}$. If $\vec{r}_c$ is the vector from the origin to the contact point of the sphere with the surface and $\vec{r}_{s,contact}$ is the vector from the origin to the center of the sphere (when in contact), then $\vec{r}_{s,contact} = \vec{r}_c + R\vec{n}$. Now, $\vec{r}_c = x_{contact}\,\hat{\imath} + z_{contact}\,\hat{k} = x_{contact}\,\hat{\imath} + h\,\hat{k}$, where $z_{contact} = h(x_{contact})$ is the vertical location of the point along the sphere that contacts the surface, and is simply the height of the surface at $x_{contact}$. Therefore,

$$\vec{r}_{s,contact} = \left[x_{contact} - \frac{Rh'}{(1+(h')^2)^{1/2}}\right]\hat{\imath} + \left[h(x_{contact}) + \frac{R}{(1+(h')^2)^{1/2}}\right]\hat{k} \qquad (2.23)$$

in which h' is also evaluated at $x_{contact}$. Since $\vec{r}_{s,contact}$ is also given by $\vec{r}_{s,contact} = x_s\,\hat{\imath} + z_{s,contact}\,\hat{k}$, eq 2.23 implies that

$$x_s = x_{contact} - \frac{Rh'}{(1+(h')^2)^{1/2}} \qquad (2.24)$$

$$z_{s,contact} = h(x_{contact}) + \frac{R}{(1+(h')^2)^{1/2}} \qquad (2.25)$$

Eqs 2.24 and 2.25 can be used to determine $z_{s,contact}$ for a given x_s, through the intermediate determination of $x_{contact}$ (first from eq 2.24). But for surfaces in which the sphere can no longer touch all points of the surface height function, eqs 2.24 and 2.25 give rise to multiple solutions for $z_{s,contact}$. Nonetheless, only one of these roots is physical (where the sphere only touches and does not penetrate the surface; for the remaining unphysical roots, a section of the sphere penetrates some portion of the surface). To avoid searching through all of these roots to find the single physical solution, an alternative procedure, called the "minimum distance method" (MDM) was developed.

Since the surface height functions currently being considered only vary in the x-direction, the bottom of the sphere (or in this case the lower half of the vertically oriented great circle) is first evenly discretized along the x-direction by n points over the domain of $x_s \pm R$, as shown in

Figure 2.5. Next, the vertical distance between a given point on the bottom of the sphere, located at a height z_{sphere}, and the corresponding point on the surface, $h(x)$, each at the same horizontal location x, is computed. As the sphere moves downward toward the surface, each of these vertical distances will decrease at the same rate. Hence, the x-location that yields the smallest value of these vertical distances will be the corresponding point of contact when the sphere first touches the surface (for the fixed value of x_s). For any chosen value of z_s, $x_{contact}$ can therefore be identified by finding the minimum value of $z_{sphere}(x) - h(x)$, or $x_{contact} \Leftrightarrow min\left[z_{sphere}(x) - h(x)\right]$, where $\Leftrightarrow$ implies "corresponds to" and $z_{sphere} = z_s - (R^2 - (x - x_s)^2)^{1/2}$ describes the bottom half of a circle of radius R whose center is located at x_s and z_s. With $x_{contact}$ now known, $z_{s,contact}$ is then determined from eq 2.25. (Note that the MDM immediately identifies the only physical solution of eq 2.25.)

To ensure that $x_{contact}$ was obtained with sufficient precision, the degree of discretization, n, of the bottom of the sphere was varied. For most surfaces of interest, $n \approx 1000$ yielded precise enough results. For more complicated surfaces, with features with short wavelengths, an initial value of $n \approx 1000$ was chosen to obtain a reasonable first guess for $x_{contact}$. Then, a finer discretization was carried out around this initial estimate to determine $x_{contact}$ with even higher precision. With the MDM in place, for a given location along the surface, $x_{contact}$ can be found, followed by $z_{s,contact}$ using eq 2.25.

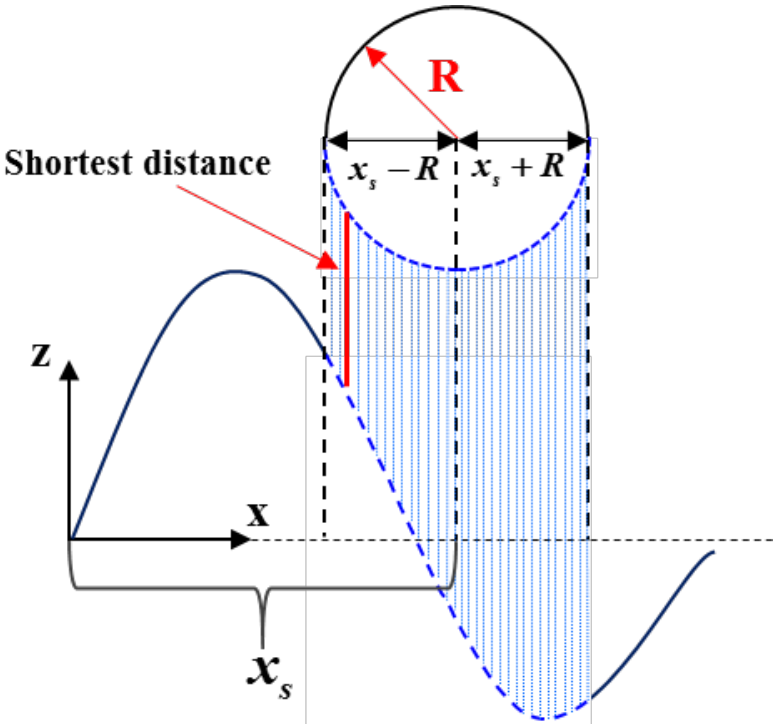

Figure 2.5 Schematic illustration of the minimum distance method, in which the vertical distances (represented by the blue solid lines) between points along the bottom of the sphere and the surface are first determined. The location with the smallest vertical distance, represented by the bold red line, corresponds to the x-position along the bottom of the sphere that will be the point of first contact of the sphere and the surface. The center of the sphere is at a horizontal distance x_s from the origin and R is the radius of the sphere. The blue dashed lines represent those portions of the surface and the sphere that may come into contact.

The MDM can also be generalized to any AFM cantilever tip shape and to surface height functions that depend upon both the x- and y-directions. For the coordinate system defined in Figure 2.6, x_s and y_s denote the horizontal location of the center of the sphere, while z_s denotes its vertical location (relative to a reference plane at $z = 0$). When the sphere is in contact with the surface, $h(x, y)$, as shown in Figure 2.6, the common point between the sphere and surface is located at $x_{contact}$, $y_{contact}$ and $z_{contact} = h(x_{contact}, y_{contact})$. For a flat plate, in which $h = 0$, $x_{contact} = x_s$, $y_{contact} = y_s$, and $z_{contact} = 0$, corresponding to the point of contact being at the

lowest vertical height on the sphere surface. Thus, $z_{s,contact} = R$. But in general, for any other shaped surface, $x_{contact} \neq x_s$ and $y_{contact} \neq y_s$, as well as $z_{s,contact} \neq R$.

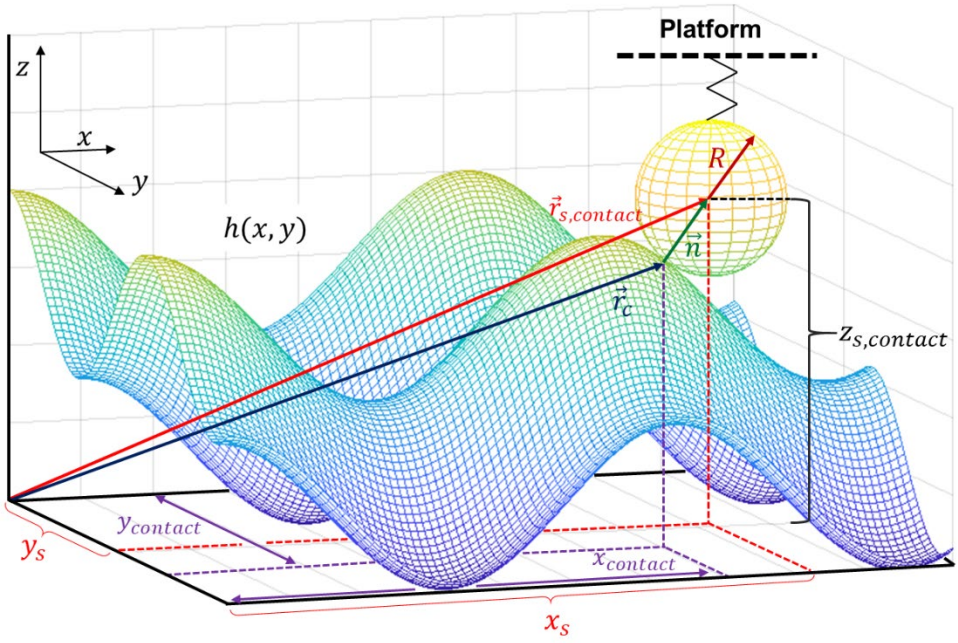

Figure 2.6 Schematic of an AFM cantilever tip modeled as a sphere attached to a horizontal platform via a Hookean spring, in which the sphere is in direct contact with a surface described by the surface height function $h(x, y)$. R is the radius of the sphere, $z_{s,contact}$ is the vertical location of the sphere center at contact, $\vec{r}_c$ is a vector from the origin to the point of contact of the sphere with the surface, $\vec{n}$ is a unit normal vector from the surface at the point of contact, and $\vec{r}_{s,contact}$ is a vector from the origin to the center of the sphere when in contact with the surface. x_s and $x_{contact}$ are, for example, the x-locations of the center of the sphere and the point of contact, respectively, both relative to the origin.

The values of $x_{contact}$, $y_{contact}$, and ultimately $z_{s,contact}$ can be obtained using the vectors, $\vec{r}_{s,contact}$, $\vec{r}_c$ and $\vec{n}$, shown in Figure 2.6. The unit normal $\vec{n}$ pointing outward from the surface in the positive z-direction is given by[102]

$$\vec{n} = \frac{-h'_x\hat{\imath} - h'_y\hat{\jmath} + \hat{k}}{\left(1 + (h'_x)^2 + \left(h'_y\right)^2\right)^{1/2}} \tag{2.26}$$

where h'_x and h'_y are the first partial derivatives of the surface height function with respect to x and y, respectively, and $\hat{\imath}$, $\hat{\jmath}$, and $\hat{k}$ are the unit normal vectors in the x, y, and z directions. The vector from the origin to the center of the sphere (when in contact with the surface) is $\vec{r}_{s,contact}$, in which $\vec{r}_{s,contact} = \vec{r}_c + R\vec{n}$ and where $\vec{r}_c$ is the vector from the origin to the point of contact that the sphere makes with the surface. Since $\vec{r}_c = x_{contact}\hat{\imath} + y_{contact}\hat{\jmath} + z_{contact}\hat{k}$ and $z_{contact} = h(x_{contact}, y_{contact})$, then

$$\vec{r}_{s,contact} = \left[x_{contact} - \frac{Rh'_x}{\left(1 + (h'_x)^2 + \left(h'_y\right)^2\right)^{1/2}}\right]\hat{\imath} + \left[y_{contact} - \frac{Rh'_y}{\left(1 + (h'_x)^2 + \left(h'_y\right)^2\right)^{1/2}}\right]\hat{\jmath} + \left[h(x_{contact}, y_{contact}) + \frac{R}{\left(1 + (h'_x)^2 + \left(h'_y\right)^2\right)^{1/2}}\right]\hat{k} \tag{2.27}$$

Eq 2.27 thus implies that

$$z_{s,contact} = h(x_{contact}, y_{contact}) + \frac{R}{\left(1 + (h'_x)^2 + \left(h'_y\right)^2\right)^{1/2}} \tag{2.28}$$

with h'_x and h'_y evaluated at $x_{contact}$ and $y_{contact}$. Before eq 2.28 can be used to determine $z_{s,contact}$ for a given x_s and y_s, $x_{contact}$ and $y_{contact}$ must first be determined using the minimum distance method, now extended to a surface described by $h(x, y)$. As shown in Figure 2.7, and similarly to the case in which $h(x)$, the bottom of the sphere is discretized into $n \times n$ total points over the domain of $x_s \pm R$ and $y_s \pm R$. The vertical distance between a given point on the bottom of the sphere, at height z_{sphere}, and the corresponding point on the surface, $h(x, y)$, directly below is determined.

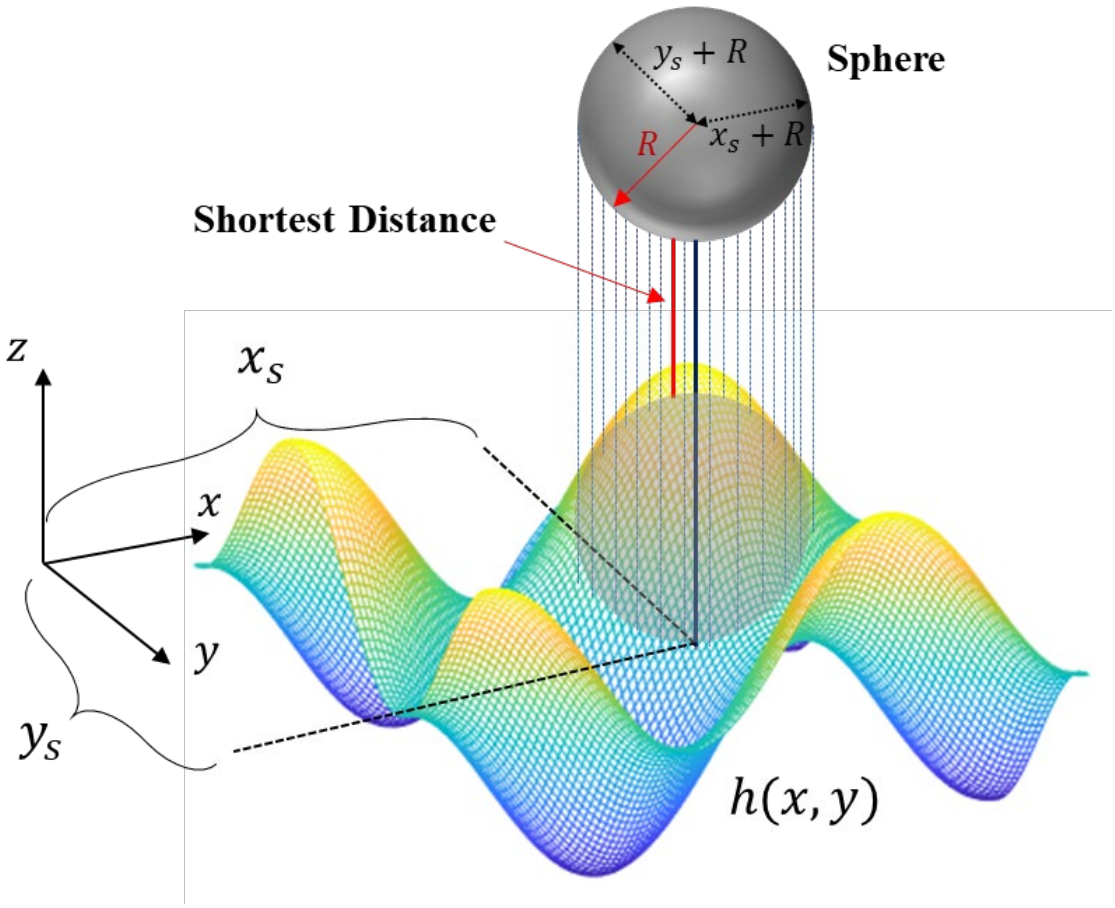

Figure 2.7 Illustration of the two-dimensional minimum distance method. The solid blue vertical lines represent the vertical distances between points along the bottom hemisphere and the corresponding points on the surface height function, $h(x, y)$. The shortest distance, represented by the solid red vertical line, corresponds to the (x, y)-position that is the point of first contact between the sphere and surface. The center of the sphere is located at a horizontal distance (x_s, y_s) from the origin and R is the radius of the sphere.

The x, y-location yielding the smallest value of each vertical distance identifies the point of first contact between the sphere and the surface, or $x_{contact}$ and $y_{contact}$. Thus, for a particular choice of x_s and y_s, $x_{contact}$ and $y_{contact}$ are determined by finding the minimum value of $z_{sphere}(x, y) - h(x, y)$, where $z_{sphere} = z_s - (R^2 - (x - x_s)^2 - (y - y_s)^2)^{1/2}$ describes the bottom half of a circle of radius R whose center is located at (x_s, y_s) and z_s. Within the MDM, the chosen vertical location of the sphere center, z_s, is arbitrary, as long as the sphere is above all

relevant surface features. Finally, with $x_{contact}$ and $y_{contact}$ now known, $z_{s,contact}$ is then determined from eq 2.28.

2.5 Summary

This chapter presented the development of a novel vdW force expression describing the interaction between an AFM cantilever tip, treated as an effective sphere, and surface of arbitrary roughness. For a surface height function, h, the deflection of the cantilever at first contact with the surface was determined from the critical point derived under the quasi-static limit as well as the point of first contact between the sphere and surface. With this method is place, Chapter 3 provides a discussion of the effects of surface geometry on plots of $z_{s,contact}$ as a function of x_s and y_s, which are henceforth called "contact locus" and "contact mesh" plots for several surface height functions.

3. ANALYSIS OF QUASI-STATIC d_c-DISTRIBUTIONS FOR VARIOUS MODEL SURFACES

3.1 Introduction

Inherent surface roughness is the primary reason for the emergence of a distribution of deflections at first contact, even for a surface like amorphous silica, which can be made "relatively" smooth. Because of surface roughness, different values of d_c will be obtained as the tip accesses spatially separate surface positions (*i.e.*, probes the "global" roughness), and as the tip attempts to access the same surface position but cannot do so exactly (*i.e.*, probes the "local" roughness) due to the inevitable horizontal drift of the cantilever.[81–84] Both of these effects were presumably observed in the AFM force measurements reported by Fronczak *et al.*[79,80] Consequently, a characteristic distribution of d_c-values (or a d_c-distribution) should be observed for a given surface (and chosen cantilever properties), providing a signature of the underlying surface roughness. Even two substrates with the same values of A should nonetheless yield two different d_c-distributions if their individual surface roughness is also different. This chapter is concerned with studying the effects of surface geometry on the resulting d_c-distributions, in the quasi-static limit, for several surface height functions of the form $h(x)$ and $h(x, y)$.

3.2 Analysis of the Effect of Surface Topography on the Resulting d_c-Distributions for Surface Height Functions of the Form $h(x)$

As a preliminary test of the modified approach-to-contact method, this section considers surfaces which vary only in the x-direction, or surface height functions of the form $h(x)$. For a given surface height function, the locus of the sphere's center when it is contact with the surface, or a plot of $z_{s,contact}$ as a function of x_s, is determined from the MDM (see 43). Three examples

(surfaces A, B, and C) of this "contact locus" are provided in Figure 3.1 for the surface height function given, in general as

$$h = \alpha \sin(kx) \tag{3.1}$$

where α is the amplitude and $k = 2\pi/\lambda$ is the wavenumber (and λ is the wavelength). $\alpha/R = 0$, 1, and 3 for surfaces A, B, and C, respectively, and in all cases, $kR = 1$.

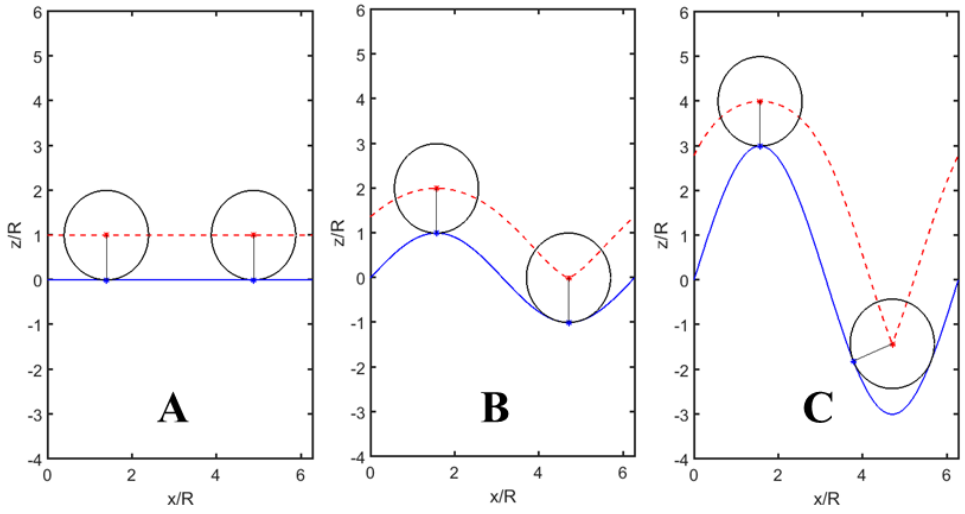

Figure 3.1 Plots of the contact locus for three surfaces described, in general, by eq 3.1. For each surface, $kR = 1$, or $\lambda/R = 2\pi$ (with $k = 2\pi / \lambda$), while $\alpha/R = 0$, 1, and 3 for surfaces A, B, and C, respectively. The blue line represents the surface and the red dashed line represents the contact locus, *i.e.*, the curve that corresponds to the center of the sphere when it is in contact with the surface. For a given location of the center of the sphere (red dot), the corresponding point on the surface that makes contact with a point on the sphere are both highlighted by the same blue dot. The center of the sphere and this contact point are connected by a black line.

The contact locus for a smooth, flat plate (surface A where $\alpha = 0$) is provided for reference, for which $x_{contact} = x_s$ and $z_{s,contact} = R$ all along the surface. For surface B ($\alpha/R = 1$), $z_{s,contact}$ varies with x_s and $x_{contact} \neq x_s$ except at $x_s = \pi/2$ or $3\pi/2$ (*i.e.*, at the top of the hill or at the bottom of the valley). The radius of curvature of B at the bottom of the valley ($x_s = 3\pi/2$) is equal to that of the sphere. Consequently, the sphere is able to make contact with all

portions of the surface, and the contact locus curve is differentiable everywhere. For surface C ($\alpha/R = 3$), its radius of curvature is now less than that of the sphere at $x_s = 3\pi/2$, and so the sphere is unable to reach the bottom of the valley. As a result, the contact locus forms a corner at this point, where the slopes on either side are finite but different (*i.e.*, discontinuous).

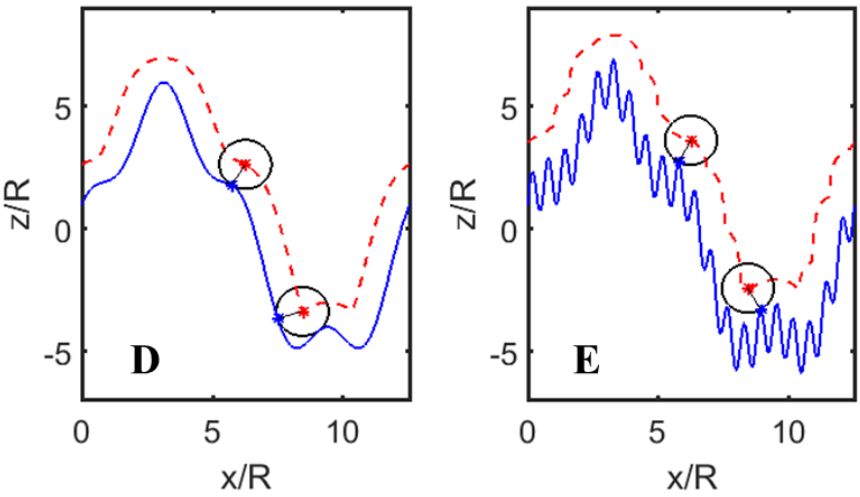

Figure 3.2 Plots of the contact locus for two surfaces described, in general, by eq 3.2. $\alpha/R = 1$ and $\beta/R = 5$ for surface D and E, while γ/R = 0 and 1 for surface D and E, respectively. In all cases, $kR = 2$, $cR = 0.5$, and mR = 10. The blue line represents the surface and the red dashed line represents the contact locus. For a given location of the center of the sphere (red dot), the corresponding point on the surface that makes contact with a point on the sphere are both highlighted by the same blue dot. The red and blue dots are connected by a black line.

Figure 3.2 shows the contact loci of two additional surfaces (E and D), both of which are described by a summation of sines and cosines given, in general, as

$$h/R = \alpha\cos(kx/R) + \beta\sin(cx/R) + \gamma\sin(mx/R) \qquad (3.2)$$

where α, β, and γ are the amplitudes of terms 1, 2, and 3, respectively, and $k = 2\pi/\lambda$ is the wavenumber. $\alpha/R = 1$ and $\beta/R = 5$ for surface D and E, while γ/R = 0 and 1 for surface D and E, respectively. In all cases, $kR = 2$, $cR = 0.5$, and mR = 10.

Surface E includes an additional sine term, which adds smaller scale roughness to surface D. Since this additional roughness operates on a relatively small wavelength, the two contact loci are quite similar in appearance. But as will be discussed further below, the presence of this small-scale roughness serves to vary the amount of substrate material that is close to the sphere. Consequently, the force interactions between surface D and the sphere, and that between surface E and the sphere, may be quite different. Hence, the d_c-distributions for these two surfaces may likewise be very different.

For the surfaces in Figures 3.1 and 3.2, with the contact loci now known, the corresponding d_c-distributions were then obtained (in the quasi-static limit). The following parameters, similar to those used by Fronczak et al.[79], were chosen: $A = 101$ zJ, $R = 100$ nm, and $k_c = 0.1$ N/m. For each surface, 1000 equally spaced x_s-values over one complete period of the surface height function were selected (*i.e.*, x_s was chosen, for example for Figure 3.1, to reside between 0 and $2\pi R$, including 0 only). Then, for each x_s, $z_{s,contact}$ and the deflection at first contact were obtained using eqs 2.17 – 2.19. The resulting d_c-distributions are provided in Figures 3.3 and 3.4 for the surfaces in Figures 3.1 and 3.2.

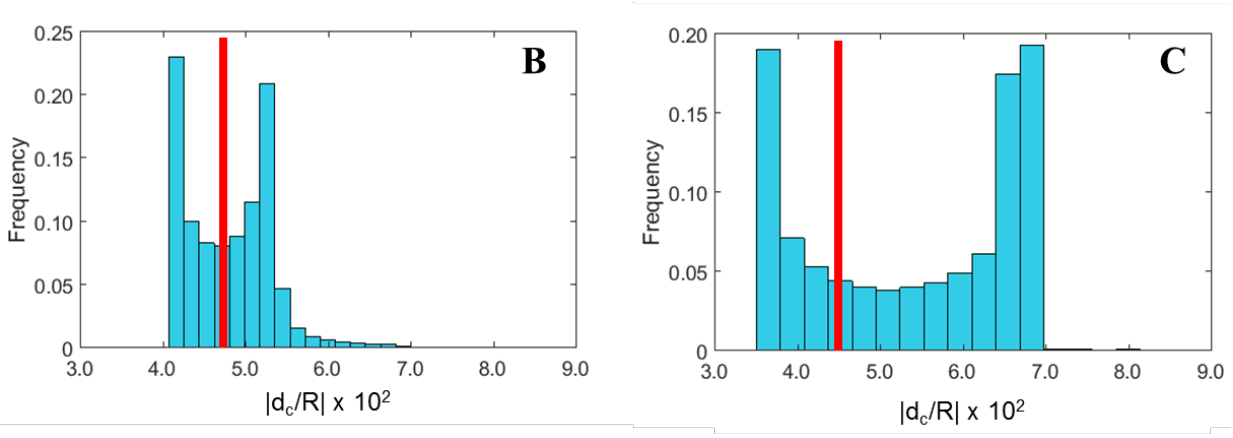

Figure 3.3 The corresponding d_c-distributions for surfaces B and C in Figure 3.1. Here, $A = 101$ zJ, $R = 100$ nm, and $k_c = 0.1$ N/m, which yields $|d_c^*| = |d_c/R| = 0.0479$ for the flat plate (surface A) and is indicated by the vertical red line.

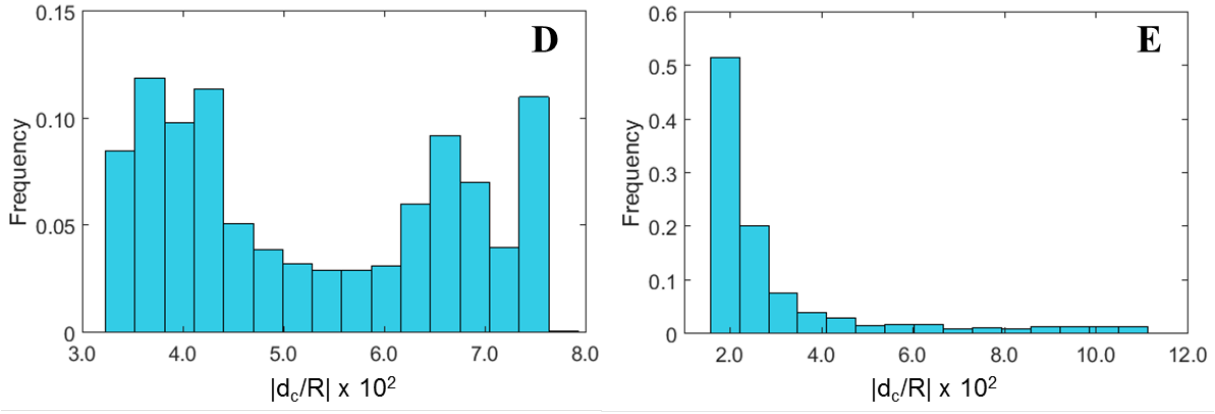

Figure 3.4 The corresponding d_c-distributions for surfaces D and E in Figure 3.2. Here, $A = 101$ zJ, $R = 100$ nm, and $k_c = 0.1$ N/m.

The underlying geometry of the surface is seen to have an impact on the resulting shape of the d_c-distribution. As the sphere approaches different locations along the surface, the magnitude of the vdW force will vary (for a given surface-sphere separation distance), as the sphere interacts with varying amounts of substrate material. Hence, the sphere will reach a critical point at different heights along the surface. Given the additional differences in the contact loci, variations in the deflections at first contact are likewise observed.

Surface C has the same wavelength as surface B but with an amplitude that is three times larger. The shapes of the corresponding d_c-distributions of B and C are therefore similar, albeit with key differences. The d_c-distribution of C is much broader, ranging from $|d_c^*| = 0.0379$ to 0.0814. The first peak shifts to a smaller deflection because of the higher negative curvature around the peak of the surface (more substrate material is moved away from the sphere as compared to B). Comparably, the valleys have a larger positive curvature, leading to larger deflections. Here, more substrate material is located near the approaching sphere, in which both sides of the valley are now able to strongly attract the sphere. Although d_c increases as the sphere approaches the valley (with the second peak of the d_c-distribution of C shifting to higher values),

the maximum deflection is, however, not much greater than that of the d_c-distribution of B. The sphere cannot touch the bottom of the valley of C, and thus the surface geometry limits the allowed deflection in this region.

Interestingly, the d_c-distribution for surface D is not very different from that for surface C, despite the very different underlying surface height functions. Although these two distributions are not identical, their overall ranges are comparable. This similarity in the two distributions may appear because, generally speaking, both surfaces give rise to similar geometric effects (*e.g.*, sharp peaks and valleys that the sphere cannot touch). On the other hand, surface E yields a very different d_c-distribution. Even though the contact loci of surfaces D and E are very similar, the small-scale roughness appearing within E gives rise to very different vdW attractive forces between the sphere and the surface. Hence, only a single peak at small deflections ($|d_c^*| \approx 0.022$) appears in the d_c-distribution of E, with a very broad tail. Because of this small-scale roughness, the amount of substrate material with which the sphere interacts at close separations rapidly varies as the sphere moves along the surface. The vdW force between the sphere and E can therefore be either much greater than or less than what arises for D. As a result, the maximum deflection of the d_c-distribution for E now occurs at $|d_c^*| \approx 0.118$, a much larger value than what is obtained for D, and even B and C.

Interestingly, the rather simple surfaces B and C give rise to a bimodal d_c-distribution, with a tail of large deflections. For the d_c-distribution corresponding to surface B in Figure 3.1, the magnitude of d_c^* ranges from 0.0426 to 0.0702; the first peak is around $|d_c^*| = 0.04$, corresponding to the sphere approaching the surface for locations centered around the top of the sine wave ($x_s/R \sim x_{contact}/R \sim \pi/2$). As shown in Figure 3.5(a), when the sphere is near this peak, the surface is curved away from the bottom of the sphere. Compared to a flat plate at the same

relative separation (which yields $|d_c^*| = 0.0479$), the vdW force interaction is weaker since less substrate material is close to the sphere. Consequently, the deflection at first contact is smaller.

As the sphere moves away from the peak, $|d_c^*|$ increases. For example, at $x_s/R = 3.85$, which corresponds to $x_{contact}/R = \pi$, $|d_c^*| = 0.0539$. This contact location corresponds to the point where the surface has zero curvature as shown in Figure 3.5(b), and thus is analogous to the sphere approaching a tilted flat plate. As discussed in the next section, the tilting of an initially horizontal plate results in a net increase in the amount of material near the sphere as it approaches the plate. Hence, the vdW force, and ultimately $|d_c^*|$, increases relative to the horizontal plate.

Finally, $|d_c^*|$ reaches its largest value of 0.0702 at $x_s/R = x_{contact}/R = 3\pi/2$, the location of the local minimum or valley of the surface. Here, as illustrated in Figure 3.5(c), the surface is curved towards the sphere. More of the surface is closer to the sphere, as compared to the corresponding flat plate, and thus $|d_c^*|$ is larger.

As a side note, surface geometry affects the shape of the resulting d_c-distribution in two other related ways. Similar to what is done in an AFM experiment, the horizontal position of the sphere center, or cantilever tip, is sampled uniformly in the x-direction, where again 1000 equally spaced x_s-values were chosen over one complete period of the surface height function. But as, in general, $x_s \neq x_{contact}$, uniform sampling in x_s does not correspond to uniform sampling in $x_{contact}$. Concurrently, uniform sampling in the x-direction does not result in uniform sampling along the arc length, s, of the surface, in which $\Delta s \approx \Delta x(1 + (h')^2)^{1/2}$. Hence, regions along the surface with non-zero slope are "under-represented" in the d_c-distribution, for which $\Delta s > \Delta x$, compared to those points around the maximum and minimum of the surface, for which $\Delta s \approx \Delta x$. These two effects also contribute to the resulting bimodal shape of the d_c-distribution.

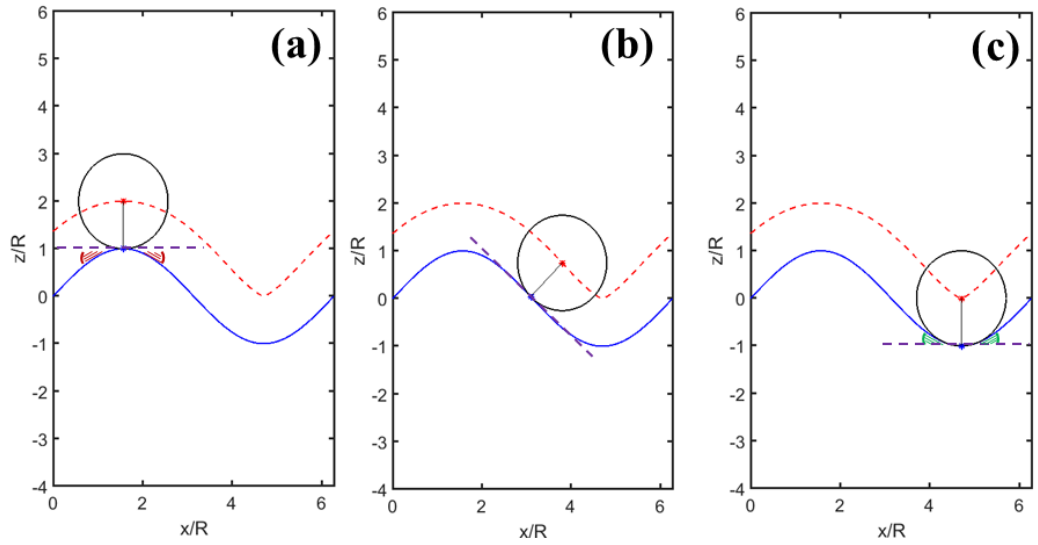

Figure 3.5 Illustration of the dependence of d_c on the curvature of the surface for various contact points of the sphere with surface B in Figure 3.1. a) The sphere approaches the peak of the surface ($x_s/R = x_{contact}/R = \pi/2$). The red areas correspond to the substrate material that is no longer interacting with the sphere, as compared to the appropriate flat plate. b) The sphere is in contact with the surface at the point in which its curvature is zero ($x_s/R = 3.85$; $x_{contact}/R = \pi$). This situation is analogous to the sphere approaching a tilted flat plate. c) The sphere approaches the valley of the surface ($x_s/R = x_{contact}/R = 3\pi/2$). The green areas correspond to the additional substrate material that is closer to the sphere, as compared to the appropriate flat plate. The purple dashed lines correspond to the appropriate flat plate at each contact point. The red dashed line is the contact locus and the blue solid line is the surface.

The effect of decreasing the amplitude of B was also investigated. As shown in Figure 3.6, as the amplitude goes to zero, for a fixed wavelength, the d_c-distribution becomes a delta function centered about $|d_c^*| = 0.0479$ (since in this limit the surface is becoming a flat plate).

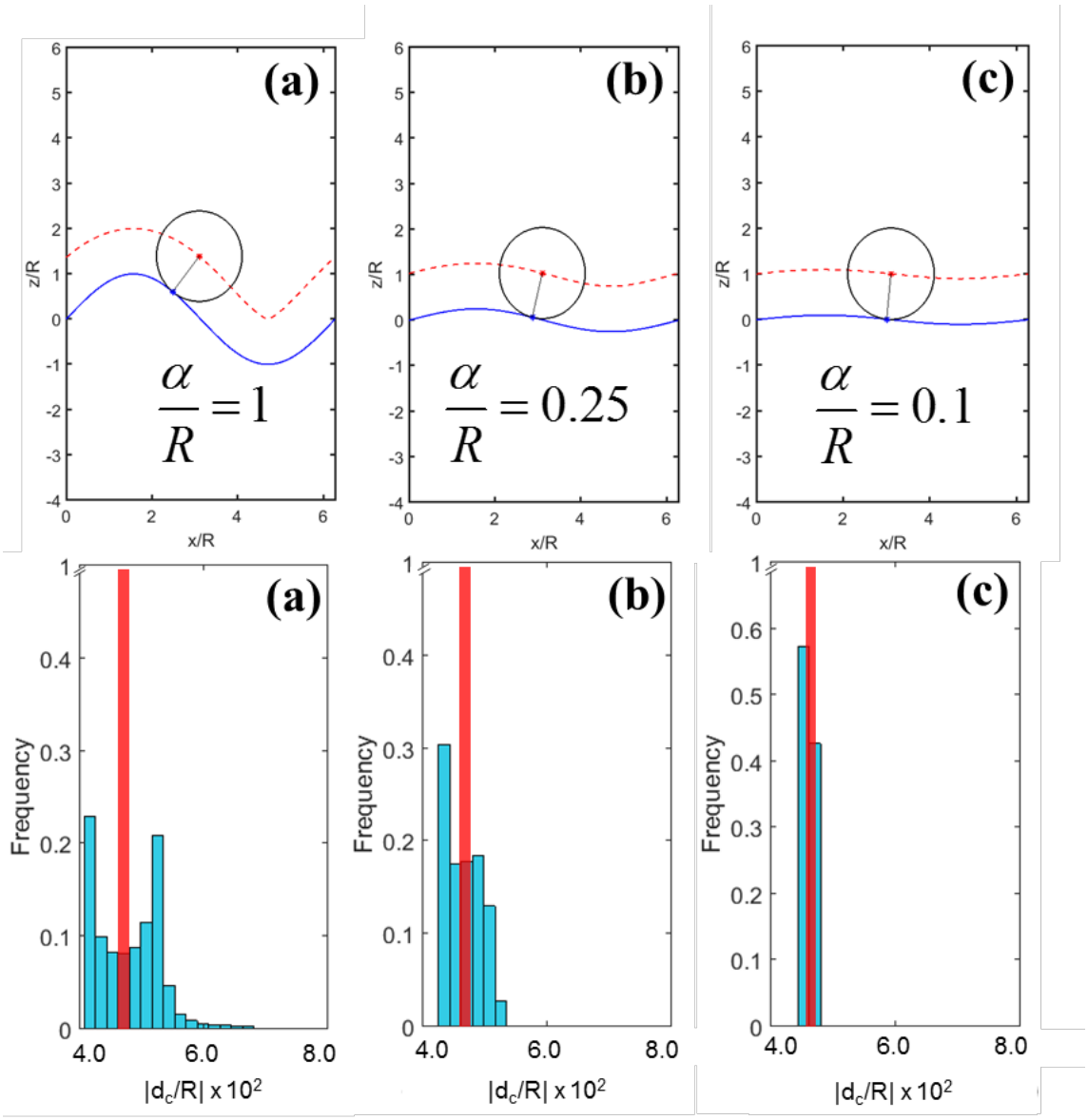

Figure 3.6 Contact loci and corresponding d_c-distributions for three surfaces described by the surface height function $h = \alpha \sin(kx)$. For each surface, $kR = 1$, or $\lambda/R = 2\pi$ (with $k = 2\pi / \lambda$), while $\alpha/R =$ 1, 0.25, and 0.1. In each of the bottom plots, the red vertical line corresponds to the d_c-distribution of a flat plate, which is a delta function centered about $|d_c^*| = 0.0479$.

A similar analysis can be performed for a surface described by a series of hemispheres with the same radius $R_H^* = R_H/R$ separated by the distance $L^* = L/R$ (shown in Figure 3.7 for $R_H^* = 1$ and $L^* = 1$). A version of this type of surface has been used previously as a model of surface roughness.[95] The contact locus for this surface, also provided in Figure 3.7, shows that the sphere

can make contact along every point along each hemisphere except for a range of x/R-values from, for example, 2.7 to 3, where a corner forms. At these corners of the contact locus, the sphere straddles two adjacent hemispheres and cannot touch the bottom of the surface at $z = 0$.

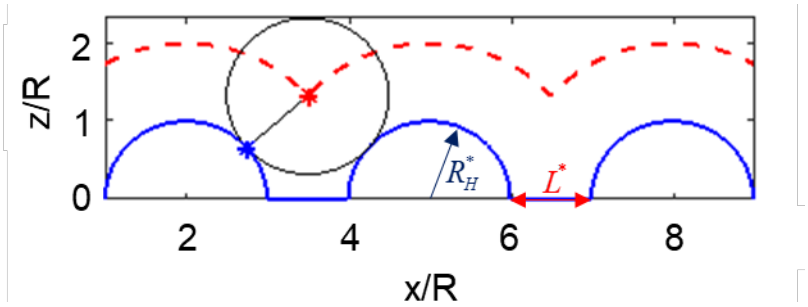

Figure 3.7 The contact locus (red dashed line) for a surface (solid blue line) described by a series of hemispheres with radius $R_H^* = R_H/R = 1$, each separated by a distance $L^* = L/R = 1$ from any other. For a given location of the center of the sphere (red circle), the corresponding point on the surface that makes contact with a point on the sphere (both of which are highlighted by the same blue circle) is also indicated. Both of these points are connected by a black line.

Contact locus plots for hemispheres of radius $R_H^* = 1$ and $L^* = 0, 1$, and 2 are shown in Figure 3.8(a), Figure 3.8(b), and Figure 3.8(c), respectively. In Figure 3.8(a) and Figure 3.8(b), cusps appear at the point where the sphere straddles two adjacent hemispheres ($L^* = 0$ and 1, respectively). In Figure 3.8(c), when $L^* = 2$, the sphere can touch the flat portions of the surface in between any two adjacent hemispheres. Nevertheless, new cusp points arise when the sphere simultaneously touches the flat surface and the side of a hemisphere (e.g., at $x_s/R \approx 4.73$).

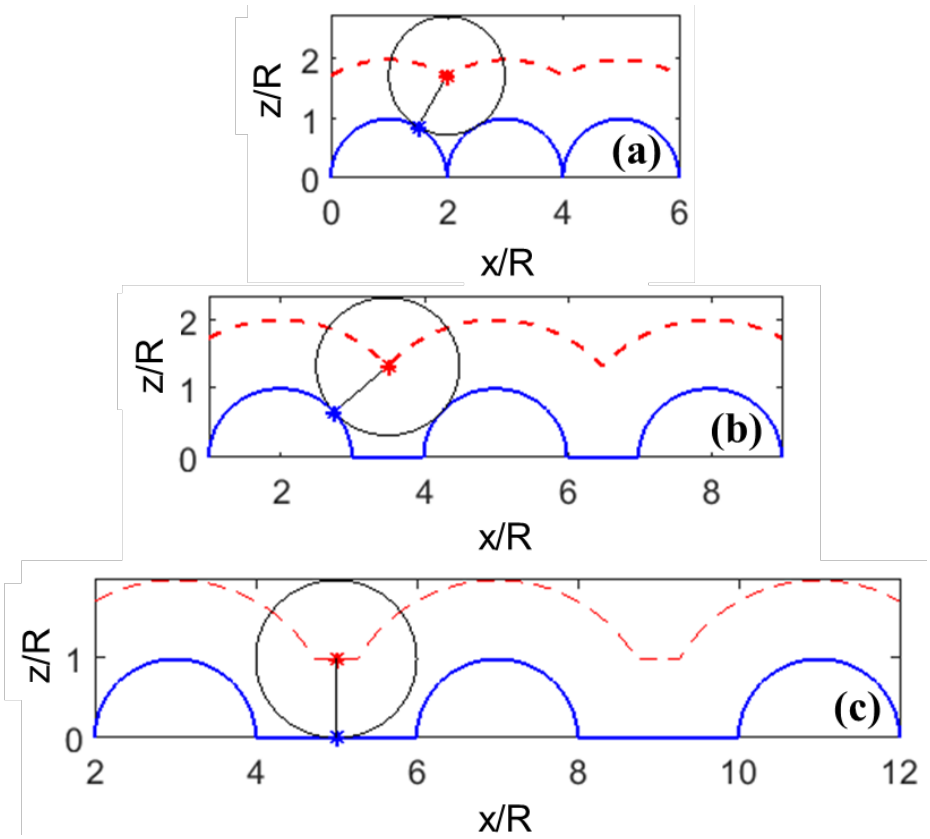

Figure 3.8 Contact locus plots of three surfaces comprised of several hemispherical asperities of radius R_H^*. The red dashed lines are the contact loci and the blue lines are the surfaces. The asperities are separated by distances $L^* = 0, 1,$ and 2.

The corresponding d_c-distributions for the surfaces shown in Figure 3.8 are shown in Figure 3.9. Each d_c-distribution has a large peak ($|d_c^*| \approx 0.042$) followed by a tail. The contact locus varies the least along the surface for $L^* = 0$. Since the distribution of vdW forces for this surface also varies the least, its d_c-distribution exhibits the largest peak with the smallest tail. Figure 3.8(c) shows that for a large enough gap between adjacent hemispheres (when $L^* = 2$), the range of the d_c-distribution is the greatest as more of the total surface is sampled, as the sphere can now make contact with the very bottom of the surface. For those contact points between any two hemispheres, this surface essentially appears to the sphere to be a flat plate, and so $|d_c^*| \approx 0.0479$ at these locations. The maximum d_c-value ($|d_c^*| \approx 0.0628$) occurs where the sphere

touches both the bottom of the surface and the side of a hemisphere. Figure 3.9(a) and Figure 3.9(b) are similar in appearance as the sphere cannot touch the bottom of either one of these surfaces, but when $L^* = 1$, more of each hemisphere can be sampled and so the peak in Figure 3.9(b) is smaller.

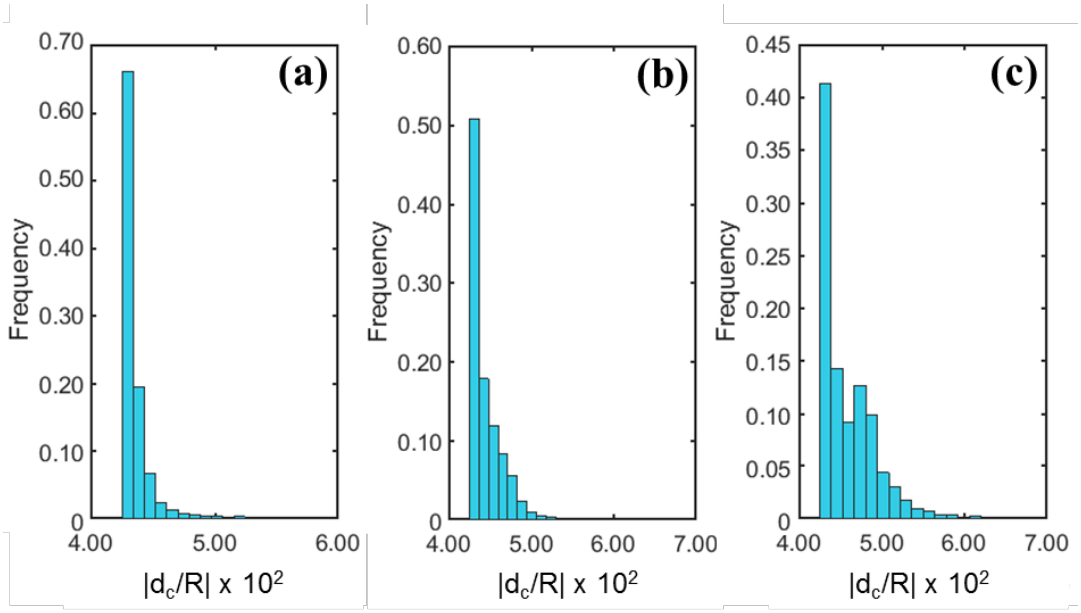

Figure 3.9 Corresponding d_c-distributions for the surfaces described, in general, in Figure 3.8. For each distribution, $R_H^* = R_H/R = 1$ while $A = 101$ zJ, $R = 100$ nm, and $k_c = 0.1$ N/m, while a) $L^* = L/R = 0$, b) $L^* = 1$, and c) $L^* = 2$.

A similar analysis can be made for a surface described by a series of "scoops" (or inverted hemispherical asperity) instead of hemispheres. Contact locus plots are shown in Figure 3.10 for surfaces with (a) $R_H^* = R_H/R = 1$, $L^* = 0$, (b) $R_H^* = 1$, $L^* = 1$, and (c) $R_H^* = 2$, $L^* = 2$. Because the sphere can come into contact a t certain points along these surfaces for which the corresponding surface height functions are not differentiable (e.g., at $x/R = 2$ and 4 in Figure 3.10(a) and $x/R = 4$ and 6 in Figure 3.10(b)), the surfaces must therefore be "rounded off" (i.e., made differentiable) at these points to ensure that the minimum distance method for finding the sphere-surface contact

points is still applicable. This "rounding off" was done by fitting cubic Hermite splines (of very limited ranges) around these points, thereby generating a fully differentiable surface height function.[4]

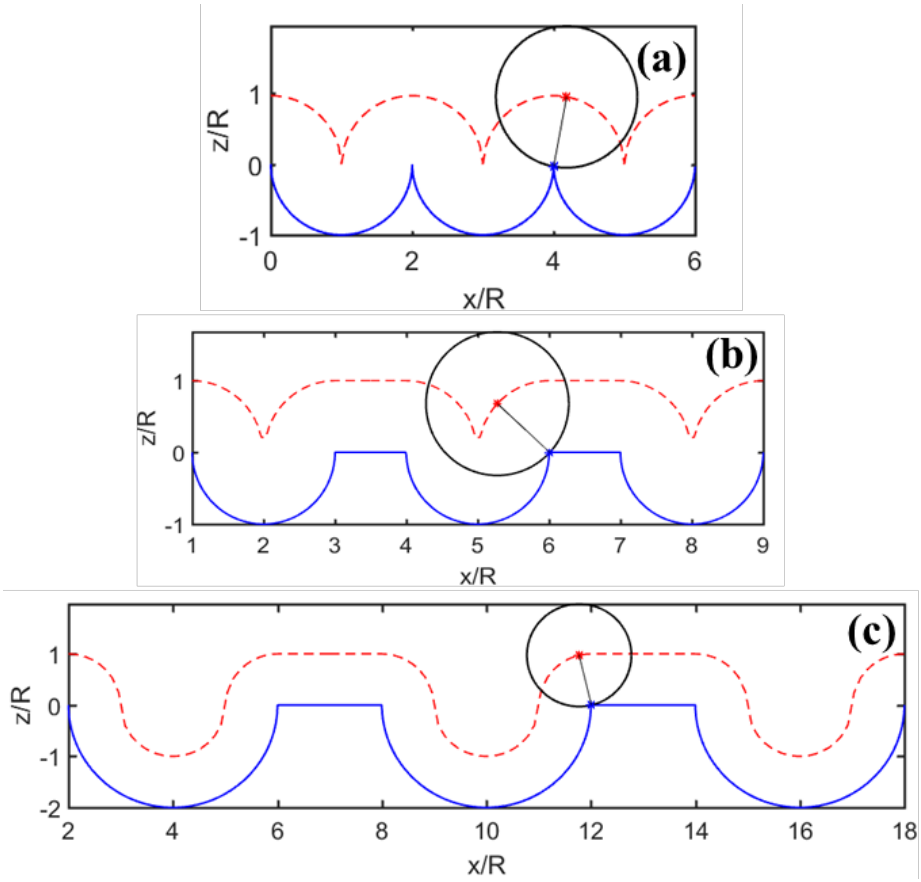

Figure 3.10 Contact locus plots of three surfaces comprised of several "scoops" of radius R_H^*. The red dashed lines are the contact loci and the blue lines are the surfaces. The scoops are separated by distances $L^* = 0, 1,$ and 2, and $R_H^* = 1, 1,$ and 2.

The corresponding d_c-distributions for the surfaces in Figure 3.10 are shown in Figure 3.11. Figure 3.11(a) shows a large initial peak around $|d_c^*| \approx 0.01$ and a long tail. The maximum value of $|d_c^*| \approx 0.13$ which corresponds to where the sphere can fit perfectly into the scoop, occurring at $x_s/R = 1, 3, 5,$ etc. The large initial peak results from the sphere touching the top/sides of the

scoop around $x/R = 0, 2, 4,$,etc., which occurs for almost all values of x_s/R. At these points, the sphere interacts with only a small portion of the surface and so $|d_c^*|$ is relatively small.

Figure 3.11(b) shows a bimodal d_c-distribution, which results from the sphere either touching the side of the scoop/flat plate interface at $x/R = 1,3, 4, 6,$ etc., or along the flat plate portions of the surface where $|d_c^*|$ varies slightly (this section of the surface contributes to the smaller peak where $|d_c^*| \approx 0.0479$, the corresponding value for a flat plate). Figure 3.11(c) shows a trimodal d_c-distribution; the flat plate portion of the surface contributes to the middle peak at $|d_c^*| \approx 0.0479$. The additional peak in the distribution arises from the ability of the sphere to interact with more of the surface around the bottom of the scoop where $|d_c^*|$ is roughly the same.

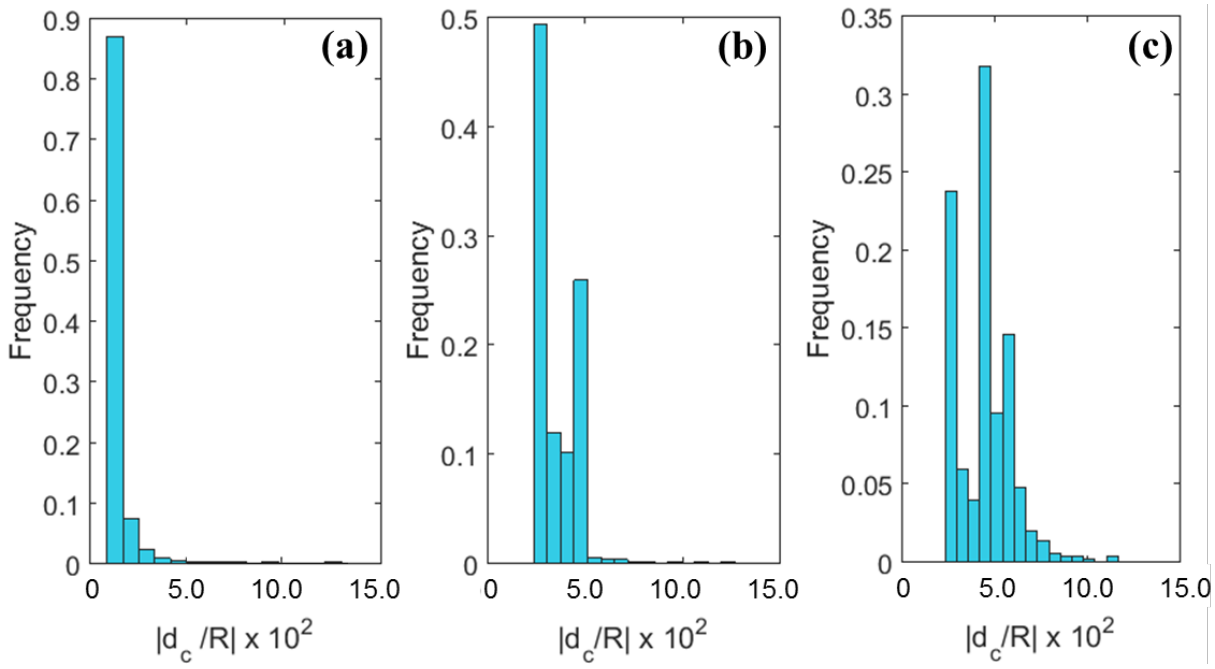

Figure 3.11 Corresponding d_c-distributions for the surfaces shown in Figure 3.10.

An additional analysis demonstrates the effect of increasing the size of the sphere relative to the size of the asperities in the surface shown in Figure 3.8(a), where $L^* = 0$. Figure 3.12(a)-

(c) contain the contact loci for $R_H^* = 1, 0.5$, and 0.2 (or equivalently when the sphere radius is either the same size, twice as large, or five times as large as the radius of a hemisphere). As the radius of the sphere increases, the contact locus varies less along the surface and appears to approach the contact locus of the flat plate shown in Figure 3.1(a).

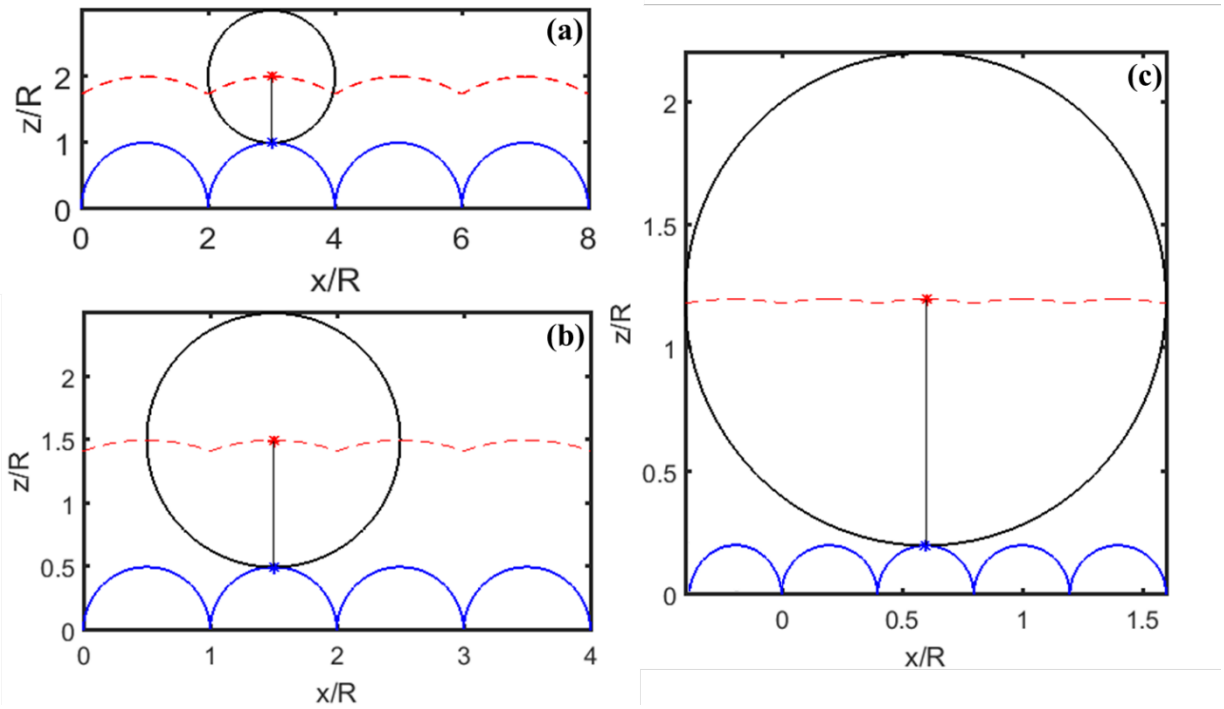

Figure 3.12 Contact locus plots of three surfaces comprised of several hemispherical asperities of radius $R_H^* = 1, 0.5$, and 0.2. The red dashed lines are the contact loci and the blue lines are the surfaces. The asperities are separated by a distance $L^* = 0$.

The corresponding d_c-distributions of these surfaces are shown in Figure 3.13. Each d_c-distribution exhibits a large peak followed by a long tail. The larger values of $|d_c^*|$ result when the sphere straddles two adjacent hemispherical peaks since the sphere is able to contact more of the underlying surface. While the contact locus appears to approach that of a flat plate in Figure 3.12(c), the same cannot be said of the resulting d_c-distribution. For $R_H^* = 0.2$, the corresponding flat plate would yield $|d_c^*| = 0.0825$ (with the top of the plate coinciding with the top of the

hemispheres), which is greater than the maximum value of $|d_c^*|$ obtained in the resulting d_c-distribution. This is due to the fact that the large sphere always interacts with less material compared to the flat plate, leading to smaller values of $|d_c^*|$, despite the close similarity of the two contact loci. (Note for the surfaces in Figure 3.12, the "missing material" between the hemispherical asperities, which of course is not included in the force profiles for these surfaces, is nonetheless included in the force profile for the corresponding flat plate.)

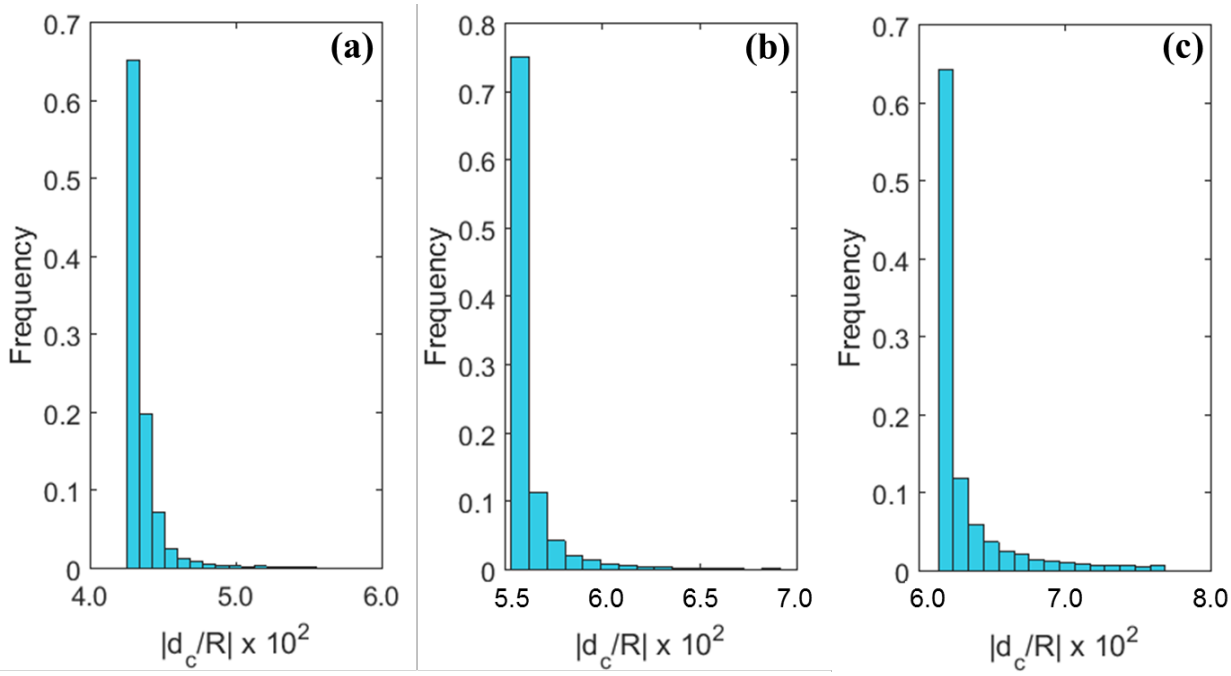

Figure 3.13 Corresponding d_c-distributions for the surfaces described in Figure 3.12.

A key result from analyzing the corresponding d_c-distributions for the various surface height function is that, in general, surface roughness can cause a significant variation in the vdW force and, in turn, the deflection at contact. The d_c-distribution appears to be a good signature of the roughness of a surface and is sensitive to even small-scale roughness on a surface. Hence, capturing the effect of surface roughness on the magnitude of the vdW force through incorporation

of surface topography directly into the approach-to-contact method should lead to a more accurate determination of the Hamaker constant of a material.

3.3 Vertical Force on a Sphere Approaching a Tilted Semi-Infinite Flat Plate

This section is concerned with an in-depth analysis of quantifying the vertical force on a sphere approaching a tilted semi-infinite flat plate. When the sphere is in contact with the sine wave at the point in which its curvature is zero ($x_s/R = 3.85$; $x_{contact}/R = \pi$), the surface behaves locally like a tilted flat plate. Here, an extension of eq 2.14 is derived in which a semi-infinite flat plate is tilted by an angle θ from the horizontal. Force profiles are then compared for a range of angles as well as between the tilted flat plate with $\theta = 45°$ and the analogous case of the sine wave in Figure 3.1(b) at $x_s/R = 3.85$ (black dashed curve).

Consider a sphere of radius R approaching a horizontal flat plate (with its top surface located at $z = 0$). As shown in Figure 3.14(a), the sphere center is at a vertical height z_s and the sphere touches the plate when its center is at the vertical height $z_{s,contact}$ (which in this case corresponds to $z_{s,contact} = R$). Let $\Delta z = z_s - z_{s,contact}$ represent the difference of these two heights, which for the case of the horizontal flat plate corresponds to the minimum separation distance (in the direction of the unit normal to the surface) between the surface of the plate and any point along the surface of the sphere. Hence, for the horizontal plate, the minimum separation distance between the surface and the center of the sphere is $r_{min} = \Delta z + R = z_s$ (see Figure 3.14(a)). Using $z_s = \Delta z + R$ (again for the horizontal plate), eq 2.14 can be rewritten as

$$F_{surf,plate} = -\frac{2}{3}\frac{A}{R}\frac{1}{[(1+\Delta z^*)^2 - 1]^2} \tag{3.3}$$

where $\Delta z^* = \Delta z/R$.

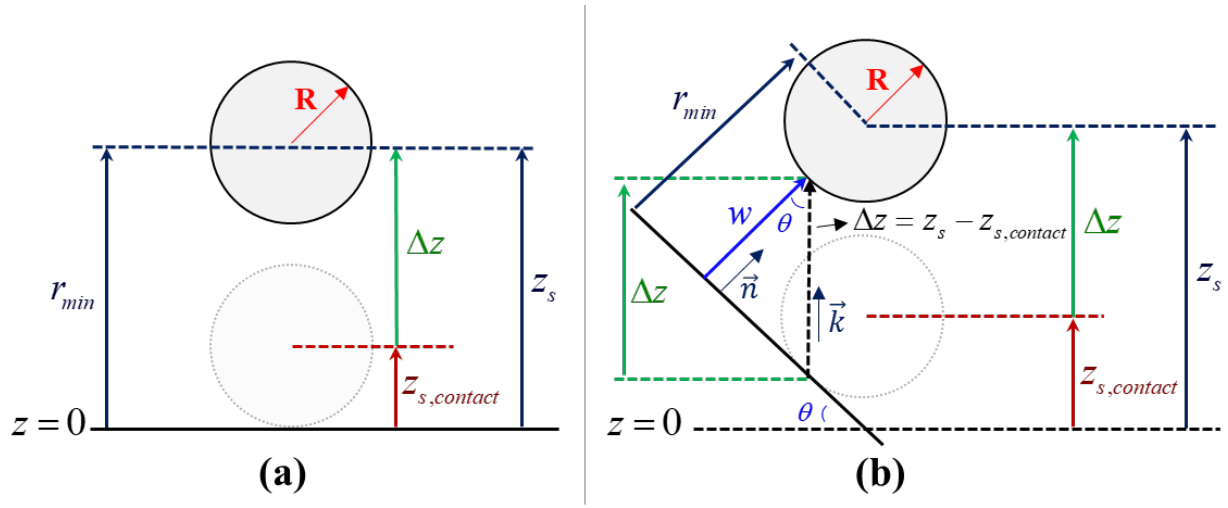

Figure 3.14 Schematic of a sphere with radius R approaching a semi-infinite flat plate. r_{min} is the minimum separation distance between the center of the sphere and the (upper) surface of the plate. Vertical locations, or the corresponding z-coordinates, are relative to a chosen $z = 0$ plane. z_s is the vertical location of the center of the sphere, $z_{s,contact}$ is the vertical location of the center of the sphere when the sphere is in contact with the surface, and $\Delta z = z_s - z_{s,contact}$. In (a), the plate is horizontal, in which the (upper) surface coincides with the $z = 0$ plane. Here, Δz also yields the minimum separation distance between the surface of the plate and any point along the surface of the sphere, i.e., $r_{min} = \Delta z + R$. In (b), the plate is tilted by an angle θ from the horizontal. Here, the minimum separation distance between the surface of the plate and any point along the surface of the sphere is $w = r_{min} - R$, in which $w = \Delta z \cos\theta$. $\vec{k}$ is the unit vector in the upward vertical direction and $\vec{n}$ is the unit normal vector to the tilted surface.

Now, consider a plate that is tilted by some angle θ from the horizontal, as shown in Figure 3.14(b). Here, $z_{s,contact} \neq R$ and the minimum separation distance between the tilted surface and the center of the sphere is not equal to $\Delta z + R$ (where again $\Delta z = z_s - z_{s,contact}$). Instead, $r_{min} = w + R$, where the distance w is defined in Figure 3.14(b) as the distance between the bottom of the sphere and surface, normal to the surface. However, if Δz in eq 3.3 is replaced by w, the force on the sphere due to the tilted plate is obtained in the direction of the (tilted) unit normal. The force in this direction is not, however, what is of final interest. To obtain the force in the z-direction, the force in the direction of the unit normal needs to be projected onto the vertical direction. From Figure 3.14(b), $\vec{n} \cdot \vec{k} = \cos\theta$ and $w = \Delta z \cos\theta$ (where $\vec{k}$ is the unit vector in the

upward vertical direction and $\vec{n}$ is the unit normal vector to the tilted surface). Therefore, the force on the sphere in the z-direction due to a tilted flat plate is given by

$$F_{surf,tilted\ plate} = -\frac{2}{3}\frac{A}{R}\frac{\cos\theta}{[(1+\Delta z^*\cos\theta)^2-1]^2} \tag{3.4}$$

The tilting of the plate gives rise to two competing effects on the resulting vertical force. The $\cos\theta$ in the numerator (which arises because of the projection of the normal force in the vertical direction) serves to reduce the vertical force as the plate is tilted. On the other hand, for a given relative vertical separation distance to contact, or Δz, the tilting of the plate serves to bring the sphere closer to the plate (i.e., $w = \Delta z\cos\theta$ decreases as the tilt angle increases for a given Δz). This latter effect should, however, be more dominant, as the denominator in eq 3.4 goes as $(\cos\theta)^2$ (to leading order). As a result, eq 3.4 suggests that the magnitude of the vertical force will increase (for a given Δz) as θ increase to 90°. (Note that θ cannot equal 90° in the analysis. In obtaining eq 3.4, the sphere is assumed to touch the surface at some point, which does not occur when the surface is completely vertical.) This predicted trend is what is observed in Figure 3.15, which plots the vertical force on the sphere versus Δz for several choices of θ. Figure 3.15 indicates that the tilting of the flat plate results in a net increase in the amount of material near the sphere as it approaches the plate. Hence, the vdW force, and ultimately the magnitude of the deflection at first contact, $|d_c^*|$, increases relative to that of a flat, horizontal plate.

Figure 3.15 also includes the force profile for a surface described by eq 3.1 with $\alpha/R = 1$ and $kR = 1$ (see Figure 3.1(b)) at $x_s/R = 3.85$, corresponding to $x_{contact}/R = \pi$ (for this analysis $A = 101$zJ and $R = 0.1$nm). At this contact location, the curvature of the surface is zero with a slope = 1. Interestingly, the force profile as the sphere comes into contact with this location is nearly identical to that of a tilted flat plate with $\theta = 45°$ (i.e., slope = 1). Hence, at this location,

the sine wave behaves like a tilted flat plate. This result indicates that the vdW force is dominated by the interactions between those portions of the two bodies that are only very close to one another.

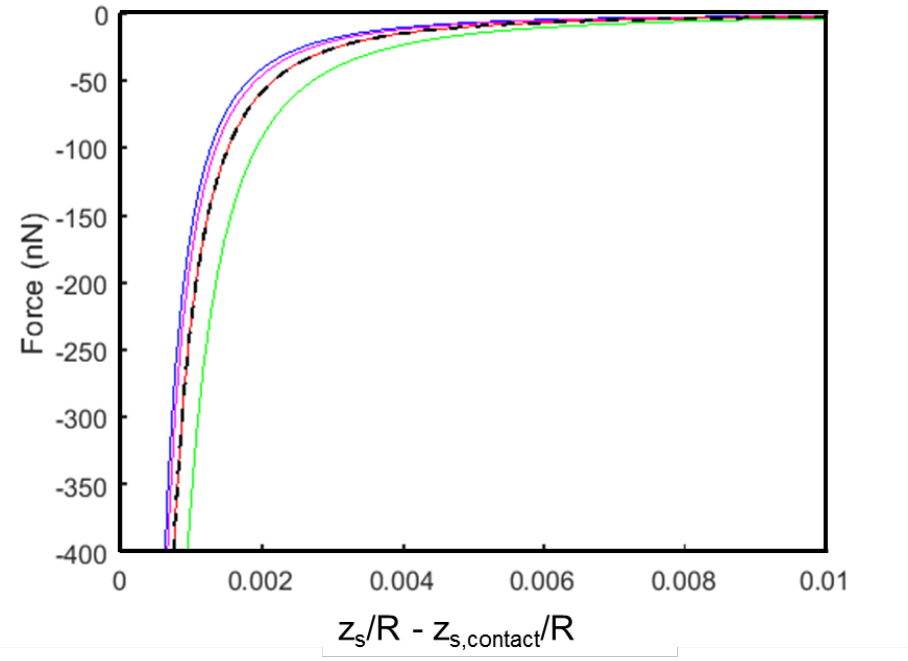

Figure 3.15 Force profiles corresponding to the interaction of a sphere with a flat plate (blue curve) and tilted plates with $\theta = 6^o$ (magenta curve), 45^o (red curve), and 63^o (green curve), and the sine wave in Figure 3.1(b) at $x_s/R = 3.85$ (black dashed curve). For this analysis, $A = 101$zJ and $R = 0.1$nm.

3.4 Comparison of Force Trajectories Between the New vdW Force Model and the Rabinovich *et al.* Surface Roughness Model

The Rabinovich *et al.*[95] model is an extension of the classical Rumpf model, which is used to predict the force of adhesion between a particle of radius R and a surface with nanoscale surface roughness. The model, for which a schematic is provided in Figure 3.16, considers two roughness scales, where λ_1 and λ_2 are the wavelengths of the two roughness scales, and r_1 and r_2 are the radii of the asperities from which the roughness on the surface is composed. An assumption of the

model is that the sphere may only make contact with the surface at the top of an asperity (for more details, see ref 95).

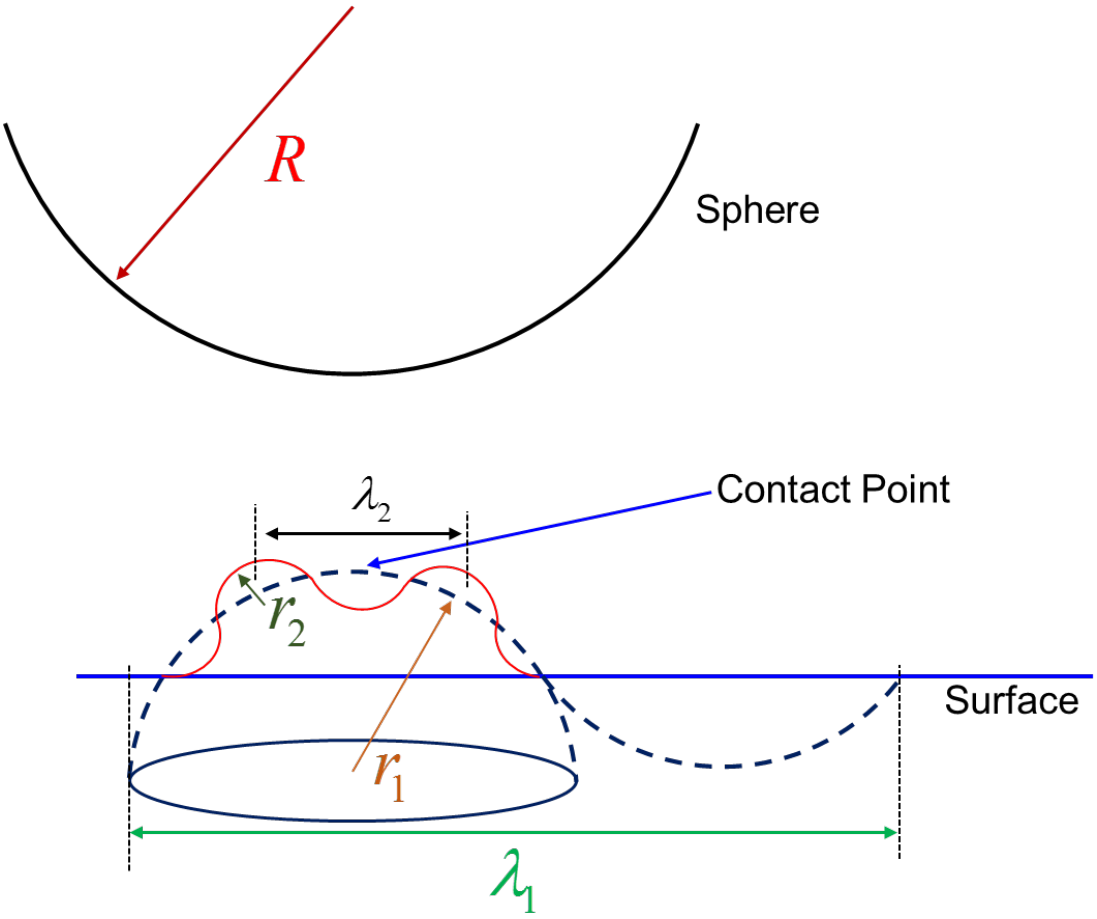

Figure 3.16 Schematic of the Rabinovich *et al.* roughness model. R is the radius of the sphere, λ_1 and λ_2 are the wavelengths of the two roughness scales, and r_1 and r_2 are the radii of the asperities from which the roughness on the surface is composed. The model requires that the sphere makes contact with the surface at the top of the asperity. This figure is adapted from Laitinen *et al.*[95]

The surface model shown in Figure 3.7 forms the basis of some previous attempts to quantify, albeit implicitly, the effect of surface roughness on the magnitude of the vdW force. (Figure 3.16 can be made similar to Figure 3.7 for $r_2 = 0$ and $\lambda_2 = 0$.) Therefore, the (explicit, or newly derived vdW force expression) analysis of this same model surface to test the effectiveness of these (implicit) approaches in accounting for surface roughness can be utilized. (Other approaches have

also been developed to describe, with varying degrees of precision, the underlying geometry or roughness of a given surface.[34,88,94,95,97,98])

Rabinovich *et al.*[95] obtained an expression for the vdW force between a sphere of radius R and the surface in Figure 3.7, although the effect of the surface geometry was only included in an average sense. In other words, the resulting force expression only depended upon the relative separation of the very bottom of the sphere and the underlying flat plate (and not on the actual location of the sphere center along the surface), with the impact of the hemispheres only included in a correction term. For this surface, and making use of our notation and coordinate system, their vdW force expression is given by

$$F_{Rab} = -\frac{2}{3}\frac{A}{R((z_s^*)^2-1)^2}\left[\frac{1}{1+\left(\frac{58\,(rms^*)}{(2R_H^*+L^*)^2}\right)}+\frac{(z_s^*-1)^2}{(1+1.82(rms^*))^2}\right] \tag{3.5}$$

where $rms^* = rms/R$ is the root-mean-squared (rms) height of the semi-hemispherical caps. The form of eq 3.5 is simply the vdW force between a sphere and flat plate modified with a correction term that is based on the rms roughness of the surface. In ref 95, the sphere-plate force expression in eq 1.6 was instead used. Here, for a proper comparison to our previous results, the force expression is modified to include the rigorous sphere-plate relation in eq 2.14, along with considering half-cylinders (*i.e.*, two-dimensional surfaces) instead of the hemispheres (*i.e.*, fully three-dimensional surfaces) considered in ref 95.

Since the Rabinovich *et al.* approach implicitly accounts for surface roughness, the vdW force is not dependent upon the sphere location, or x_s, and as such will only yield a single value of d_c for a given A (*i.e.*, this model cannot predict a d_c-distribution). (This deflection at first contact must be based on the additional unphysical assumption that the sphere touches the underlying flat plate, regardless of the positions of the hemispheres.) Nonetheless, the resulting

vdW force profile may still be satisfactory in an average sense. To test the adequacy of the Rabinovich *et al.* model in this regard, the single force profile obtained using eq 3.5 is compared to the average force profile obtained by solving eq 2.14 for several values of x_s. The resulting force profiles for the surfaces in Figure 3.7 are shown in Figure 3.17 for which (a) $R_H^* = 2$, (b) $R_H^* = 1$, and (c) $R_H^* = 0.2$, and $L^* = 0$ in all cases. To appropriately compare the force profiles along different portions of the surface, the forces are plotted versus the relative separation distance, $z_s^* - z_{s,contact}^*$, where $z_{s,contact}^* = 1$ for eq 3.5 regardless of the (horizontal) location of the sphere. The maximum and minimum force profiles obtained with eq 2.14 for a given surface are also included.

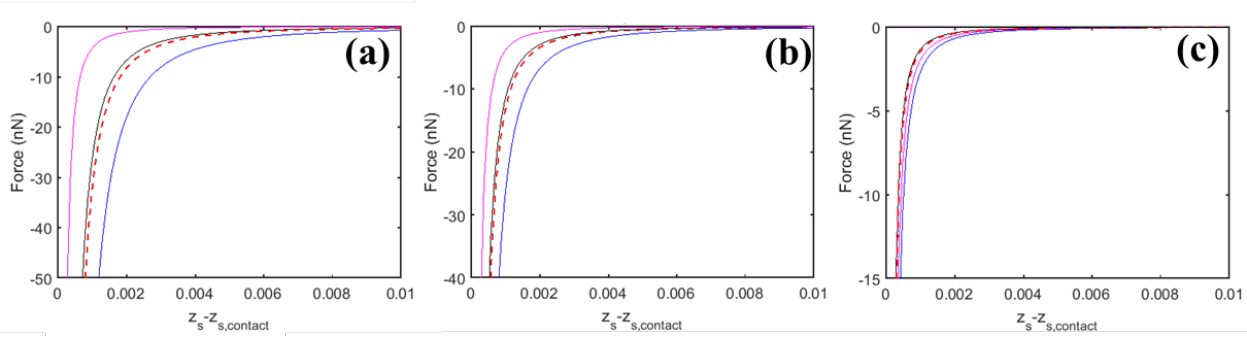

Figure 3.17 A comparison of the force profiles obtained by solving the modified Rabinovich *et al.* model (magenta lines) and eq 2.14. The blue and black lines are the maximum and minimum force profiles, respectively, along the surface and the red dashed line is the average force trajectory over one period of the surface (all from eq 2.14). The surfaces are described by Figure 3.7, and (a) $R_H^* = 2$, (b) $R_H^* = 1$, and (c) R_H^* =0.2 while $L^* = 0$ in all cases.

An assumption of the Rabinovich *et al.* model is that the radius of the approaching sphere is much greater than the scale of the surface roughness (*i.e.* $R \gg R_H$). Hence, in Figure 3.17(c), for which $R = 5R_H$, the Rabinovich *et al.* force profile is reasonably close to the average force profile from eq 2.14 across one period of the surface. The Rabinovich *et al.* force profile slightly underestimates the true average force, while also residing in between the maximum and minima

force profiles (although the true average force profile is quite close to the minimum force profile). The agreement between the Rabinovich *et al*. model and eq 2.14 improves as $R_H^* \to 0$. But, as may be expected, the Rabinovich *et al*. model yields worse predictions when the sphere radius becomes comparable to the radius of a hemisphere. As seen in Figure 3.17(a) and Figure 3.17(b), the Rabinovich *et al.* force profile now resides outside of the bounds set by the maximum and minimum force profiles from eq 2.14, and as a result is not in good agreement with the actual average force profile.

This discrepancy between the average force profile and eq 3.5 persists even as $R_H^* << 1$, or as the relative length scale of the roughness becomes negligible. Even as the approaching sphere becomes much larger than the size of an asperity, the force between the sphere and this surface does not become identical to that between the sphere and a flat plate. The "missing material" between the hemispherical asperities, which is not included in eq 2.14, is nonetheless included in the flat plate force relation appearing in eq 3.5. Overall, Figure 3.17 indicates that surface roughness must be properly accounted for if an accurate value of A is to be determined from either the obtained force profiles or distribution of d_c-values.

3.5 Analysis of the Effect of Surface Topography on the Resulting d_c-Distributions for Surface Height Functions of the Form $h(x, y)$

For surface height functions that vary in both the x- and y-directions, the MDM can be applied to generate a "contact mesh", or a plot of the position of the center of the sphere when in contact with the surface as a function of x_s and y_s. In this case, a 50 by 50 grid comprising a complete period of the surface height function was selected, for a total of 2500 contact points.

Two "egg-crate" surfaces, F and G, shown in Figure 3.18, were generated using the surface height function of[103]

$$h(x,y) = \alpha[\cos(kx) + \cos(ky)] \tag{3.6}$$

where $k = 2\pi/\lambda$ is the wavenumber (and λ is the wavelength). For surface F, $\alpha/R = 0.5$ and $kR = 1$ (or $\lambda/R = 2\pi$). Thus, for a given horizontal location of the sphere, or each (x_s, y_s) pair, $x_{contact} \neq x_s$ and $y_{contact} \neq y_s$, except at the top of each hill and at the bottom of each valley (where $x_{contact} = x_s$ and $y_{contact} = y_s$). Furthermore, the sphere is able to contact all parts of this surface (and, in particular, the sphere can touch the bottom of a valley). The "contact surface" obtained from the minimum distance method, or $z_{s,contact}$ for each (x_s, y_s) pair, is also provided in Figure 3.18, which for F is differentiable at all points. For surface G, $\alpha/R = 1.5$ and $kR = 1$. In this case, the sphere can no longer contact sections of the surface centered around the bottom of a valley. Consequently, the contact surface for G is no longer differentiable at those points directly above the bottom of a valley. The third surface, H, shown in Figure 3.19, was generated from[103]

$$h(x,y) = \alpha[\cos(kx) + \cos(ky)] + \beta[\cos(cx) + \cos(cy)] \tag{3.7}$$

where $\alpha/R = 0.5$, $kR = 1$ (as for surface F), $\beta/R = 0.0625$, and $cR = 10$. This surface superimposes a smaller-scale surface roughness onto surface F. As a result, the sphere can contact only a small fraction of the surface (mainly around the peaks of the many small hills), which gives rise to many points of non-differentiability in the corresponding contact surface. The quasi-static d_c-distributions for each surface are provided in Figure 3.20 (surfaces F and G) and Figure 3.21 (surface H), again for A = 100 zJ, R = 1000 nm, and k_c = 0.1 N/m.[103]

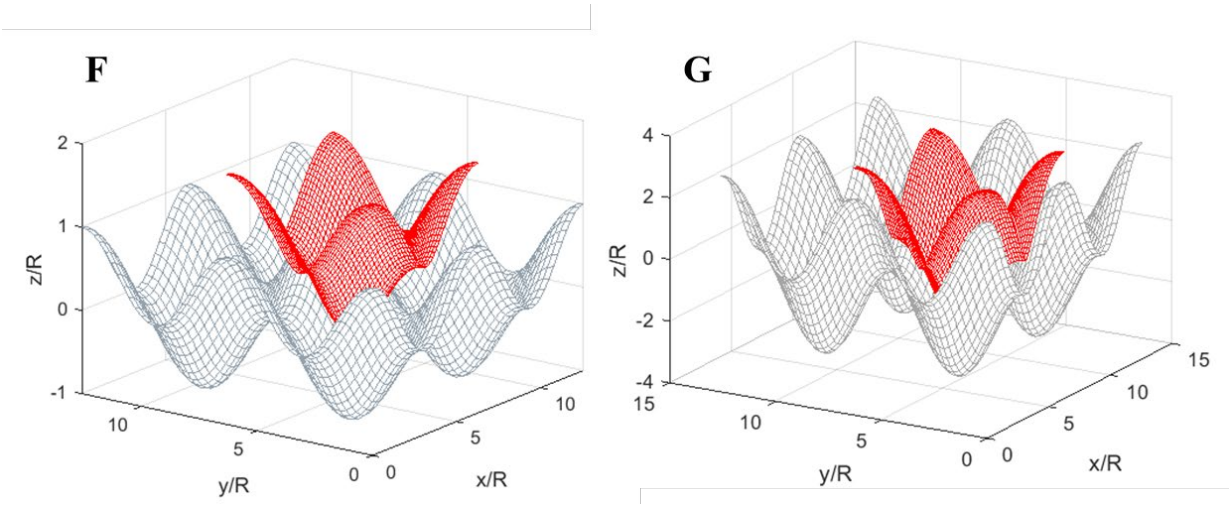

Figure 3.18 Plots of the two surfaces (gray mesh) described by the surface height function in eq 3.6, along with portions of their corresponding contact surfaces (red mesh). For each surface, $kR = 1$ or $\lambda/R = 2\pi$, while $\alpha/R = 0.5$ and 1.5 for surfaces F and G, respectively. Because the sphere cannot touch the bottom of the valleys in surface G, discontinuities in its contact mesh arise at these locations.[103]

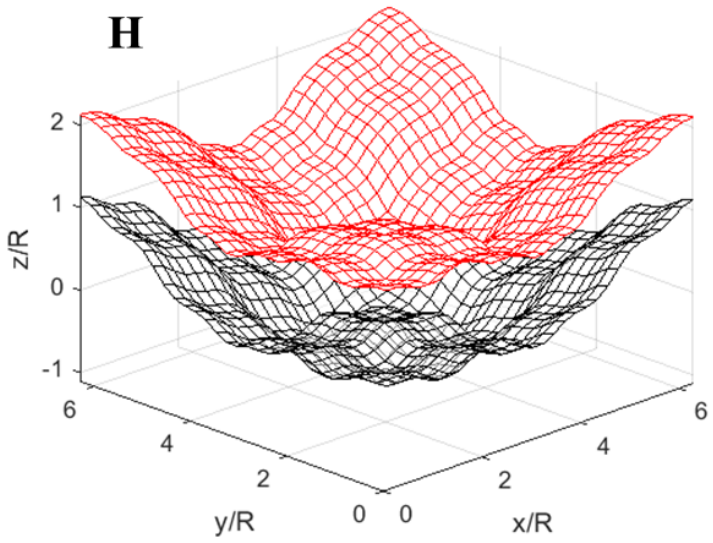

Figure 3.19 Plot of the surface (gray mesh) described by the surface height function in eq 3.7, along with the corresponding contact surface (red mesh). For surface H, $\alpha/R = 0.5$, $kR = 1$, $\beta/R = 0.0625$, and $cR = 10$, which introduces a superimposed small-scale surface roughness onto surface A.[103]

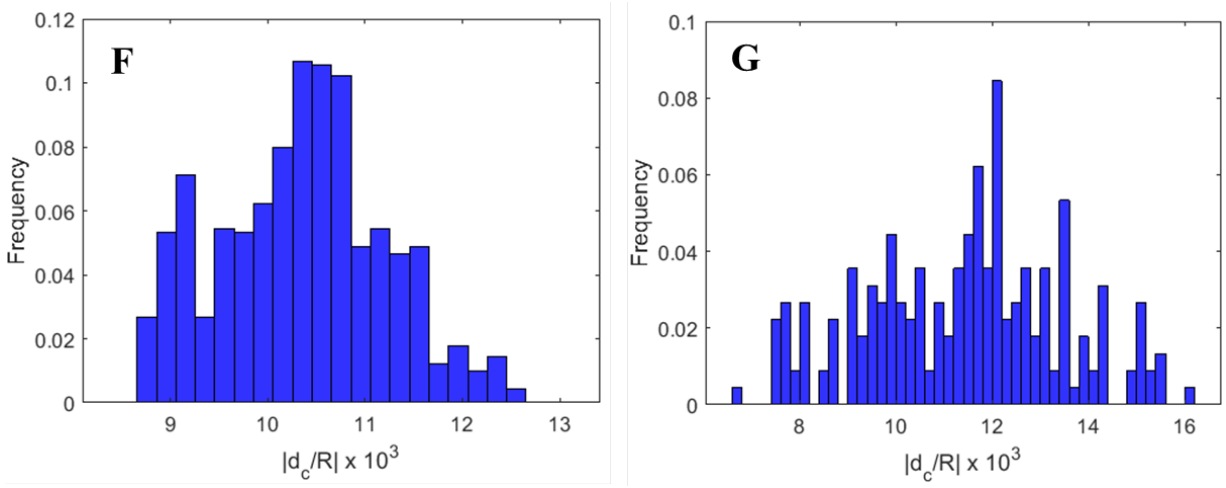

Figure 3.20 The quasi-static d_c-distributions for surfaces F and G in Figure 3.18. Here, A = 100 zJ, R = 1000 nm, and k_c= 0.1 N/m.[103]

The quasi-static d_c-distribution for surface F is centered around d_c~10.5 nm, with a range of 8.8 – 12.6 nm and an average value of 10.6 nm; it is somewhat symmetrical, though skewed slightly towards larger values of d_c. The larger values of d_c correspond in general to those surface locations where the vdW attractive force is greater, or when the sphere at close separation distances interacts with more nearby material on the substrate. Hence, the largest values of d_c are obtained when the sphere approaches surface F near any of the valleys, since here the surface curves upwards toward the sphere. On the other hand, the smallest values of d_c are obtained when the sphere approaches surface A around any of the peaks, since here the surface curves away from the sphere. Besides these variations in the vdW force along the surface, surface geometry also affects the shape of the d_c-distribution. As discussed in ref 101, the uniform sampling of the horizontal location of the sphere, or of x_s and y_s, may nonetheless generate a nonuniform sampling of points along the surface.

Although the topography on surface G has the same wavelength as surface F, it has an amplitude that is three times larger. As a result, the shape of the quasi-static d_c-distribution for G

is very different from F. The d_c-distribution for G, with an average value of 11.6 nm, is now much broader (7 –16 nm). The higher negative curvature around the peaks of this surface results in less substrate material available to interact with the sphere (yielding smaller d_c-values), while the larger positive curvature around the valleys results in more material available to interact with the sphere (yielding larger d_c-values). Furthermore, since there are portions of surface G that cannot be directly contacted by the sphere, the resulting deflections around these locations cannot be as large as would be expected from the corresponding magnitudes of the vdW forces, thereby giving rise to a "less smooth" distribution.

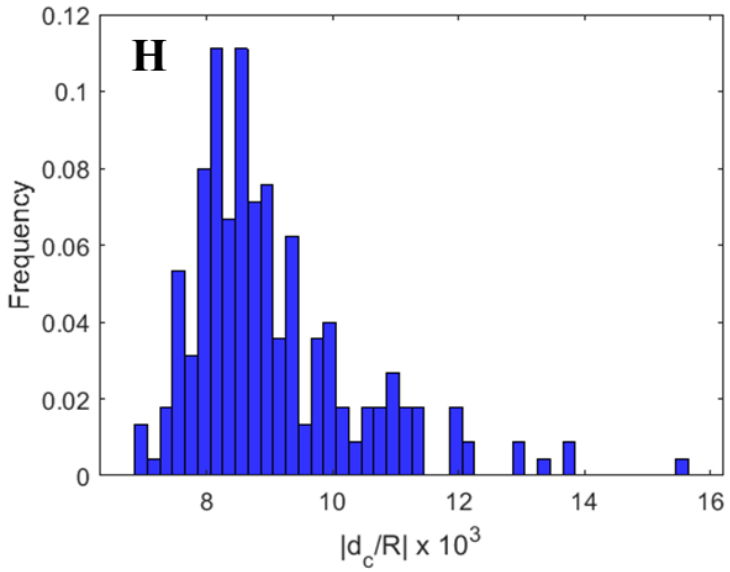

Figure 3.21 The quasi-static d_c-distribution for surface H in Figure 3.19. Here, A = 100 zJ, R = 1000 nm, and k_c= 0.1 N/m.[103]

The quasi-static d_c-distribution for surface H is shifted to smaller deflections, as compared to F, having an average of 9.25 nm, though the range is still relatively broad (7-15.8 nm). Nonetheless, most deflections are found between 7.5 and 10 nm, which abruptly ends at the smallest deflections but has a rather long tail for the higher deflections. Because of the small-scale

roughness present in H, the amount of substrate material available for the sphere to interact with decreases across the entire surface, and so the deflections are shifted in general to lower values. Nevertheless, the maximum deflection for this surface occurs at 15.8 nm, which is not much different from surface F. While the sphere is mainly only interacting with the peaks of the small-scale roughness (β/R = 0.0625), the underlying larger-scale roughness of the surface (α/R = 0.5) tends in some areas to move more material upwards to the sphere. Hence, for some sphere locations, the vdW force is still relatively large.

3.6 Summary

This chapter provided an analysis of the effects of surface geometry on the resulting d_c-distributions, in the quasi-static limit, for several surface height functions of the form $h(x)$ and $h(x, y)$. Contact loci and contact mesh plots were obtained illustrating the position of the sphere when in contact with the surface. The presence of small-scale roughness serves to vary the amount of substrate material that is close to sphere and therefore influences the magnitude of the vdW force and ultimately d_c. This chapter sets the stage for later chapters as model-predicted d_c-distributions will be obtained for real AFM surface scans and subsequently compared with those obtained experimentally. The sensitivity of the d_c-distributions to the various scales of roughness described by the surface height functions is an important result since accurate model-predicted d_c-distributions are essential to obtaining Hamaker constants with a reduction in uncertainty. The next chapter is concerned with the validation of the quasi-static model for a range of cantilever approach speeds and introduces the concept of relative entropy which is a quantitative metric for comparing the "closeness" of two d_c-distributions.

4. DYNAMIC ANALYSIS OF CANTILEVER TIP BEHAVIOR AND VALIDATION OF THE QUASI-STATIC MODEL

4.1 Introduction

The d_c-distributions previously obtained in Chapter 3 follow from the limit of quasi-static behavior of the cantilever, in which the cantilever is assumed to always be in mechanical equilibrium up until the critical point (at which in the quasi-static limit the tip then immediately "jumps" into contact with the surface). In practice, however, the cantilever approaches the surface at a finite approach speed, such that mechanical equilibrium cannot truly be maintained (due to inertial effects). Consequently, a model describing the dynamic behavior of the cantilever tip as it approaches and interacts with an arbitrary surface is presented. From a quantitative comparison of the d_c-distributions generated with both the quasi-static and dynamic models, a specific threshold cantilever approach speed is determined, in which the difference between these two distributions becomes unimportant. By selecting approach speeds below this threshold value, subsequent experimentally-obtained d_c-distributions can therefore be confidently compared to the corresponding quasi-static d_c-distribution. Hence, the proposed method for estimating A requires only the determination of the quasi-static d_c-distribution for a particular surface, thereby avoiding the additional computational expense of generating the dynamic d_c-distributions.

4.2 Dynamic Behavior of the AFM Cantilever Tip Modeled as an Effective Sphere

The quasi-static description of the behavior of the AFM cantilever cannot be strictly valid. Since the substrate moves at a finite speed toward the cantilever during an AFM force experiment,[79,80] or equivalently the platform moves at a finite speed toward the (stationary) surface, the inertial behavior of the tip may become important. If so, the effect of the inertia of the tip is expected to

be greatest at those separation distances around the critical point, where the tip moves very rapidly just before it first contacts the surface.

To study the importance of these inertial effects, and their possible impact on the obtained values of d_c, the dynamic behavior of the cantilever tip (again described as an effective sphere) can be modeled as follows[79,80]

$$m\frac{d^2z_s}{dt^2} = F_{surf} + F_{spr} \tag{4.1}$$

where t is time and $m = k_c/4\pi^2\nu_0^2$ is the effective mass of the sphere, in which ν_0 is the resonance frequency of the cantilever. F_{surf} is again given by eq 2.9, while $F_{spr} = -k_c d = -k_c\left(z_s - z_p + R\right)$ (see Figure 4.1). The cantilever, or platform, approaches the (stationary) surface with a constant speed, v_c (chosen to be a positive quantity). Thus, z_p varies with time as $z_p = z_{p,0} - v_c t$, where $z_{p,0}$ is the initial position of the platform above the surface. Upon nondimensionalizing the spatial quantities by R, eq 4.1 can be written as[103]

$$\frac{d^2z_s^*}{dt^{*2}} = -\frac{4}{3\pi}b^*\int_{-\infty}^{\infty}\int_{-\infty}^{\infty}\frac{dx^*dy^*}{\left[(x^*-x_s^*)^2+(y^*-y_s^*)^2+\left(h^*-z_{s,crit}^*\right)^2-1\right]^3} - z_{s,crit}^* - a^*t^* + z_{p,0}^* - 1 \tag{4.2}$$

where $t^* = 2\pi\nu_0 t$, $a^* = \frac{1}{2\pi R}\frac{v_c}{\nu_0}$ (which is related to the ratio of the two characteristic timescales $1/\nu_0$ and R/v_c), and $b^* = \frac{A}{k_c R^2}$ (which is related to the ratio of two characteristic energies).

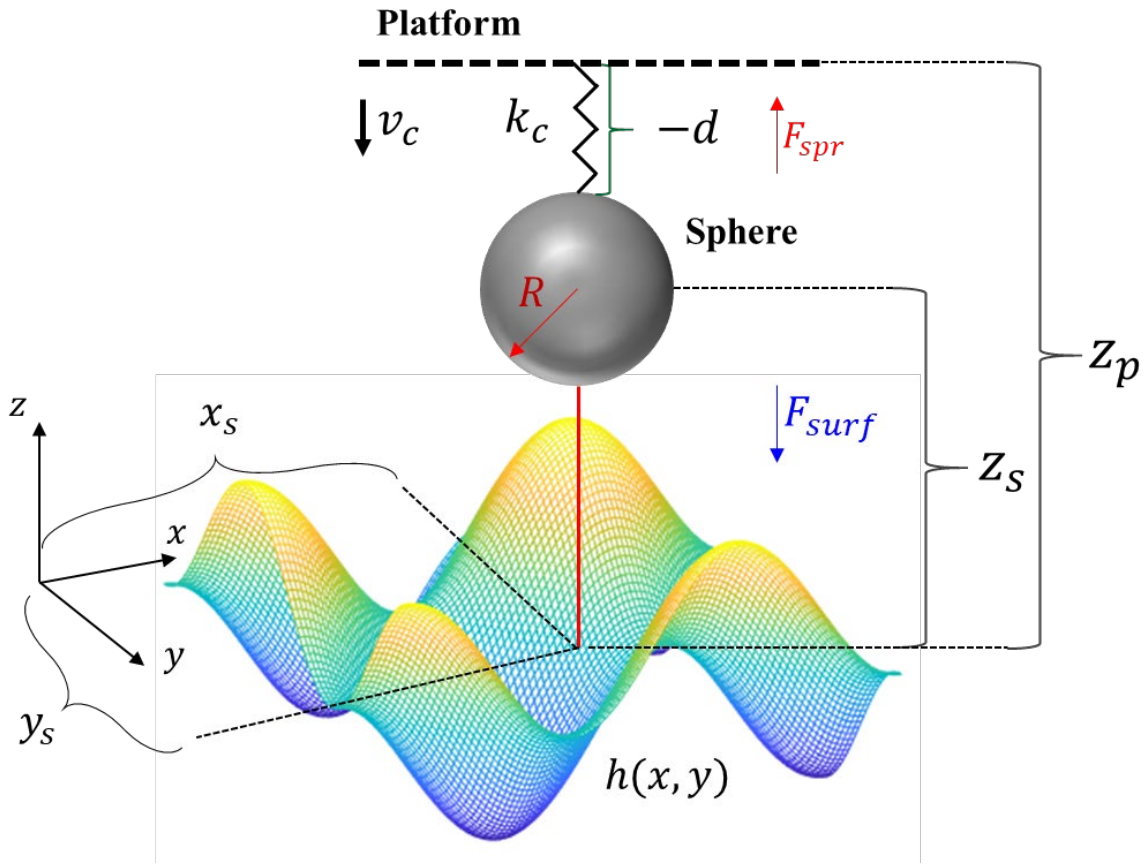

Figure 4.1 Schematic of an AFM cantilever tip modeled as a sphere attached to a horizontal platform by a Hookean spring, in which the sphere also interacts with an arbitrary surface described by the surface height function $h(x,y)$. k_c is the spring constant of the cantilever, v_c is the cantilever (platform) speed, z_s and z_p are the vertical locations of the sphere and platform, respectively, from $z = 0$, R is the radius of the sphere, and d is the deflection of the spring.

Eq 4.2 is an ordinary differential equation requiring two initial conditions to solve, one for the initial position of the sphere and one for its initial speed. The cantilever is assumed to begin sufficiently far from the surface that the tip is both in mechanical equilibrium and initially traveling with the same downward speed as the platform at $t = 0$. For the chosen initial platform location $z_{p,0}$, and for the chosen horizontal location of the sphere (x_s and y_s), the quasi-static relation in eq 2.16 is solved to determine $z_{s,0}$, the initial vertical location of the sphere. Furthermore, with the vertical component of the sphere's speed given by $v_s = dz_s/dt$, the sphere is chosen to be moving with $v_s = -v_c$ at $t = 0$. For a given set of physical parameters (or the approach speed, spring

constant, resonance frequency, and horizontal sphere location), eq 4.2 is integrated forward in time until the sphere initially contacts the surface, or when $z_s = z_{s,contact}$. Due to inertial effects (*i.e.* the term on the left-hand side of eq 4.2), no critical point arises within the dynamic model. The deflection of the cantilever tip at first contact is, however, still well-defined and determined by $d_c = z_{s,contact} - z_{p,contact} + R$, where $z_{p,contact}$ is the corresponding location of the platform when $z_s = z_{s,contact}$.

4.3 Verifying the Quasi-Static Assumption for Model Surfaces

As a reference case, eq 4.2 was initially solved for an infinitely flat plate, or $h^* = 0$. The resulting ratio of d_c to its value in the quasi-state limit, $d_{c,qs}$, for the flat plate is shown in Figure 4.2 for different cantilever approach speeds with $R = 1000$ nm, $k_c = 0.1$ N/m, and $A = 100$ zJ (which yields $d_{c,qs} = 10.35$ nm). As expected, this ratio approaches unity as v_c decreases. But d_c for a given v_c is always smaller than what it is in the quasi-static limit, while d_c also decreases with an increase in v_c. These two trends arise because of the following reasons. First, the speed of the tip, however large it may become just before the tip contacts the surface, remains finite (in contrast to the tip immediately jumping to the surface upon reaching the critical point in the quasi-static model). Second, the platform is in constant motion (in contrast to the fixed location of the platform once the critical point is reached in the quasi-static model). Hence, d_c for the dynamic model is less than $d_{c,qs}$. Furthermore, the relative speed between the tip and platform just before contact decreases with an increase in v_c, which results in a decrease in d_c as the cantilever approach speed increases. Nevertheless, even at the relatively fast approach speed of 1000 nm/s, d_c is still within 0.5% of its quasi-static value.

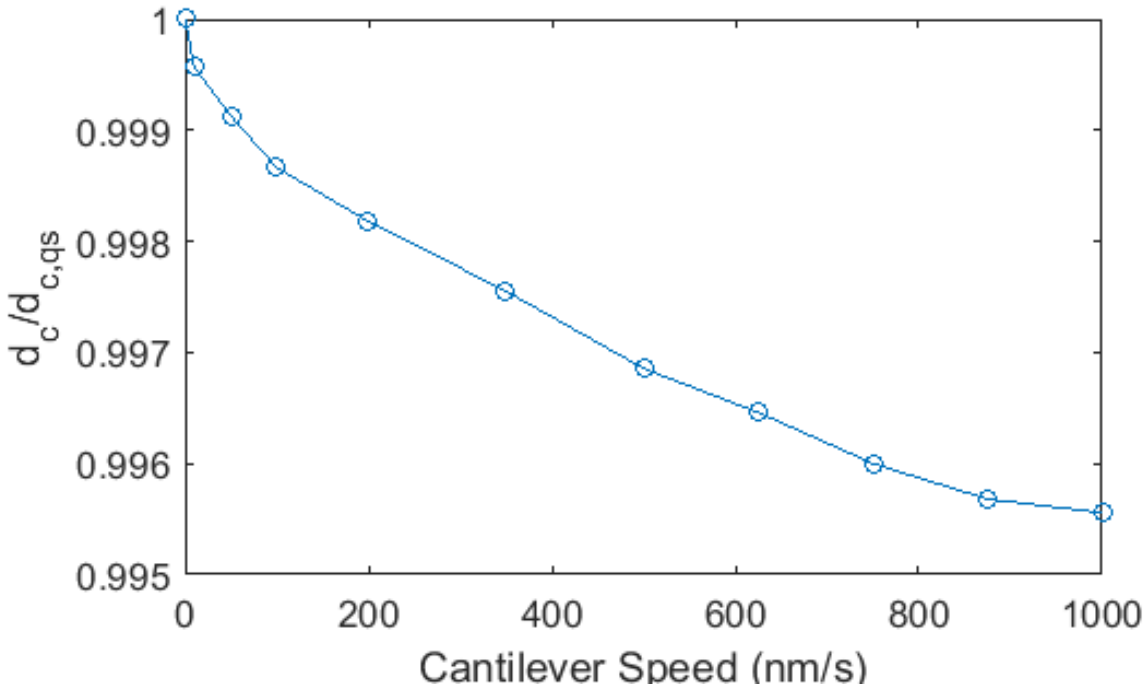

Figure 4.2 The ratio of the deflection at first contact, d_c, to the deflection at first contact in the quasi-static limit, $d_{c,qs}$, or $d_c/d_{c,qs}$, versus the cantilever approach speed for a surface that is an infinite flat plate. Here, $R = 1000$ nm, $k_c = 0.1$ N/m, and $A = 100$ zJ.

Figure 4.2 reaffirms the previous conclusion obtained for the flat plate (though using the rigorous force expression for $h = 0$, or eq 2.14) that at sufficiently slow approach speeds (which includes the "standard" AFM default approach speed of 200 nm/s) the predictions of the quasi-static model will be negligibly different from the results of the dynamic model (*i.e.* these differences are much smaller than the experimental noise encountered in typical AFM experiments). Thus, for the tip approaching a flat plate, the computationally less intensive quasi-static model, which requires only the simultaneous solution of eq 2.16, can be used instead of the dynamic model, in which eq 4.2 is integrated in time until the sphere first contacts the surface.

While inertial effects are unimportant when the tip approaches a flat plate at standard speeds, a similar conclusion may not hold, however, for more complicated surfaces, and for which there is a distribution of d_c-values. Hence, in order to test the validity of the quasi-static model

for the case of the tip approaching a substrate with non-zero surface roughness, quasi-static and dynamic d_c-distributions for the three model surfaces F, G and H shown in Figure 3.18 and Figure 3.19 are compared.

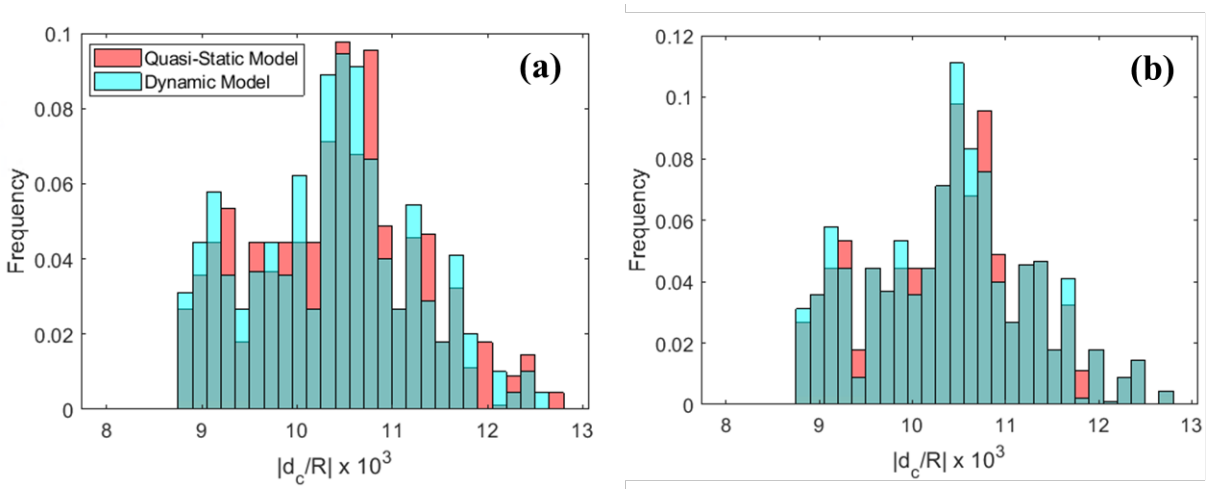

Figure 4.3 Comparison of the quasi-static (light blue) and dynamic (red) model-predicted d_c-distributions for surface F (shown in Figure 3.18) at the cantilever approach speeds of (a) 1000 nm/s and (b) 200 nm/s.

For surface F, the resulting d_c-distributions for the two approach speeds of 200 nm/s and 1000 nm/s are provided in Figure 4.3, which also compares them to the corresponding quasi-static distribution. At v_c = 200 nm/s, the dynamic distribution is nearly identical to the quasi-static distribution, a result consistent with what was seen for the flat plate in which the behavior of the cantilever is essentially quasi-static at this approach speed. As v_c increases to 1000 nm/s, the dynamic d_c-distribution shifts to the left (*i.e.* relative to the quasi-static distribution there is an increase in the frequencies of smaller d_c-values along with a decrease in the frequencies of the larger d_c-values), though not significantly. Similar to the flat plate, inertial effects cause the dynamic deflections at contact to always be smaller than the quasi-static result at any location along the surface, with the dynamic values of d_c again decreasing with an increase in the approach

speed. Yet also like the flat plate, inertial effects only have a small impact on the resulting deflections (at least for the approach speeds considered). Compared to Figure 4.3, Figure 4.4 and Figure 4.5, corresponding to surface G and H, respectively, show similar trends where the two distributions are nearly identical at v_c = 200 nm/s and the dynamic d_c-distributions shift more to the left as v_c increases.

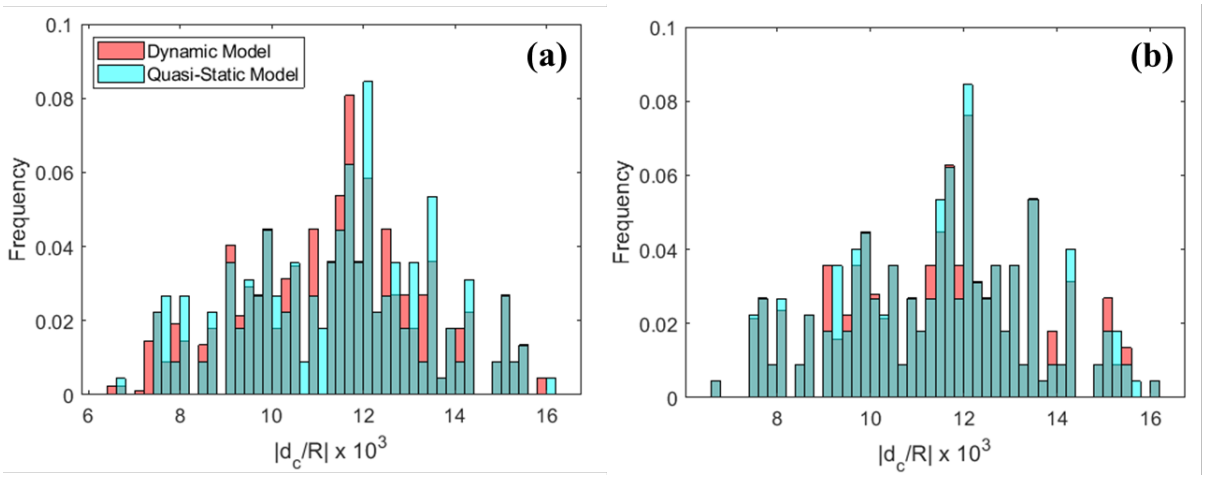

Figure 4.4 Comparison of the quasi-static (blue) and dynamic (red) model-predicted d_c -distributions for surface G (shown in Figure 3.18) for the cantilever approach speeds of (a) 1000 nm/s and (b) 200 nm/s.

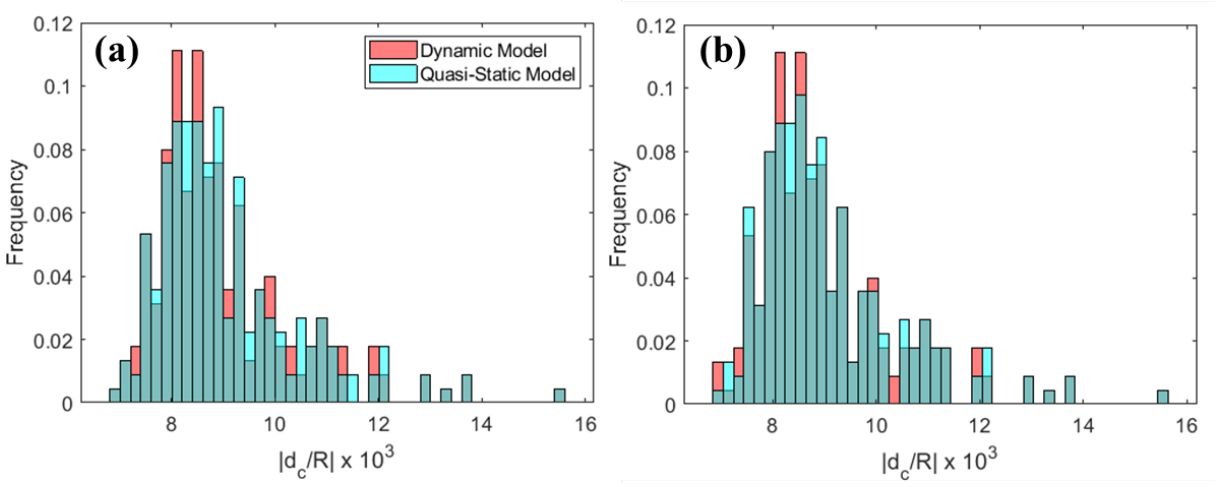

Figure 4.5 Comparison of the quasi-static (blue) and dynamic (red) model-predicted d_c -distributions for surface H (shown in Figure 3.19) for the cantilever approach speeds of (a) 1000 nm/s and (b) 200 nm/s.

In order to quantitatively determine the "closeness" of the dynamic and quasi-static distributions, their relative entropy or value of the Kullback-Leibler (KL) divergence[104–106] was computed, which for two discrete probability density distributions is defined as follows

$$D_{KL}(p\|q) = \sum_{i=1}^{N} p(x_i) \cdot ln\left(\frac{p(x_i)}{q(x_i)}\right) \tag{4.3}$$

where $p(x_i)$ is the probability density of the chosen "true" distribution, $q(x_i)$ is the probability density of the "approximating" distribution, and $x_1, \ldots, x_N$ represent the various histogram bins assigned to the "true" distribution (and for which $p(x_i) \neq 0$). The relative entropy is finite and non-zero only when for the same x_i both $p(x_i) \neq 0$ and $q(x_i) \neq 0$. (The contribution for a given x_i is considered to be zero when $p(x_i) = 0$.) The relative entropy equals zero when the two distributions are identical, while a non-zero value provides a measure of how much "information is lost" between these two distributions.[107]

For further analyzing the trends seen in Figure 4.4 and Figure 4.5, the quasi-static d_c-distribution was chosen as the "true" distribution, while the "approximating" distribution was chosen to be the dynamic d_c-distribution. The resulting relative entropy versus v_c is shown in Figure 4.6 for each surface (F, G and H), which also includes for comparison $1 - d_c/d_{c,qs}$ versus v_c for the flat plate.

As expected for each surface, the dynamic distribution becomes identical to the corresponding quasi-static distribution in the limit of very low approach speeds (*i.e.*, the relative entropy goes to zero as v_c goes to zero). The relative entropy for all surfaces is also seen to increase as the approach speed increases, indicating that the dynamic distribution is becoming "less like" the quasi-static distribution, or inertial effects are becoming more important, as v_c increases. Although the dependence of the relative entropy on v_c for each surface is quite different, Figure

4.5 nevertheless validates the use of the relative entropy as an appropriate measure of the difference between the dynamic and quasi-static distributions. (Since the various histograms are not continuous and are generated using finite bin widths, the resulting plots of the relative entropy will not necessarily be "smooth".)

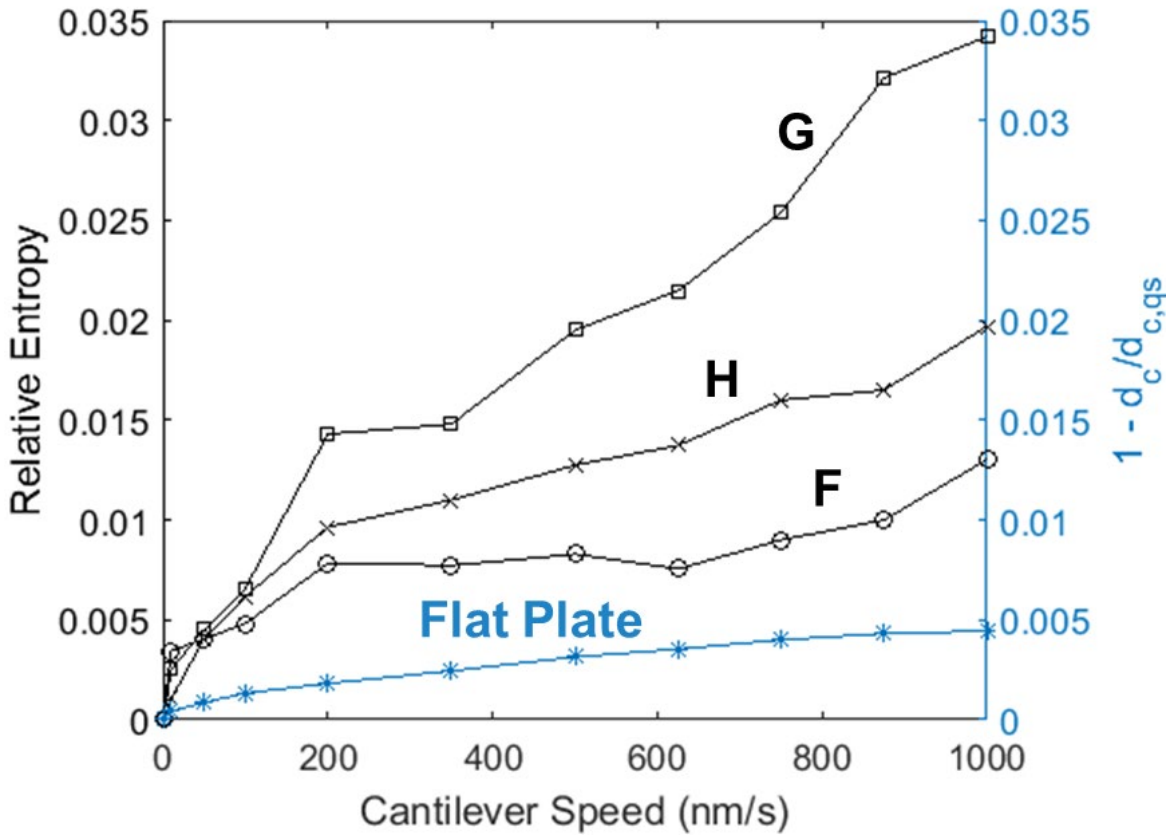

Figure 4.6 Relative entropy versus cantilever approach speed for surfaces F, G, and H (left y-axis). For comparison, $1 - d_c/d_{c,qs}$ versus v_c from Figure 4.2 for the flat plate is included (right y-axis).

The relative entropy can also be used to provide a more quantitatively meaningful analysis of the importance of inertial effects, which Figure 4.6 arguably only yields in a relative sense. In particular, the relative entropy is utilized to assign an effective Hamaker constant, A_{eff}, to a given dynamic distribution in the following way. First, the dynamic distribution obtained for a specific

surface (and k_c and R) from eq 4.2 at a given approach speed and Hamaker constant A is now considered to be the "true" distribution (in which A is likewise now considered to be the "true" value of the Hamaker constant). Next, and for the same surface (and k_c and R), various quasi-static distributions are generated for a range of different inputted values of the Hamaker constant, or A_{input}. These quasi-static distributions are therefore considered to be the "approximating" distributions. The relative entropies of these quasi-static distributions with respect to the given dynamic distribution are then determined. Figure 4.7 shows plots of the relative entropy versus A_{input} at $v_c = 1000$ nm/s (a) and 200 nm/s (b) for surface F, in which the dynamic distribution was generated with $A = 100$ zJ (and with k_c and R the same as for Figure 4.4). In general, as seen in Figure 4.7, the relative entropy exhibits a reasonably sharp minimum at a particular value of A_{input}, which is then chosen to be the value of A_{eff} for the dynamic distribution. Because of inertial effects, A_{eff} will not necessarily be equal to A, although both should be nearly identical at slow enough approach speeds. This expected trend is observed in Figure 4.7, where A_{eff} is equal to 98.6 zJ at 1000 nm/s and 99.7 zJ at 200 nm/s.

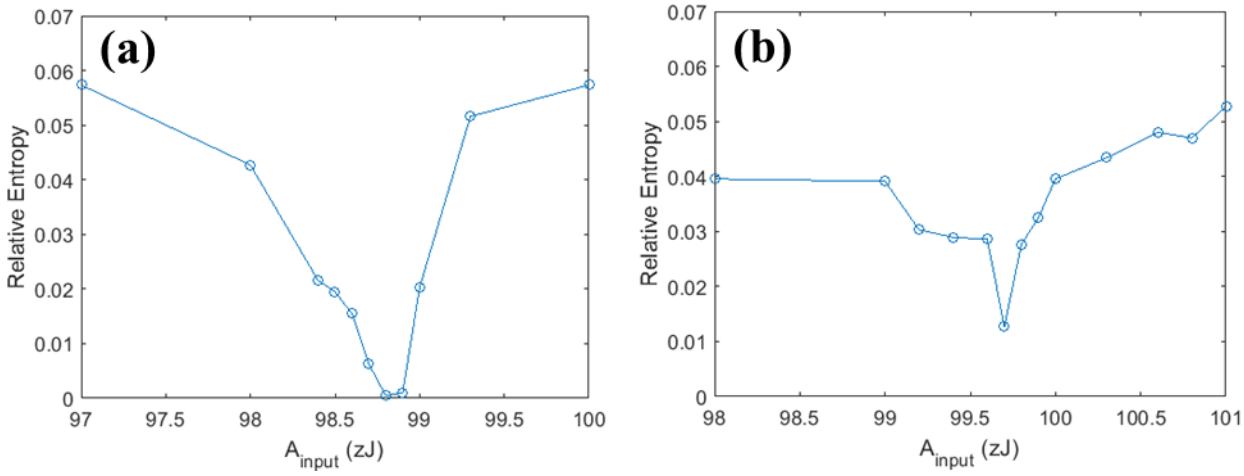

Figure 4.7 Relative entropy versus A_{input} for the cantilever approach speeds of (a) 1000 nm/s and (b) 200 nm/s for surface A (and for which A = 100 zJ). The effective Hamaker constant, which is defined to be that value of A_{input} at which the relative entropy is a minimum, is 98.6 zJ and 99.7

The corresponding plots for surfaces G and H are shown in Figure 4.8 and Figure 4.9, respectively, in which the dynamic distributions were again both generated with A = 100 zJ. The relative entropy again exhibits a reasonably sharp minimum at a particular value of A_{input}, which is chosen to be the value of the effective Hamaker constant, A_{eff}. For surface H, A_{eff} is 98.6 zJ at 1000 nm/s and approximately 99.9 zJ at 200 nm/s. For surface H, A_{eff} is 98.8 zJ at 1000 nm/s and approximately 99.9 zJ at 200 nm/s. As a side note, due to the discrete nature of the histograms, the relative entropy becomes "noisy" at small ranges of A_{input}, as shown in Figure 4.8(a) and Figure 4.9(a). However, the minima in the relative entropy are clear over a large range of values of A_{input} (*e.g.* 80-120 zJ) but become less well-defined as the range decreases. Nonetheless, the global minimum is chosen to yield A_{eff} which still yields the expected trends.

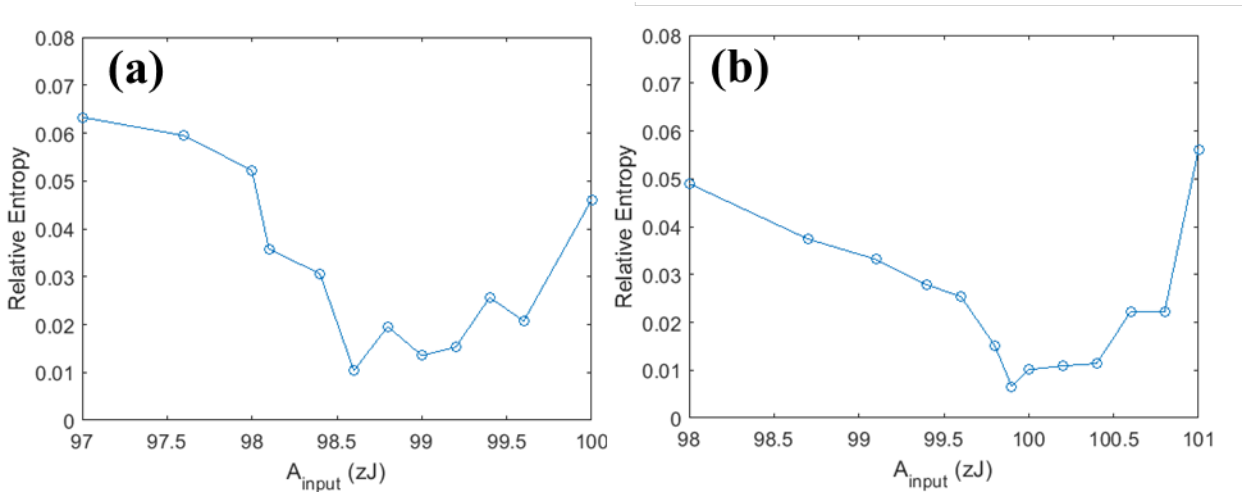

Figure 4.8 Relative entropy versus A_{input} for cantilever approach speeds of (a) 1000 nm/s and (b) 200 nm/s for surface G. The effective Hamaker constant, corresponding to that value of A_{input} at which the relative entropy is a minimum, is 98.6 zJ and 99.9 zJ for 1000 nm/s and 200 nm/s, respectively.

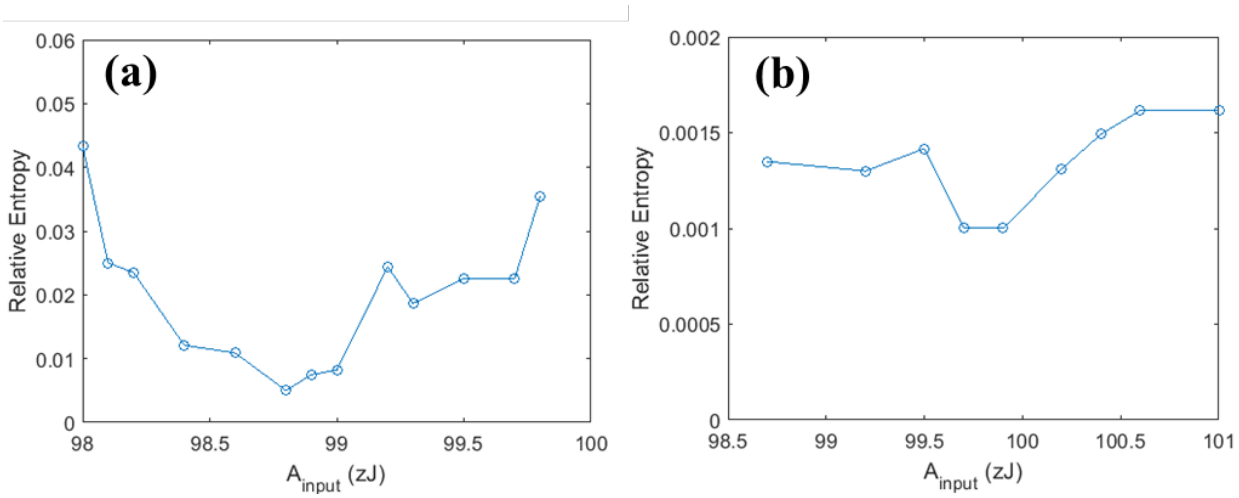

Figure 4.9 Relative entropy versus A_{input} for cantilever approach speeds of (a) 1000 nm/s and (b) 200 nm/s for surface H. The effective Hamaker constant is 98.8 zJ and 99.9 zJ for 1000 nm/s and 200 nm/s, respectively.

Figure 4.10 shows the ratio of the effective Hamaker constant to the "true" Hamaker constant (A = 100 zJ) as a function of the cantilever approach speed for the surfaces F, G and H. For each surface, A_{eff}/A approaches unity as $v_c \to 0$, which is consistent with the results shown in Figure 4.6. For comparison, the same ratio for the flat plate is also included in Figure 4.10. Because inertial effects yield smaller values of d_c compared to the quasi-static limit at any point along a given surface, $A_{eff} < A$ for $v_c > 0$ for all surfaces. Furthermore, A_{eff} decreases with an increase in v_c, which is consistent with Figures 4.3-4.5 where a dynamic distribution shifts more to the left as the approach speed increases. (For fixed cantilever properties and surface geometry, a decrease in the Hamaker constant yields, according to eq 2.9, a weaker surface-tip force which results in a smaller deflection at first contact. Hence, a dynamic value of d_c that is less than the corresponding quasi-static limit should be interpreted as arising from a weaker van der Waals force, or $A_{eff} < A$.)

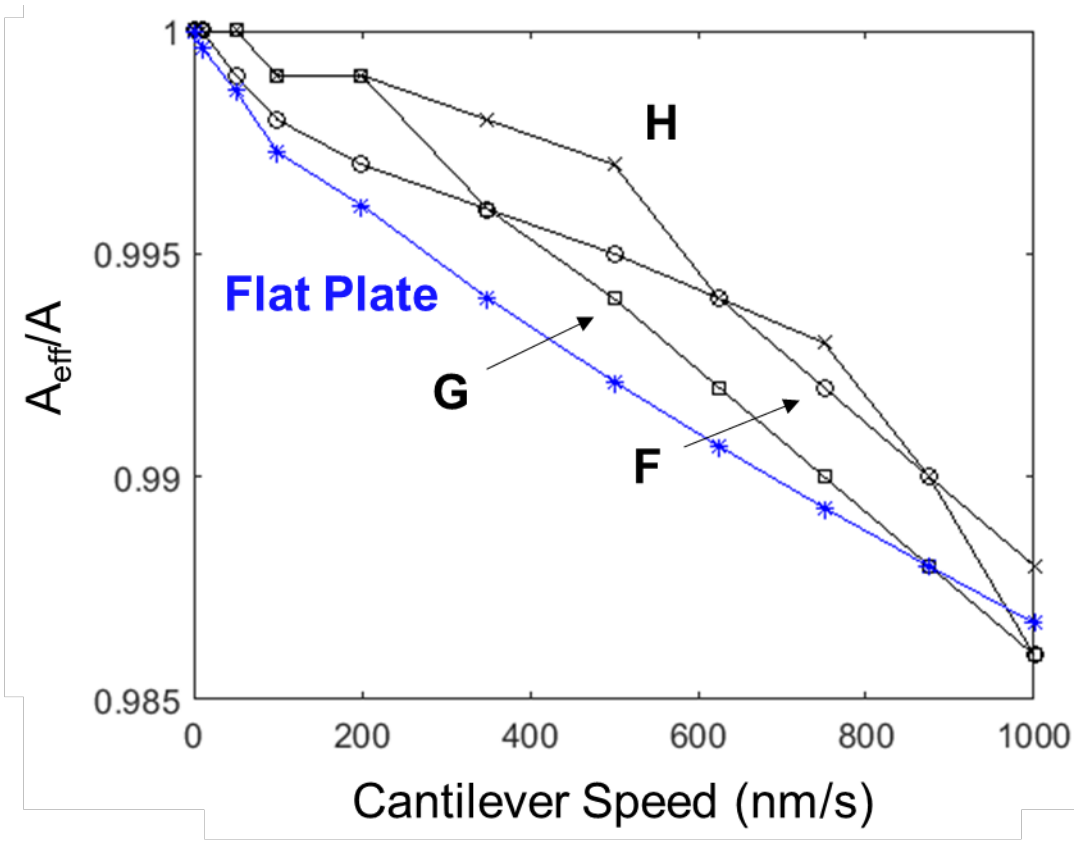

Figure 4.10 Ratio of the effective Hamaker constant, A_{eff}, to the "true" value, A, as a function of the cantilever approach speed for the three model surfaces F, G, and H, and the flat plate.

Figure 4.10 also implies that for sufficiently slow approach speeds, for which A_{eff}/A is close enough to one, the quasi-static model will provide an accurate description of the behavior of the AFM cantilever tip. Hence, there is no need to invoke the more computationally intensive dynamic model. In particular, if a deviation of 0.5% or less is considered to be insignificant, then for all surfaces the corresponding quasi-static d_c-distribution should be (nearly) identical to the dynamic distributions for approach speeds of 200 nm/s or slower. In other words, at these approach speeds, inertial effects in an AFM experiment should be essentially unobservable (at least compared to the magnitudes of the other uncertainties that typically arise). An interesting implication arises when comparing Figure 4.6 and Figure 4.10. In contrast to Figure 4.6, which shows a different trend for each surface, the behavior of the data in Figure 4.10 appears to be more

"universal". While the curves are not collapsing on top of each other, the data seems to behave more similarly than in Figure 4.6. Given the uniqueness of the d_c-distributions arising from each surface, it is interesting that this type of universal behavior is observed.

4.4 Summary

A model describing the dynamic behavior of an AFM cantilever tip was introduced and solved for a range of cantilever approach speeds. For sufficiently slow approach speeds (*i.e.* 200 nm/s or slower), the resulting d_c-distributions for several model surfaces were essentially identical to those obtained in the quasi-static limit. From this result, a computational consistency check was performed by which an effective Hamaker constant was determined from a range of inputted Hamaker constant values by minimizing the relative entropy between a quasi-static and dynamic d_c-distribution. For sufficiently slow cantilever approach speeds, A_{eff}/A approaches unity such that the quasi-static model provides an accurate description of the behavior of the AFM cantilever tip.

This chapter sets the stage for the full experimental validation of the updated approach-to-contact method in which a single self-Hamaker constant for a given material will be determined across a range of surface topographies. Similarly to the computational consistency check, the relative entropy will be minimized between model-predicted (*e.g.* derived from the quasi-static model for a given surface function) and experimental d_c-distributions for a range of inputted Hamaker constants to yield an effective Hamaker constant (*i.e.* $A_{eff,12}$). The self-Hamaker constant is then determined using eq 1.4 for a given cantilever tip material (*i.e.* A_{22}), and with a significant reduction in error compared to the original approach-to-contact method developed by Fronczak, *et al.*[79,80] Chapter 5, however, first provides a discrete Fourier transform method to

generate statistically similar surfaces from an AFM surface height scan since it is not feasible to obtain force measurements and image the same exact location on a particular surface. By generating a large number of representative surfaces, aggregate model-predicted d_c-distributions can then be obtained and compared to those obtained experimentally using the AFM. Therefore, the relative entropy can then be minimized between the model-predicted and experimental distributions to determine an effective Hamaker constant.

5. RECONSTRUCTING AFM SURFACE HEIGHT MAPS USING THE DISCRETE FOURIER TRANSFORM

5.1 Introduction

Chapter 3 provided a comprehensive computational study illustrating the effect of surface curvature on the resulting deflections at first contact of the cantilever. For these model surfaces presented in Chapter 3, both the characteristics of the surface (*i.e.* surface height map) and precise location of contact that the sphere makes with the surface are known. Unfortunately, when generating a d_c-distribution experimentally, obtaining AFM deflection curves along the same exact portion of the surface that was imaged in a separate AFM scan is not feasible. Moreover, the modified approach-to-contact method requires a comparison between the model-predicted and experimental d_c-distributions for a particular surface to obtain an effective Hamaker constant which minimizes the relative entropy between the two distributions. As such, a method is required to generate representative surface height maps, with the same overall roughness (*e.g.* the RMS roughness and distribution of peak heights), from the original AFM surface scans to ensure that a proper comparison can be made between statistically similar portions of the surface. Jaiswal *et al.*[89,108,109] developed a method utilizing a discrete Fourier transform (DFT) algorithm to generate new representative surface image with similar roughness profiles as the original surface. This chapter is concerned with detailing the mathematics of DFT, providing an analysis of the amplitude spectra of model surface functions, and outlining an extension of the method developed by Jaiswal *et al.* by which representative surfaces are generated from an existing AFM surface height map while maintaining similar roughness statistics.

5.2 Mathematics of Discrete Fourier Transforms: One-Dimensional DFT

For a discrete surface described by the surface height function, $f(x)$, with values known only at the equally spaced distance Δx in the x-direction, the integer $n = 0, \ldots, N-1$ is defined such that $x = n\Delta x$ where $N = L_x/\Delta x$ and L_x is the total length of the surface image. When computing a DFT, N is chosen to be even and of a power of 2 (*i.e.* 64, 128, 256, etc.) The DFT is given by[110]

$$F_u = \sum_{n=0}^{N-1} f_n e^{-2\pi i u n/N} \tag{5.1}$$

where f_n is the function value at a particular value of n, $u = 0, \ldots, N-1$, and $i = \sqrt{-1}$. For a given u, the corresponding wavelength of the function value $\lambda_u = N\Delta x/u$ or wavenumber, $k_u = 2\pi/\lambda_u = 2\pi u/N\Delta$. In general, and for real function values (*e.g.* f_n) , F_u is complex such that $F_u = R_u + iI_u$ or, in polar form, $|F_u| = \left({R_u}^2 + {I_u}^2\right)^{1/2}$ where the phase angle $\phi_u = \tan^{-1}\frac{I_u}{R_u}$. Thus, $F_u = |F_u|e^{i\phi_u}$ and its complex conjugate is equal to ${F_u}^* = |F_u|e^{-i\phi_u}$. In general,

$$F_{u+N} = \sum_{n=0}^{N-1} f_n e^{-2\pi i(u+N)n/N} = \sum_{n=0}^{N-1} f_n e^{-2\pi i n} e^{-2\pi i u n/N} = \sum_{n=0}^{N-1} f_n e^{-2\pi i u n/N} = F_u \tag{5.2}$$

since n is an integer such that $e^{-2\pi i n} = 1$. Also,

$$F_{N-u} = \sum_{n=0}^{N-1} f_n e^{-2\pi i(N-u)n/N} = \sum_{n=0}^{N-1} f_n e^{-2\pi i n} e^{2\pi i u n/N} = \sum_{n=0}^{N-1} f_n e^{2\pi i u n/N} \tag{5.3}$$

So, if f_n is real, $F_{N-u} = {F_u}^* = F_{-u}$ and ${F_{N-u}}^* = F_u$. In general,

$$F_0 = \sum_{n=0}^{N-1} f_n \tag{5.4}$$

which is real if f_n is real. If N is even, then $F_{N-u/2} = F_{N/2} = {F_{N/2}}^*$and so $F_{N/2}$ is also real and is given as

$$F_{N/2} = \sum_{n=0}^{N-1} f_n e^{-\pi i n} = \sum_{n=0}^{N-1} f_n(\cos n\pi - i \sin n\pi) = \sum_{n=0}^{N-1} (-1)^n f_n \tag{5.5}$$

Now, again for real f_n, $|F_u|^2 = F_u F_u{}^* = F_{N-u}{}^* F_{N-u} = |F_{N-u}|^2$ which is symmetric about $N/2$.

In general, the inverse transform is given by[110]

$$f_n = \frac{1}{N} \sum_{u=0}^{N-1} F_u e^{2\pi i u n/N} \tag{5.6}$$

Substitution of F_u in its polar form into eq 5.6 gives

$$f_n = \frac{1}{N} \sum_{u=0}^{N-1} |F_u| e^{i\phi_u} e^{2\pi i u n/N} \tag{5.7}$$

The following pairs of terms can be written when eq 5.7 is expanded (this expansion does not apply to the F_0 and $F_{N/2}$ terms)

$$f_n = \frac{1}{N} \left\{ |F_u| e^{i\phi_u} e^{2\pi i u n/N} + |F_{N-u}| e^{i\phi_{N-u}} e^{2\pi i (N-u) n/N} \right\} + \cdots \tag{5.8}$$

which can then be simplified to

$$f_n = \frac{1}{N} \left\{ |F_u| e^{i\phi_u} e^{2\pi i u n/N} + |F_u| e^{-i\phi_u} e^{-2\pi i u n/N} \right\} + \cdots \tag{5.9}$$

or

$$f_n = \frac{2}{N} |F_u| \cos\left(2\pi \frac{un}{N} + \phi_u\right) + \cdots \tag{5.10}$$

where the amplitude of a particular wavelength component is $\frac{2}{N}|F_u|$. Eq 5.7 can then be written as

$$f_n = \frac{F_0}{N} + (-1)^n \frac{F_{N/2}}{N} + \sum_{u=1}^{N/2-1} 2 \frac{|F_u|}{N} \cos\left(2\pi \frac{un}{N} + \phi_u\right) \tag{5.11}$$

or

$$f_n = \frac{F_0}{N} + (-1)^n \frac{F_{N/2}}{N} + \sum_{u=1}^{N/2-1} 2\frac{|F_u|}{N} \cos\left(2\pi u \frac{(x_n - x_0)}{N\Delta x} + \phi_u\right) \quad (5.12)$$

where $x_n - x_0 = n\Delta x$ or $n = \frac{x_n - x_0}{\Delta x}$.

Eq 5.1 can be used to determine the Fourier coefficients from a series of discrete spatial data and converted back to the space domain using eq 5.12. Eq 5.12 decomposes the surface function into a series of cosine terms with amplitude $2\frac{|F_u|}{N}$, wavelengths $\lambda_u = N\Delta x/u$, and phase angles ϕ_u. The amplitude spectrum of a discrete surface height function provides information regarding the magnitude of each contributing wavenumber across the entire Fourier space providing a unique "signature" of the transformed function. For a one-dimensional surface height function, the amplitude spectrum is a plot of the amplitude, $|F_u| = \left({R_u}^2 + {I_u}^2\right)^{1/2}$ for each wavelength component from $u = 0 \ldots N-1$. Because an amplitude spectrum is symmetric about $u = N/2$, most amplitude spectra are plotted as $2\frac{|F_u|}{N}$ versus $u = 0 \ldots N/2$.

For a surface comprised of a series of cosine (or sine) terms, the individual phase angles associated with each term may be independently shifted from 0 to 2π (or 0 to 360 degrees) while maintaining the same exact amplitude spectrum. The shifting of one or more values of ϕ_u results in simultaneous constructive and destructive interference of the surface function causing features of the surface to vary between the new and original surface. For a wavelength component F_u, the corresponding shifted component is equal to ${F'}_u = F_u e^{-i{\phi'}_u}$, where ${\phi'}_u$ is the phase shift in radians. In order to properly maintain identical amplitude spectra between surface functions, when shifting the phase angle of a particular wavelength component, (*e.g.* $u = 1$) the corresponding complex conjugate of the wavelength component must be adjusted accordingly (*e.g.* $u = 255$ for

$N = 256$). Figure 5.1 shows the proper mapping for shifting the phase angles across a one-dimensional surface height function.

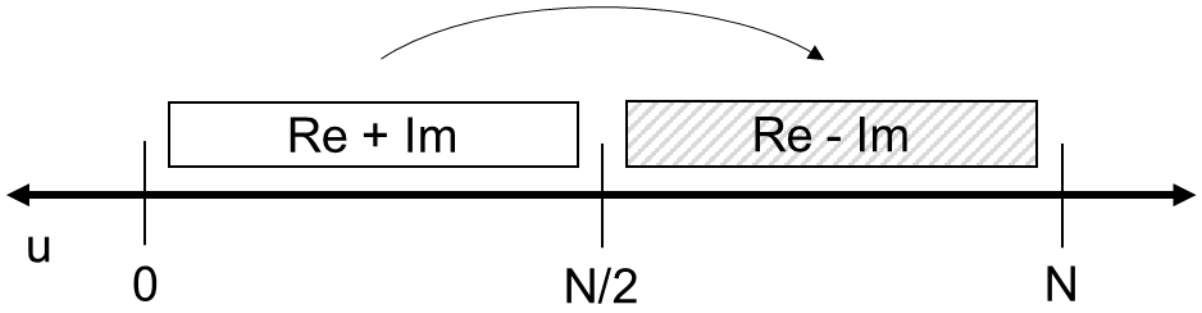

Figure 5.1 Schematic representation of shifting the wavelength components of the DFT of a one-dimensional surface height function by phase angle ϕ'_u.

Section 5.4 provides examples of amplitude spectra and the analysis of shifting the phase angles on a range of one-dimensional surface height functions.

5.3 Mathematics of Discrete Fourier Transforms: Two-Dimensional DFT

The two-dimensional extension to the discrete Fourier transform is as follows. For a discrete surface height map, $h(x, y)$, with values known only at the equally-spaced distances Δx and Δy in the x- and y-directions, respectively, the integers $n = 0, \dots, N-1$ and $m = 0, \dots, M-1$ are defined such that $x = n\Delta x$ and $y = m\Delta y$, where $N = L_x/\Delta x$ and $M = L_y/\Delta y$, and L_x and L_y are the total lengths in each direction of the chosen image. N and M are chosen to be even and of a power of 2 (*i.e.* 64, 128, 256, etc.) The DFT is given by[111]

$$F_{uv} = \sum_{n=0}^{N-1} \sum_{m=0}^{M-1} f_{nm} e^{-2\pi i \left(\frac{un}{N} + \frac{vm}{M}\right)} \tag{5.13}$$

where $u = 0, \dots, N-1$ and $v = 0, \dots, M-1$. For a given u and v, the wavevector of the corresponding sinusoidal components is $\vec{k} = (k_u, k_v)$, in which $k_u = 2\pi u/N\Delta x$ and $k_v =$

$2\pi v/M\Delta y$, and the wavelength is $\lambda = 2\pi/k$, where $k = (k_u^2 + k_v^2)^{1/2}$. In general, $F_{uv} = F_{u+N,v+M}$ and $F_{00} = \sum_{n=0}^{N-1}\sum_{m=0}^{M-1} f_{nm}$. For an even N and M,

$$F_{\frac{NM}{2\,2}} = \sum_{n=0}^{N-1}\sum_{m=0}^{M-1} f_{nm}e^{-\pi in}e^{-\pi im} = \sum_{n=0}^{N-1}\sum_{m=0}^{M-1}(-1)^{n+m}f_{nm} \tag{5.14}$$

Also, if f_{nm} is real,

$$\begin{aligned} F_{N-u,M-v} &= \sum_{n=0}^{N-1}\sum_{m=0}^{M-1} f_{nm}e^{-2\pi i(N-u)n/N}e^{-2\pi i(M-v)m/M} \\ &= \sum_{n=0}^{N-1}\sum_{m=0}^{M-1} f_{nm}e^{-2\pi in}e^{-2\pi im}e^{2\pi iun/N}e^{2\pi ium/M} = {F_{uv}}^* = F_{-u,-v} \end{aligned} \tag{5.15}$$

and so ${F_{N-u,M-v}}^* = F_{uv} = {F_{-u-v}}^*$. Now, again for real f_{nm}, $|F_{uv}|^2 = F_{uv}{F_{uv}}^* = {F_{N-u,M-v}}^* F_{N-u,M-v} = \left|F_{N-u,M-v}\right|^2$ so $|F_{uv}| = \left|F_{N-u,M-v}\right|$. Finally,

$$F_{N-u,v} = \sum_{n=0}^{N-1}\sum_{m=0}^{M-1} f_{nm}e^{2\pi iun/N}e^{-2\pi ivm/M} = F_{-u,v} = {F_{u,-v}}^* \tag{5.16}$$

and $F_{u,M-v} = F_{u,-v} = {F_{-u,v}}^*$ so ${F_{N-u,v}}^* = F_{u,M-v}$. Similarly to the one-dimensional case, $F_{uv} = R_{uv} + iI_{uv}$ or, in polar form, $|F_{uv}| = \left({R_{uv}}^2 + {I_{uv}}^2\right)^{1/2}$ where the phase angle $\phi_{uv} = \tan^{-1}\frac{I_{uv}}{R_{uv}}$ and $F_{uv} = |F_{uv}|e^{i\phi_{uv}}$ and ${F_{uv}}^* = |F_{uv}|e^{-i\phi_{uv}}$. Finally, the inverse transform is given by[111]

$$f_{nm} = \frac{1}{NM}\sum_{u=0}^{N-1}\sum_{u=0}^{M-1} F_{uv}e^{2\pi i\left(\frac{un}{N}+\frac{vm}{M}\right)} \tag{5.17}$$

Similarly to eq 5.1, eq 5.13 can be used to determine the Fourier coefficients from a series of two-dimensional discrete spatial data and converted back to the space domain using eq 5.17. The surface function is broken down into a series of cosine terms with amplitude $2\,|F_{uv}|/N$, wavelengths $\lambda = 2\pi/k$, with $k = (k_u^2 + k_v^2)^{1/2}$, and phase angles ϕ_{uv}. For a two-dimensional surface height function, the amplitude spectrum is a plot of the amplitude, $|F_{uv}| =$

$\left({R_{uv}}^2 + {I_{uv}}^2\right)^{1/2}$ for each wavelength component from $u = 0 \ldots N-1$ and $v = 0 \ldots M-1$. Because an amplitude spectrum is symmetric about $u = N/2$, $v = M/2$ most amplitude spectra are plotted as $2|F_{uv}|/N$ versus $u = 0 \ldots N/2$ and $v = 0 \ldots M/2$.

Similarly to the one-dimensional case, the individual phase angles comprising the surface may be independently shifted from 0 to 2π (or 0 to 360 degrees) while maintaining the same exact amplitude spectrum. For a wavelength component F_{uv}, the corresponding shifted component is equal to $F'_{uv} = F_{uv}e^{-i\phi'_{uv}}$, where ϕ'_{uv} is the phase shift in radians. Again, in order to properly maintain identical amplitude spectra between surface functions, the corresponding complex conjugate of the wavelength component must be adjusted accordingly. Figure 5.2 shows the proper mapping for shifting the phase angles across a one-dimensional surface height function.

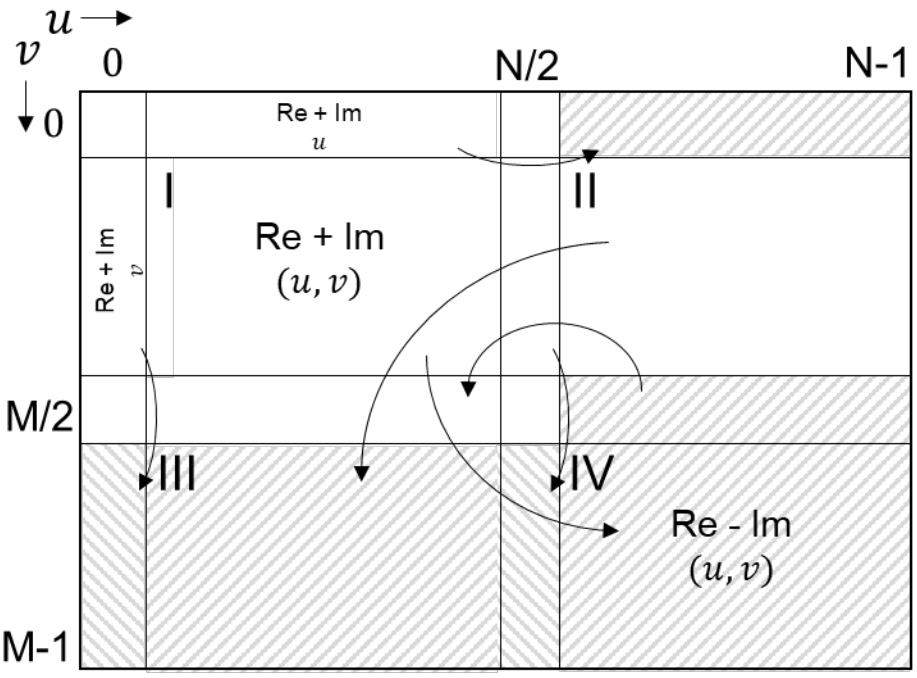

Figure 5.2 Schematic representation of shifting the wavelength components of the DFT of a two-dimensional surface height function by phase angle ϕ'_{uv}. (Adapted from J. Fessler, 2D DFT.)

The DFT of the two-dimensional surface height data is comprised of an N by M data matrix where the first row and column contain the wavelength components $u = 0 \ldots N-1$, $v = 0 \ldots N-1$, respectively. Similarly to the one-dimensional case, $u = v = N/2 = M/2$ at the midpoint of the row/column and the remaining data (*i.e.* $u = v = N/2 \ldots N-1$) is the corresponding complex conjugate. Quadrant I of the matrix comprises the (u, v) wavelength components that range from $(u, v) = (1,1)$ to $(N/2-1, M/2-1)$, and quadrant IV contains the complex conjugate values. Quadrant II comprises the (u, v) wavelength components that range from $(u, v) = (N/2+1, 1)$ to $(N-1, M/2-1)$, and quadrant III contains the complex conjugate values which range from $(u, v) = (1, M/2+1)$ to $(N/2-1, M-1)$. Proper shifting of the phase angle comprising one or more wavelength components again requires multiplying by $e^{-i\phi'_{uv}}$ and updating the corresponding complex conjugate values in the matrix. Section 5.5 provides examples of amplitude spectra and the analysis of shifting the phase angles on a range of two-dimensional surface height functions.

5.4 Analysis of the Amplitude Spectra of One-Dimensional Surface Height Functions

The amplitude spectrum of a discrete surface height function provides information regarding the magnitude of each contributing wavenumber across the entire Fourier space providing a unique "signature" of the transformed function. For a one-dimensional surface height function, the amplitude spectrum is a plot of the amplitude, $|F_u| = \left({R_u}^2 + {I_u}^2\right)^{1/2}$ for each wavelength component from $u = 0 \ldots N-1$. Because an amplitude spectrum is symmetric about $u = N/2$, most amplitude spectra are plotted as $2|F_u|/N$ versus $u = 0 \ldots N/2$. Figure 5.3 shows the amplitude spectrum for the surface function $h(x) = \cos(x)$, with $N = 256$, evaluated over the domain 0 to 2π.

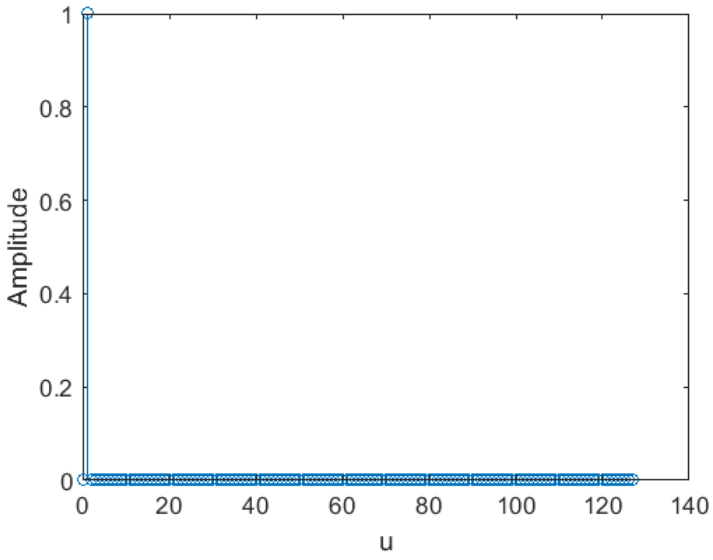

Figure 5.3 Amplitude spectrum of $h(x) = \cos(x)$ with $N = 256$, evaluated over the domain 0 to 2π.

Because the function is comprised of a single cosine with an amplitude of 1, the amplitude spectrum shows one peak at $u = 1$. Figure 5.4 shows the amplitude spectrum of the function $h(x) = \cos(x) + 2$ which is a cosine shifted up by 2.

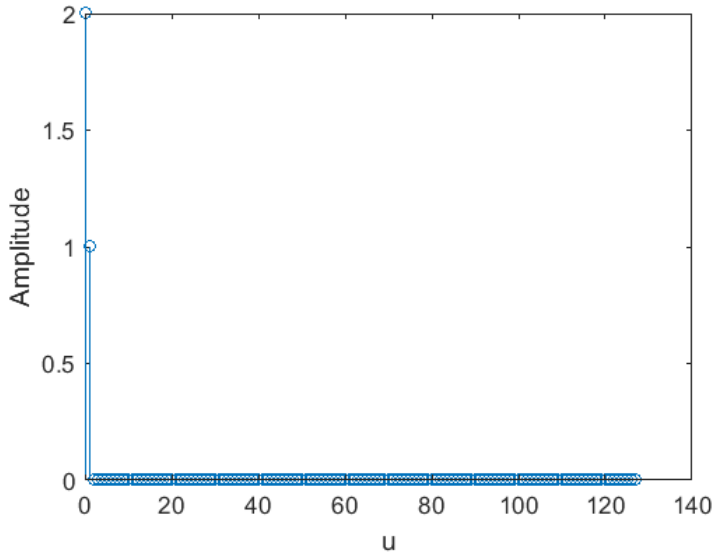

Figure 5.4 Amplitude spectrum of $h(x) = \cos(x) + 2$ with $N = 256$, evaluated over the domain 0 to 2π.

The amplitude shows a peak of 2 at $u = 0$ corresponding to the shifting of the function by 2, in addition to the peak at $u = 1$. Figure 5.5 shows the amplitude spectrum of the function $h(x) = \cos(x) + 2\cos(5x)$.

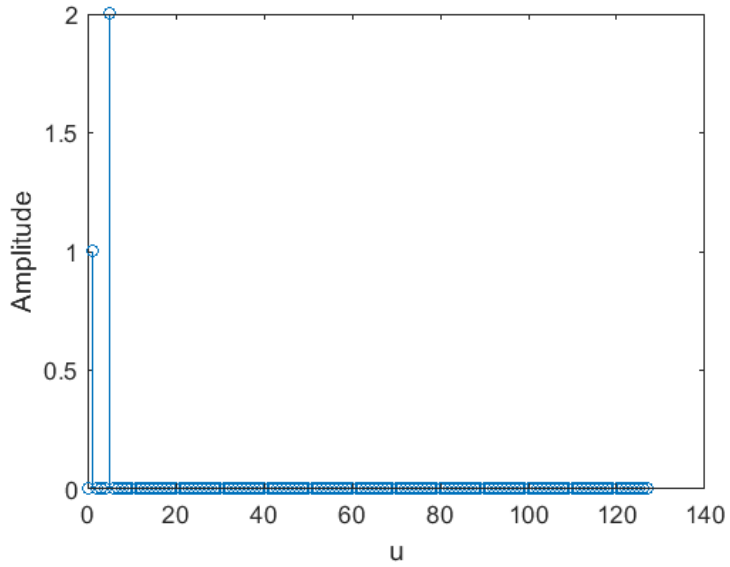

Figure 5.5 Amplitude spectrum of $h(x) = \cos(x) + 2\cos(5x)$ with $N = 256$, evaluated over the domain 0 to 2π.

Here, the amplitude spectrum shows a peak of 1 at $u = 1$ and a peak of 2 at $u = 5$ corresponding to the additional cosine term.

A phase angle plot offers further information regarding the individual values of ϕ_u comprising the surface height function. As noted previously, $\phi_u = \tan^{-1}\frac{I_u}{R_u}$. Figure 5.6 shows the amplitude spectrum and corresponding phase angle plot for $h(x) = \sin(\mathrm{x})$. While the amplitude spectrum is identical to Figure 5.3, the phase angle plot shows a peak at 90° at $u = 1$ since $\sin(\mathrm{x}) = \cos(\mathrm{x} + \pi/2)$ and $\phi_u = \pi/2$ radians (90 degrees).

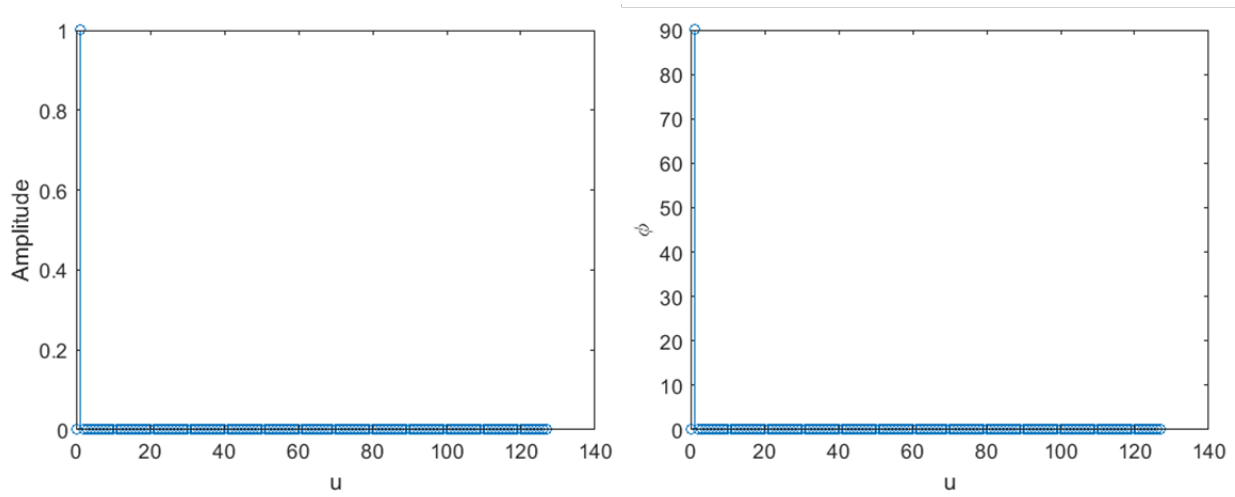

Figure 5.6 Amplitude spectrum and corresponding phase angle plot for $h(x) = \sin(\mathrm{x})$. The amplitude spectrum is identical to $h(x) = \cos(\mathrm{x})$ and the phase angle plot shows a peak of 90° at $u = 1$ since $\sin(\mathrm{x}) = \cos(\mathrm{x} + \pi/2)$.

For example, the real (the cosine component) and imaginary (the sine component) contributions to the Fourier coefficients of the DFT of the surface height function $h(x) = 5\cos(\mathrm{x}) + 2\cos(3x) + 4\sin(10x)$ are F_1, F_3, and F_{10} and equal (2.5, 0), (1, 0) and (0, -2), respectively with N = 256. The corresponding complex conjugate values of F_{255}, F_{253}, and F_{246} are (2.5, 0), (1, 0) and (0, +2), respectively. Shifting the phase angle comprising the three terms in the function requires multiplying F_1, F_3, and F_{10} by $e^{-i\phi' u}$ where ϕ'_u is the phase shift (in radians) for $u = 1, 3, 10$. The corresponding complex conjugate values must also be updated as well to ensure

conservation of the amplitude spectrum. Figure 5.7 shows a comparison plot of the surface height function $h(x) = 5\cos(x) + 2\cos(3x) + 4\sin(10x)$ before (blue) and after (red) a random phase shift. The amplitude spectrum (b) is also provided which is identical between both surfaces.

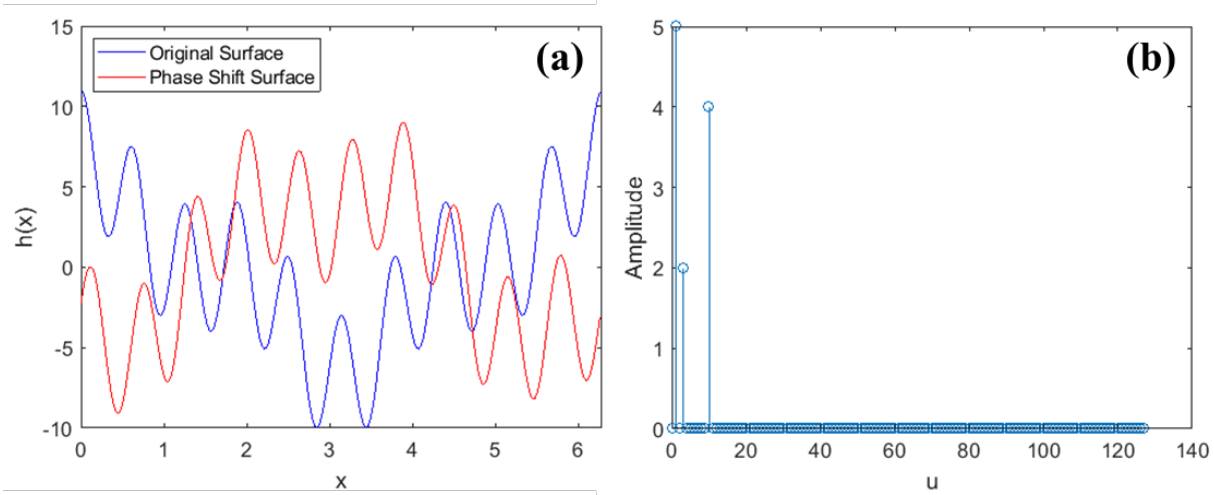

Figure 5.7 (a) Plot of the function $h(x) = 5\cos(x) + 2\cos(3x) + 4\sin(10x)$ (blue) and function after undergoing a phase shift (red). (b) Amplitude spectrum of both functions.

For a discrete vector of data points comprising a surface height function, the RMS roughness of the surface is simply the standard deviation of the data. The RMS roughness is of particular interest because it provides a quantitative metric to characterize the roughness scale of a surface. While shifting the phase angles comprising a surface height function causes simultaneous constructive and destructive interference of the surface, the RMS roughness is conserved. Therefore, it is possible to generate an infinite number of surfaces with the same RMS roughness albeit with different surface topographies. Therefore, the resulting model-predicted d_c -distributions, whose shape and range of individual d_c-values are a function of the topography of the surface, will vary between surfaces. This important result sets the stage for the surface reconstruction method which is discussed later in this chapter.

5.5 Analysis of the Amplitude Spectra of Two-Dimensional Surface Height Functions

For a two-dimensional surface height function, the amplitude spectrum is a plot of the amplitude, $|F_{uv}| = \left({R_{uv}}^2 + {I_{uv}}^2\right)^{1/2}$ for each wavelength component from $u = 0 \ldots N-1$, $v = \cdots M-1$. Similarly to the one-dimensional amplitude spectrum, the two-dimensional spectrum is plotted as $2|F_{uv}|/NM$ as a function of $u = 0 \ldots N/2$ and $v = 0 \ldots N/2$, along with intermediate points (u, v) altogether comprising an amplitude spectrum matrix (rather than a one-dimensional vector). Figure 5.8 shows the amplitude spectrum for the surface function $h(x, y) = \cos(x)$, with $N = M = 256$, evaluated over the domain 0 to 2π.

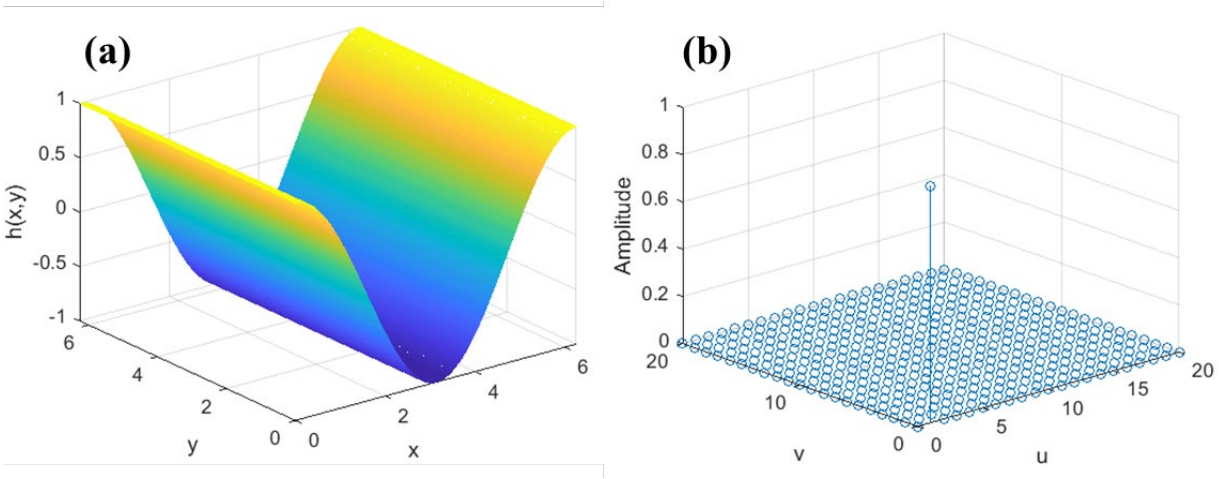

Figure 5.8 (a) A mesh plot of the surface height function $h(x, y) = \cos(x)$ and (b) corresponding amplitude spectrum.

The amplitude spectrum shows a single peak at $u = 1$ because $h(x, y)$ is only a function of x. Figure 5.9 shows the amplitude spectrum for the surface height function $h(x, y) = \cos(x + y)$.

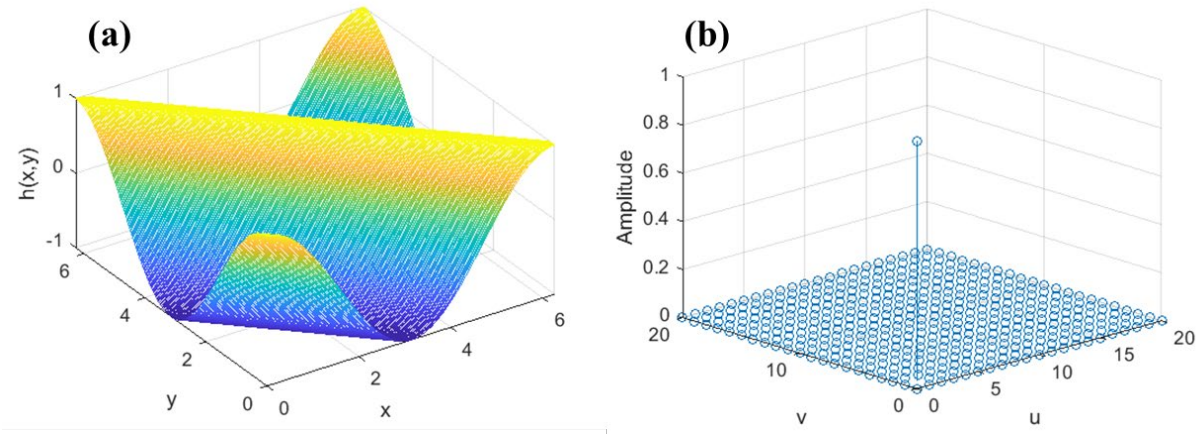

Figure 5.9 (a) A mesh plot of the surface height function $h(x, y) = \cos(x + y)$ and (b) corresponding amplitude spectrum.

Now, a single peak exists at $(u, v) = 1$ since the surface height function is a function of both x and y. Figure 5.10 shows the amplitude spectrum for the surface height function $h(x, y) = \cos(x) + \sin(x)$.

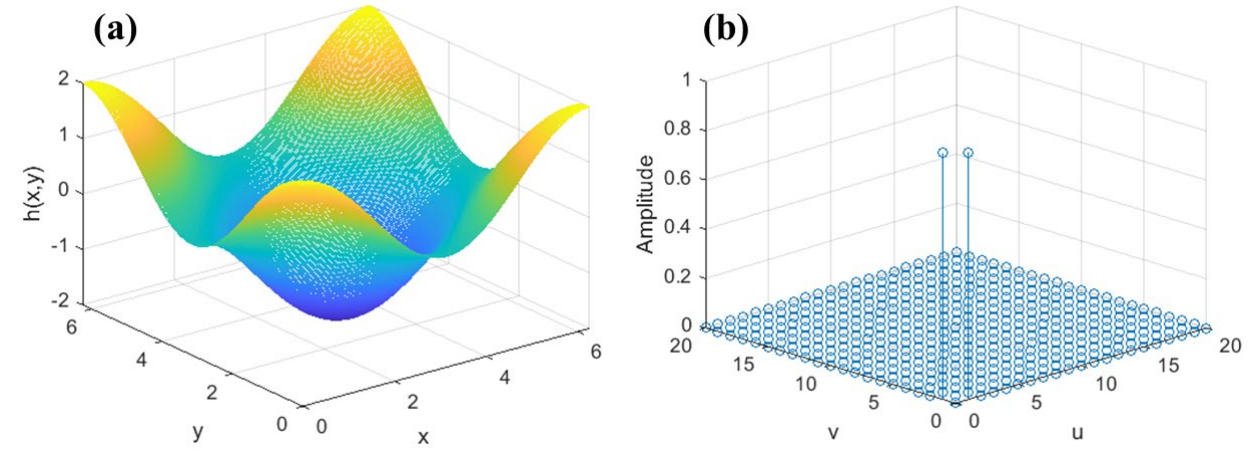

Figure 5.10 (a) A mesh plot of the surface height function $h(x, y) = \cos(x) + \sin(x)$ and (b) corresponding amplitude spectrum.

This surface is the egg-crate surface shown in Chapter 3. The amplitude spectrum shows two peaks, one at $u = 1$ and one at $v = 1$. Finally, Figure 5.11 shows the amplitude spectrum for the

surface height function $h(x,y) = \cos(x) + \cos(y) + 3\cos(5x) + 2\cos(4y) + 2\cos(10x + 10y)$.

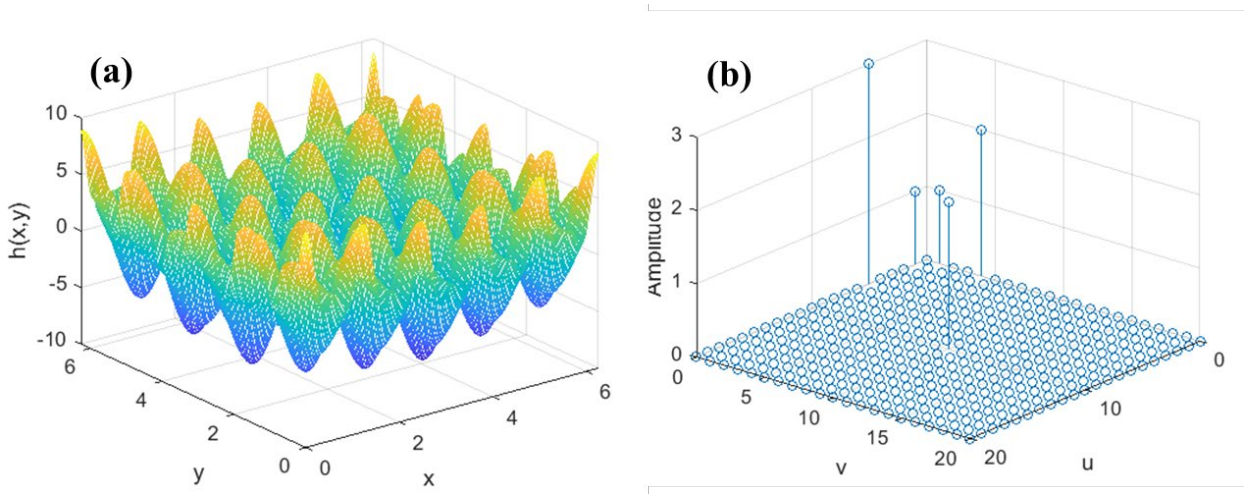

Figure 5.11 A mesh plot of the surface height function $h(x,y) = \cos(x) + \cos(y) + 3\cos(5x) + 2\cos(4y) + 2\cos(10x + 10y)$ and (b) corresponding amplitude spectrum.

In this case, the amplitude spectrum shows peaks of 1 and 3 at $u = 1$ and 5, 1 and 2 at $v = 1$ and 4, and 2 at $(u,v) = 10$. Figure 5.12 shows a comparison mesh plot of the surface height function $h(x,y) = \cos(x) + \cos(y) + 3\cos(5x) + 2\cos(4y) + 2\cos(10x + 10y)$ which has undergone a phase shift along all nonzero wavelength components. The amplitude spectrum is identical to Figure 5.11(b), along with the RMS roughness.

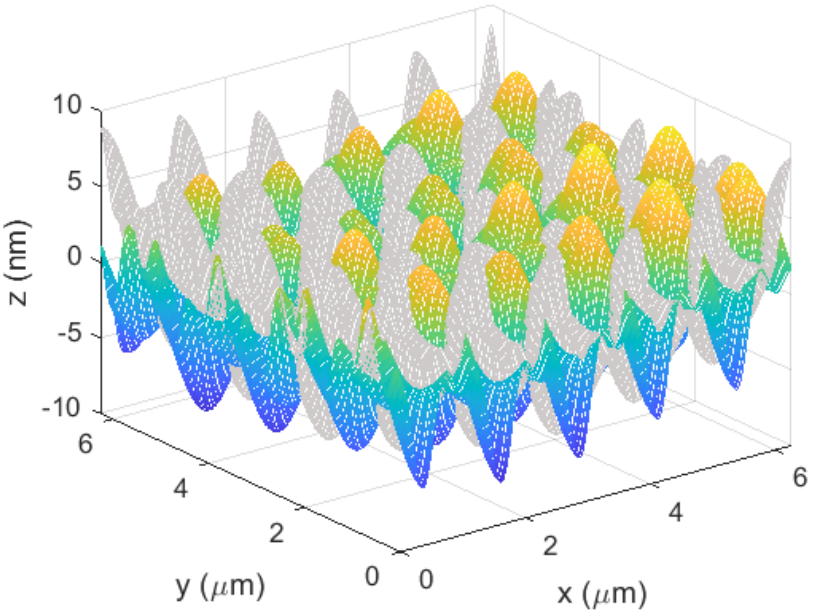

Figure 5.12 Mesh plot of the surface height function $h(x, y) = \cos(x) + \cos(y) + 3\cos(5x) + 2\cos(4y) + 2\cos(10x + 10y)$ showing the original (gray) and shifted (color) surfaces.

5.6 Generating Representative AFM Surface Height Functions from an AFM Image Scan

5.6.1 Surfaces Comprised of a Small Range in Peak Heights

The modified approach-to-contact method necessitates a comparison between the model-predicted and experimental d_c-distributions for a particular surface to obtain an effective Hamaker constant. As such, a method is required to generate representative surface height maps, with the same overall roughness, from the original AFM surface scans to ensure that a proper comparison can be made between statistically similar portions of the surface since force and imaging experiments cannot be conducted along the same exact portion of a surface. Jaiswal *et al.*[89,108,109] developed a method utilizing a discrete Fourier transform (DFT) algorithm to generate new representative surface image with similar roughness profiles as the original surface. This DFT method ensures that the root-mean-squared (RMS) roughness of each representative surface height map remains constant and matches that of the original surface scan, while also generating surfaces with nearly identical

distributions of the various peak heights. This section is concerned with detailing the DFT method in the context of generating representative surface height images from an AFM surface scan which are needed as inputs to the modified approach-to-contact method to obtain model-predicted d_c-distributions.

As a summary, for a discrete surface height map, $h(x, y)$, with values known only at the equally-spaced distances Δx and Δy in the x- and y-directions, respectively, the integers $n = 0, \dots, N-1$ and $m = 0, \dots, M-1$ are defined such that $x = n\Delta x$ and $y = m\Delta y$, where $N = L_x/\Delta x$ and $M = L_y/\Delta y$, and L_x and L_y are the total lengths in each direction of the chosen image. The DFT of the real function $h(n, m)$ yields the complex-valued function, $H(u, v)$, which is now based on the integers $u = 0, \dots, N-1$ and $v = 0, \dots, M-1$. For a given u and v, the wavevector of the corresponding sinusoidal components is $\vec{k} = (k_u, k_v)$, in which $k_u = 2\pi u/N\Delta x$ and $k_v = 2\pi v/M\Delta y$, and the wavelength is $\lambda = 2\pi/k$, where $k = (k_u^2 + k_v^2)^{1/2}$.

As an example, a 10 μm by 10 μm surface height map of an amorphous silica surface was obtained via contact mode AFM using a Multimode 8 with a Bruker RTESPA-300 probe (nominal values of $k_c = 40$ N/m and resonance frequency f_0 = 300 kHz). A representative resulting scan is shown in Figure 5.13(a).

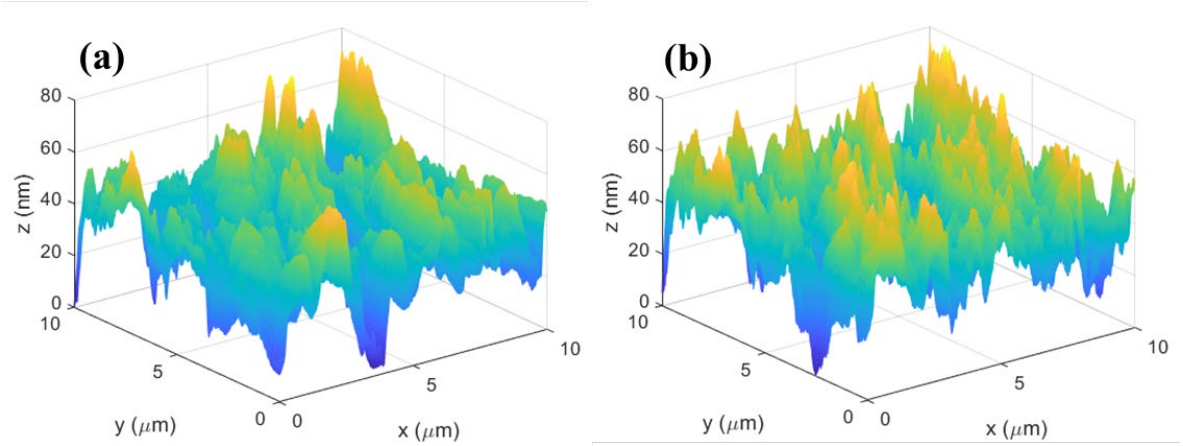

Figure 5.13 (a) A 10 by 10 micron experimentally obtained AFM scan of an amorphous silica surface, which has an RMS of 10.0 nm. (b) A reconstructed image of the surface shown in (a) obtained with the discrete Fourier transform method. The RMS of this surface is also 10.0 nm and also has other statistically similar characteristics as the original AFM surface scan.

The resulting amplitude spectrum of the original AFM image scan, or $|H(u,v)|/NM$, is provided in Figure 5.14, for which $N = M = 512$ and $\Delta x = \Delta y = 19.5$ nm. The surface is comprised mainly of long wavelength spatial contributions ($u, v < 20$ or $\lambda >$ 353 nm), with very small contributions from the shorter wavelengths. Because the mean height of the surface was set to zero, the constant term ($u, v = 0$) in the amplitude spectrum is also equal to zero.

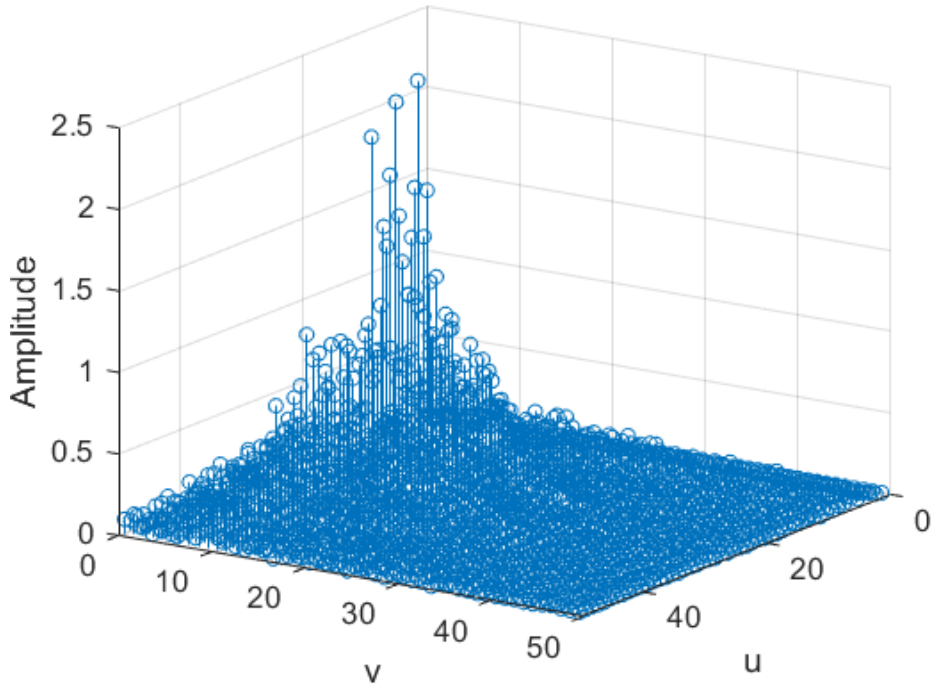

Figure 5.14 Amplitude spectrum of the AFM surface scan shown in Figure 5.13(a).

Next, various representative surface height maps with the same amplitude spectrum were generated by randomly varying only the phase angles associated with a particular wavelength component taking note of the required connections between the various corresponding conjugate pairs as illustrated in Figure 5.2. The adhesion force between the chosen sphere radii and the surface of interest is, however, driven mainly by the underlying long wavelength contributions, while the short wavelength features on the surface serve as "random noise", minimally influencing the adhesion force. This result is evidenced in Figure 3.2 and Figure 3.4 which show two surfaces with similar contact loci but with different d_c-distributions due to the presence of small-scale (high frequency, short wavelength) surface roughness on the surface shown in Figure 3.2(b). Therefore, in order to generate representative surface height maps that maintain the same overall force profiles (*i.e.* nearly identical distributions of deflections at first contact), the phase angles of the long wavelength features were left unchanged while only the phase angles of the short wavelength

features ($u, v \geq 20$), including their conjugate pairs, were randomly varied (which still does not alter the resulting amplitude spectrum). After varying these phase angles, an inverse transform was then carried out to produce a new surface image with identical RMS roughness and very similar surface height distributions. The surface height distributions, or distribution of all the individual height values comprising the surface, corresponding to the two surfaces shown in Figure 5.13 (the original AFM image scan and one of the representative images generated via the DFT method) are shown in Figure 5.15. These plots were obtained by converting the matrix of height values comprising each surface into a probability distribution plot of heights. These distributions show only positive deviations because each surface was shifted upward so that the largest negative deviation was set to 0 nm.

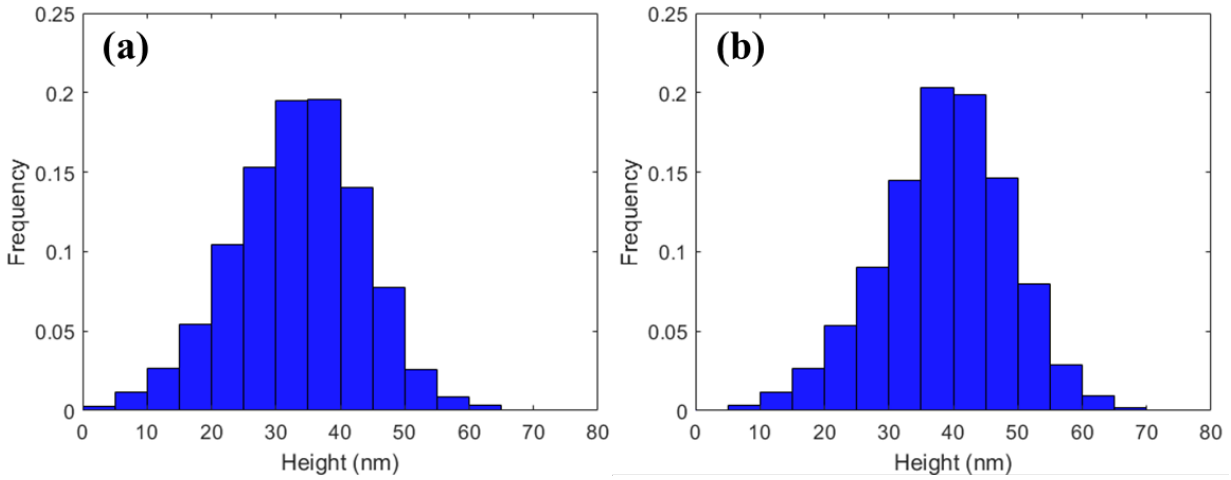

Figure 5.15 Surface height distributions for (a) the original AFM surface image shown in Figure 5.13(a) and (b) the representative surface shown in Figure 5.13(b) generated from the DFT method. By setting the minimum height value of each surface to 0 nm, the height distributions show the frequency of only positive deviations across a range of height values.

The DFT method was further utilized for an experimentally obtained AFM scan of a stainless steel surface shown in Figure 5.16(a). The reconstructed surface is given in Figure 5.16(b) and the RMS

roughness of both surfaces is 12.8 nm. The reconstructed surface shows a slight difference in the short wavelength / high frequency features (the small scale roughness) while maintaining the same distinguishing long wavelength features.

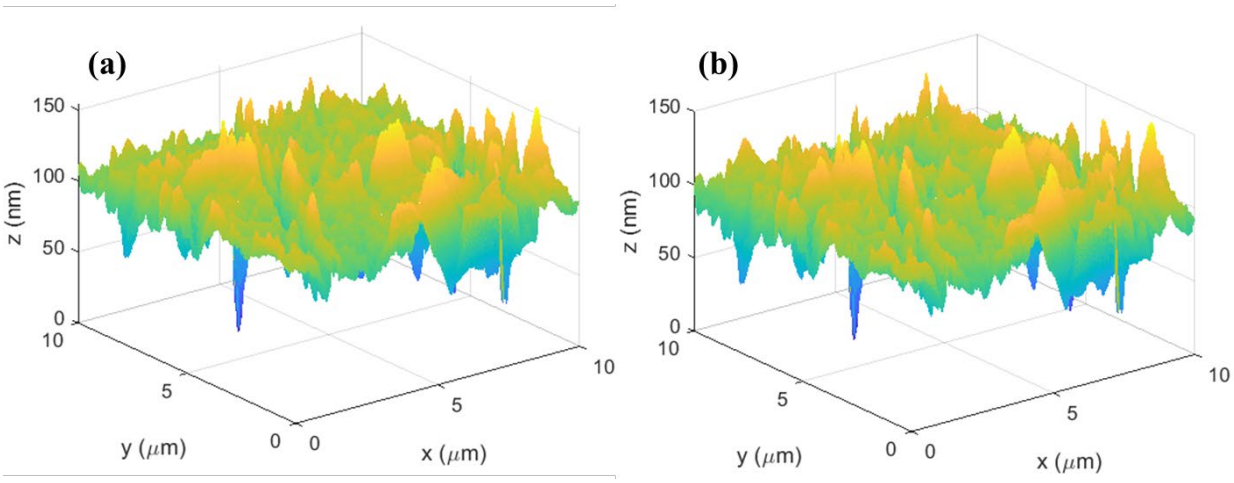

Figure 5.16 (a) A 10 by 10 micron experimentally obtained AFM scan of stainless steel surface, which has an RMS of 12.8 nm. (b) A reconstructed image of the surface shown in (a) obtained with the discrete Fourier transform method. The RMS of this surface is also 12.8 nm and also has other statistically similar characteristics as the original AFM surface scan.

5.6.2 Surfaces Comprised of Large Outlier Peaks

The aforementioned surface reconstruction method is applicable to generally "smooth" surfaces, or surfaces that do not exhibit any large peaks much greater than the average peak height. In Figure 5.15, the average height (after shifting the surface upwards such that all deviations in height are positive) is 38 nm with a standard deviation of 10 nm. All positive deviations in the height greater than the mean (*e.g.* height values greater than 38 nm) fall within the 99% confidence interval or approximately three standard deviations from the mean. However, it was found that when applying the DFT method in Section 5.6.1 to a surface containing peaks with heights extending beyond three standard deviations from the mean, these peaks would be removed from the reconstructed surface despite preserving the RMS roughness. For example, Figure 5.17(a)

shows a surface with several large peaks extending beyond several standard deviations of the mean height (in this case, the mean surface height is set to 0 nm and the standard deviation of the height is 1.7 nm). Figure 5.17(b) shows the reconstructed surface using the DFT method described in Section 5.6.1. The characteristic roughness profile of the surface is significantly altered as many of the large peaks above roughly three standard deviations from the mean, or approximately 5.6 nm, do not remain on the reconstructed surface or are reduced in height (the overall small-scale roughness appears to increase in size while the size of the large peaks decrease). Therefore, a modification to the surface reconstruction method was developed to preserve the large peaks present on the surface while generating statistically-similar surfaces, and more importantly, those with similar roughness profiles.

The modified surface reconstruction method first identifies large, outlier peaks on the surface and removes them from the surface, leaving the background surface. The height and width of each outlier peak are subsequently determined, and a distribution of widths and peaks is generated as well as a representative outlier peak of height and width based on the average of the distribution. A discrete Fourier transform is then performed on the remaining surface to obtain a new background surface. Finally, the representative outlier peak is scaled by a random peak height and width from the distribution and placed randomly on the surface. This process continues until all peak heights and widths are selected from the distribution. Figure 5.17 shows a 10 by 10 micron experimentally obtained AFM scan of an amorphous silica surface containing numerous large peaks extending from the surface.

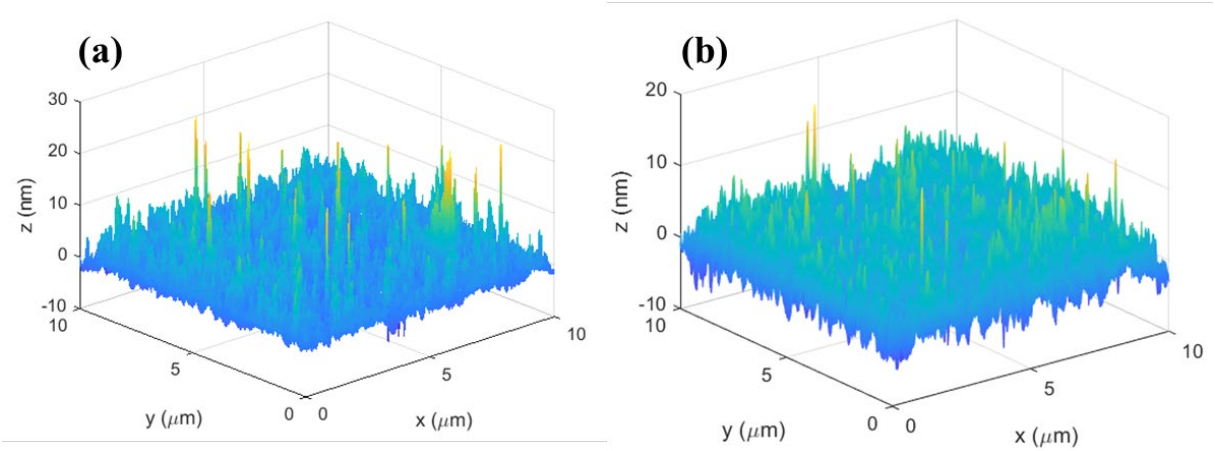

Figure 5.17 A 10 by 10 micron experimentally obtained AFM scan of an amorphous silica surface containing numerous large peaks extending from the surface.

First, the standard deviation (or RMS roughness) of the surface is calculated. Then, a cut-off height is computed such that all peaks greater than the cut-off height, or outliers, are removed from the surface (the height of the surface at the former location of the outlier peak is set to the cut-off height). The cut-off value is determined by $z_p\sigma$, where z_p is the quantile of the standard normal distribution and σ is the standard deviation of the data.[112] For the 99.9 percentile, z_p = 3.29 and with a standard deviation of 1.7 nm for Figure 5.17(a) the cut-off is 5.6 nm. These peaks are shown in Figure 5.18(a). The remaining background surface is comprised of a series of plateaus at locations corresponding to the outlier peaks and so an interpolation scheme is utilized to fill in the gaps in the surface. Because the height and width of the outlier peaks may vary significantly, the height of each peak is normalized by its maximum and the width of each peak via the standard deviation of the peak in the x- and y-location. The normalized height of a given peak, n, is given by

$$f_n(x) = \frac{f(x)}{f_{max}} \tag{5.18}$$

where f_{max} is the maximum value of the peak.

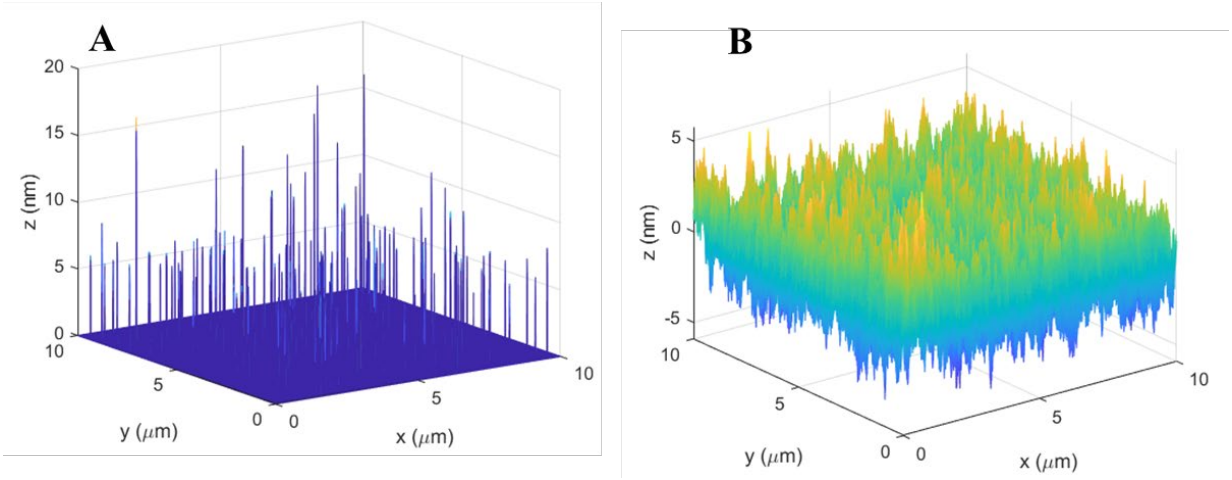

Figure 5.18 (a)Peaks larger than the "cut-off" height on the silica surface. (b)Resulting background noise generated by performing a DFT on the remaining surface.

Then, a DFT is performed on the background surface, with the gaps in the surface filled, and the phase angles comprising the surface are randomly scrambled to generate a new background surface. With the new background surface generated, a random peak and width is selected from the distribution of heights and peaks of the outlier peaks and the average outlier peak is scaled and placed randomly on the surface. This process is repeated until all heights and widths have been selected from the original distributions. Figure 5.19 shows the reconstructed surface with very similar statistics as the original surface; these statistics are summarized in Table 5.1. The skewness is a measure of the asymmetry of the surface height data around the mean (the skewness of a symmetric distribution is zero) and the kurtosis is related to the number and magnitude of the outliers in the surface height data.[112] The statistics between the original and reconstructed surface are very similar which illustrates the robustness of the modified surface reconstruction method.

Table 5.1 RMS roughness, skewness, and kurtosis between the original and reconstructed surface

	RMS Roughness (nm)	Skewness	Kurtosis
Original Surface	1.7	2.2	14.5
Reconstructed Surface	1.7	2.0	16.4

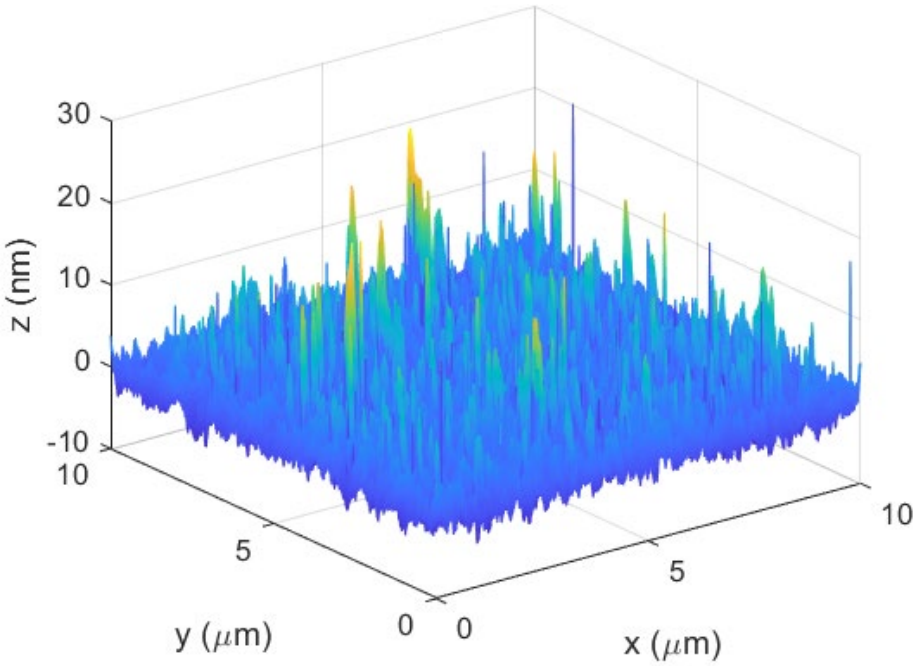

Figure 5.19 A reconstructed surface with statistically similar characteristics as the original AFM surface scan shown in Figure 5.17.

5.7 Reconstructing a Surface Height Function from the Contact Locus

So far, it has been assumed that an AFM surface scan is considered the actual, underlying surface. However, as seen in Chapter 3, the development of a contact locus curve from a surface height function surface calls into question the results of imaging a surface through AFM. Because the tip of an imaging probe has a finite radius (usually on the order of tens of nanometers), and depending on the scale of the surface roughness, some features that exist on the actual, underlying surface may not appear in the image scan. Therefore, a surface scan obtained experimentally through AFM is actually the contact locus of the "true" surface, and not the surface itself. This observation

is evidenced in the contact locus of surface E in Figure 3.2 where the sphere is unable to reach the bottom of the small oscillations and so the contact locus looks almost identical to the contact locus of surface D which does not contain the small scale roughness. While this same phenomenon exists experimentally, though not to the same extent seen computationally from the model surfaces, and since it has been shown that small-scale roughness largely impacts the vdW force and the distribution of deflections at contact for a surface, it is of interest to attempt to reconstruct the actual, underlying surface for an AFM surface scan. Inputting the true surface into the approach-to-contact model should give rise to a more accurate model-predicted d_c-distribution. However, it turns out that for a fine tip probe radius (*e.g.* 10 nm) the distinction between the contact locus and actual, underlying surface is insignificant. Nonetheless, this section seeks to extract the actual, underlying surface from the contact locus and quantitatively determine if any meaningful information is lost between the contact locus and actual surface.

As seen in Figure 2.4(b), when the sphere touches the surface, the line between the sphere's center and point of contact is normal to the surface or perpendicular to the local surface tangent. From the unit normal, $\vec{n}$, the point corresponding to the location of the center of the sphere when in contact with the surface can be determined. This process is repeated for each sphere location along the surface, thus generating a contact locus. Reconstruction of the surface from the contact locus can be done through the opposite procedure. First, for a given point along the contact locus, the angle of the unit normal vector with respect to the horizontal must be determined between the point on the contact locus and point of contact that the sphere makes with the surface. The angle can be estimated by taking the negative inverse of the slope between the point of interest on the contact locus and an adjacent point. Then, the following relationship, with reference to Figure 2.4(b), can be used to determine the contact point that the sphere makes with the surface

$$|\vec{n}| = 1 = \sqrt{(x_{contact} - x_s)^2 + \left(z_{s,contact} - h(x_{contact})\right)^2} \tag{5.19}$$

$$z_{s,contact} - h(x_{contact}) = m(x_{contact} - x_s)$$

Here, m is related to the slope of the normal vector, x_s and $z_{s,contact}$ is the location of the center of the sphere at the contact point, and $x_{contact}$ and $h(x_{contact})$ together determine the location of the contact point on the surface. As there are two solutions to eq 5.19, care must be taken to select the physical one. The process is then repeated for each point along the contact locus to reconstruct the entire surface. Figure 5.20(a) shows a reconstructed surface from a contact locus for the surface height function $h(x/R) = 0.5\sin(\mathrm{x/R})$.

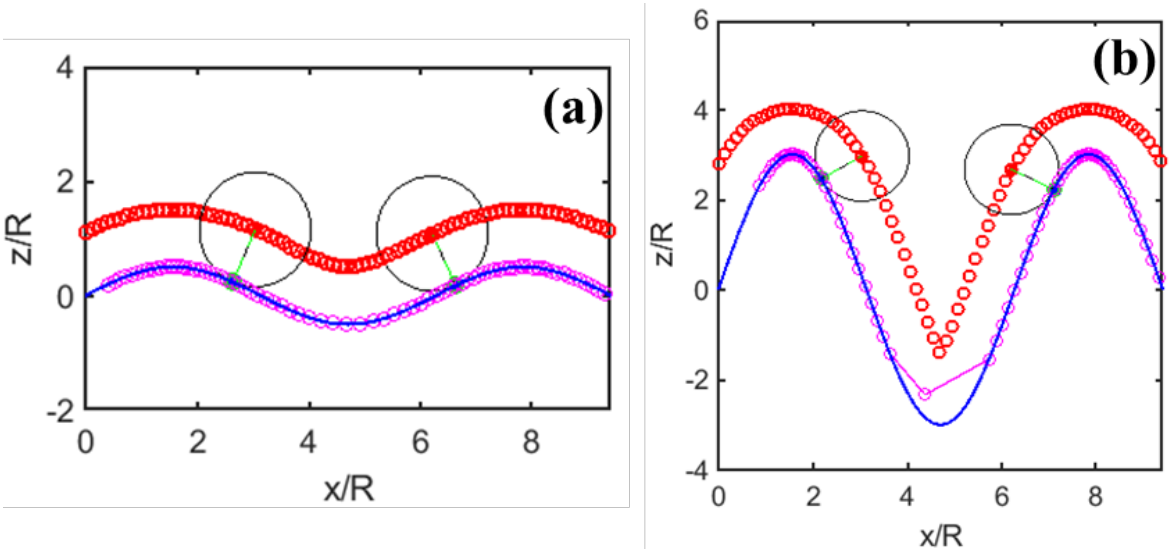

Figure 5.20 The reconstruction of the surface height function (a) $h(x/R) = 0.5\sin(\mathrm{x/R})$ and (b) $h(x/R) = 3\sin(\mathrm{x/R})$. The dashed magenta line is the reconstructed surface, the red circles are points constituting the contact locus, and the blue line is the original surface.

The red circles are the locations of the center of the sphere when the sphere makes contact with the surface, for each x_s. The magenta circles comprise the reconstructed surface and the blue line is the original surface. Also, the dashed green lines are the normal vectors determined from the

procedure outlined above, and the black lines are the original normal vectors obtained by solving for the contact locus from the original surface.

The surface reconstruction procedure works well for surfaces that do not lead to corner points in the contact locus, such as the one shown in Figure 5.20(a). At a corner point the sphere cannot touch the bottom of the surface such as at $x_s = 3\pi/2$ in Figure 3.1(c) for surface C. Because the contact locus is not differentiable at a corner point, the reconstruction method cannot uniquely obtain the true surface around the corner. This consequence is illustrated in Figure 5.20(b), for the surface height function $h(x/R) = 3\sin(\mathrm{x/R})$. The method is able to reconstruct the actual, underlying surface for all points along the contact locus except at $x_s = 3\pi/2$ where the corner point exists. Since the slope between two adjacent points along the contact locus is required to determine the normal vector, the slope cannot be determined accurately at the corner point where it quickly changes (as opposed to all other locations on the contact locus where the slope is roughly constant between adjacent points).

In practice, when performing AFM imaging experiments, the size of the cantilever tip should be made as small as possible in order to mitigate the effect of under sampling portions of the surface. However, since the cantilever tip radius is of a finite size, portions of the actual, underlying surface that are sharper than the radius of the tip can never be sampled. For the surfaces analyzed in this and the next chapter (*e.g.* silica, stainless steel, and sapphire), the RMS roughness is on the same order of magnitude as the size of the surface scan. Therefore, the surface heights appear to vary over several tens of nanometers, and over length scales much greater than the tip radius. Hence, the contact locus that is generated will be negligibly different from the actual, underlying surface. Figure 5.21 illustrates the magnitude of the surface roughness of the surface shown in Figure 5.16 relative to a cantilever tip of radius 1000 nm. While some minor change in

the deflection at contact may result at very specific locations on the surface, the overall shape of the d_c-distribution will remain essentially the same.

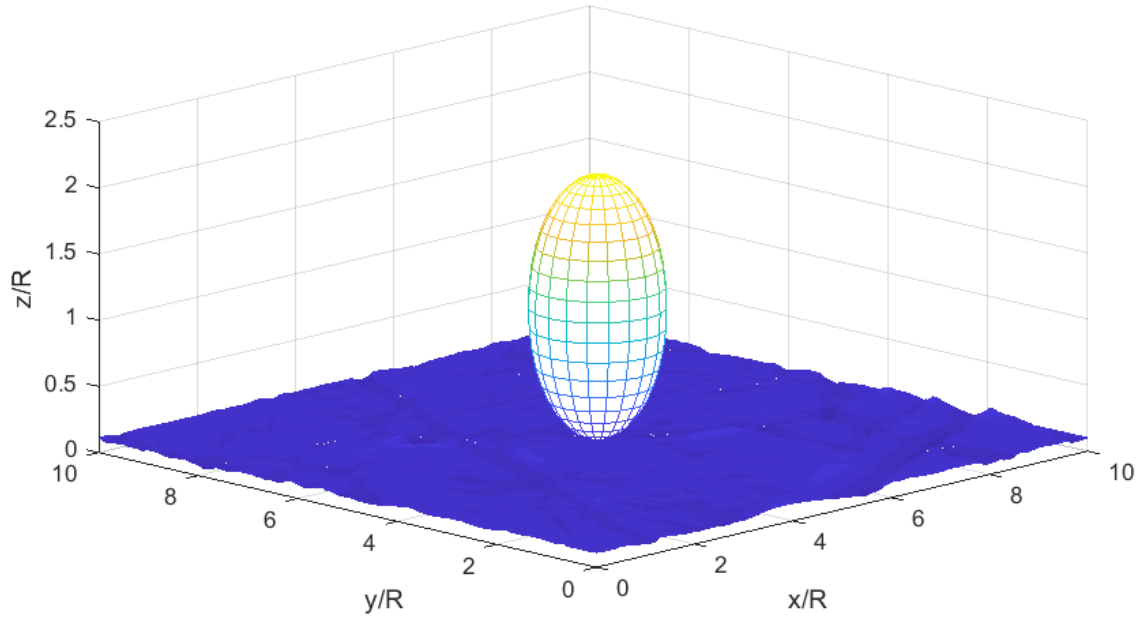

Figure 5.21 The scale of the roughness of the surface shown in Figure 5.16 relative to a sphere of R = 1000 nm.

5.8 Summary

This chapter offered a comprehensive mathematical description of the discrete Fourier transform, including the analysis of amplitude spectra and the effect of varying the phase angle of individual wavelength components on the resulting one-dimensional and two-dimensional surface height functions. Since it is not feasible to image a portion of a substrate using AFM and also obtain force curves along the same exact portion of the surface, DFT can be utilized to transform an experimentally obtained AFM surface height map into the Fourier domain, randomize the phase angles corresponding to each wavelength component, and then generate a representative scan with a similar roughness profile as the original. The DFT method presented herein ensures that the

root-mean-squared (RMS) roughness of each representative surface height map remains constant and matches that of the original surface scan, while also generating surfaces with nearly identical distributions of the various peak heights. Finally, for the surfaces analyzed in this and the next chapter (*e.g.* silica, stainless steel, and sapphire), the RMS roughness is on the same order of magnitude as the size of the surface scan. Therefore, the surface heights appear to vary over several tens of nanometers, and over length scales much greater than the tip radius. Hence, the contact locus that is generated will be negligibly different from the actual, underlying surface. This chapter now sets the stage for the full experimental validation of the approach-to-contact method for which the self Hamaker constant of several materials will be determined with a significant reduction in uncertainty compared to the original approach-to-contact method developed by Fronczak *et al.*[79]

6. EXPERIMENTAL VALIDATION OF THE APPROACH-TO-CONTACT METHOD

6.1 Introduction

Previous chapters have laid the foundation for the development of a modified approach-to-contact method in which the self-Hamaker constant of a substrate can be accurately determined, with a significant reduction in uncertainty, by explicitly accounting for the topography of the given surface. Chapter 4 introduced the concept of relative entropy which provided a quantitative metric to compare two discrete probability distribution functions. The dynamic d_c-distribution was chosen as the reference distribution and various quasi-static distributions were generated for a range of inputted Hamaker constant values, and the relative entropy was minimized to obtain a single A_{eff} value. Moreover, it was found, computationally, that at sufficiently slow cantilever approach speeds (*e.g.* < 200 nm/s), $A_{eff} \cong A_{input}$ such that the quasi-static model provided an accurate description of the behavior of the AFM cantilever tip. Hence, there is no need to invoke the more computationally intensive dynamic model. A discrete Fourier transform method was then proposed in Chapter 5 by which surface height maps of similar roughness profiles were generated from an AFM surface scan. It was found that by varying the individual phase angles contributing to each wavelength component of a surface height map, representative surfaces could be obtained with identical RMS roughness.

This chapter considers a robust experimental validation of the approach-to-contact method for which the self-Hamaker constant of three experimental substrates - amorphous silica, stainless steel, and sapphire - is determined over a range of experimental surfaces with varying topographies. This provides a true test of the approach-to-contact method since surface roughness is taken directly into account, and so the self-Hamaker constant should be constant, with a small

degree of uncertainty due to inevitable experimental error, across each surface of varying topography for a particular experimental substrate. The chosen substrates and experimental surfaces span a range of A_{11} values (65-350 zJ) and RMS roughness (1-25 nm) to ensure a thorough validation. By inputting a range of A_{12}-values, the Hamaker constant is estimated by minimizing the relative entropy between the experimental (*i.e.* the "true" distribution) and model-predicted d_c-distributions, the latter generated from the quasi-static model for a set of cantilever properties. The chosen cantilevers also span a range of nominal radii; two polystyrene colloidal probes of 990 nm and 1800 nm and a silicon nitride probe of effective radius 176 nm. While each colloidal probe/experimental surface pair should lead to a unique experimental d_c-distribution, they should, in theory, yield a similar A_{11} across surfaces comprised of the same substrate material.

This chapter is organized as follows. First, experimental and theoretical methods are discussed including a procedure in which four amorphous silica and stainless steel plates are polished to a "mirror-like" smoothness and then systematically made rougher to produce surfaces that span a range of RMS roughness. AFM force experiments are then completed across each of the plates to generate experimental d_c-distributions unique to the topography of each plate using a silicon nitride cantilever and polystyrene colloidal probes of radius 990 and 1800 nm. AFM surface scans are then obtained and used as input surface height functions to generate corresponding model predicted d_c-distributions, solving the quasi-static model. As previously discussed, since it is not feasible to conduct force and imaging experiments on the same exact portion of a surface, the DFT method introduced in Chapter 5 is used to produce representative surfaces with similar roughness profiles as the original surface scan. The effective Hamaker constant of each plate and ultimately each substrate is then calculated by minimizing the relative entropy between the experimental and model-predicted d_c-distributions for a particular substrate

and plate. Finally, the self-Hamaker constant is determined along with the associated error using error propagation. The A_{11} values were found to be in excellent agreement between plates of the same substrate and the average A_{11} value across all plates for a particular substrate agreed well those found in the literature derived from Lifshitz theory.

6.2 Experimental and Theoretical Methods

6.2.1 Determining the Self-Hamaker Constant for an Experimental Substrate

The general procedure for determining the self-Hamaker constant of an experimental substrate is as follows. Figure 6.1 provides a graphical flowchart describing the method. First, an experimental d_c-distribution is obtained by running AFM force experiments on the experimental substrate (*e.g.* amorphous silica) at 125 different locations for a given cantilever probe (*e.g.* Bruker MSCT-E silicon nitride cantilever) and a cantilever approach speed of 200 nm/s (the rationale for choosing this approach speed is discussed in Chapter 4). Ten AFM surface scans are then obtained by imaging the experimental substrate at different locations using a fine tip cantilever (*e.g.* Bruker RTESPA-300 cantilever). As discussed in Chapter 5, it is not feasible to conduct force and imaging experiments at the same exact location on the experimental substrate and so the DFT method was developed to generate representative surfaces from the original surface scans. In this case, ten representative surfaces were generated for each surface scan, for a total of 100 surface height maps. These surface height maps, along with the experimentally-determined spring constant of the cantilever (and nominal radius), are used to generate model-predicted d_c-distributions for a range of input Hamaker constant values. The relative entropy is then minimized between each model-predicted and experimental d_c-distribution to obtain a set of 100 A_{eff}-values. An average value of A_{eff} is then determined, along with the corresponding error computed using

error propagation (more details on error analysis are given in Section 6.4.1). Finally, from the average value of A_{eff}, the self-Hamaker constant of the experimental substrate can be determined using eq 6.5.

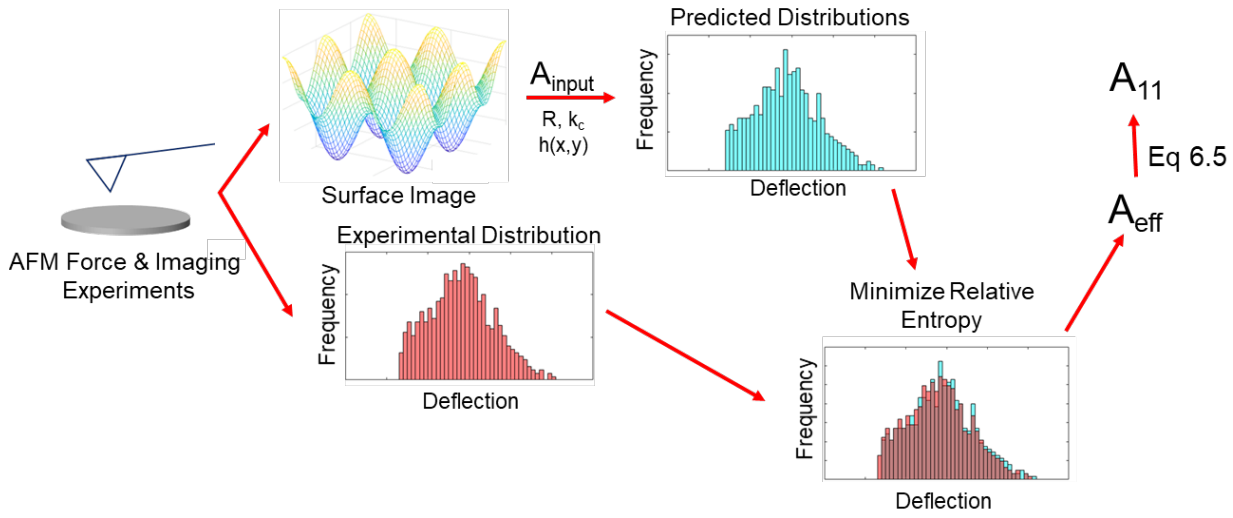

Figure 6.1 Graphical flowchart describing the method for determining the self-Hamaker constant of an experimental material.

6.2.2 Systematic Polishing of Experimental Substrates

Four amorphous silica and stainless steel plates were polished using a Buehler (Lake Bluff, IL) MiniMet 1000 Grinder Polisher. Each plate was first polished using a 0.25 μm (mean particle diameter) Buehler MetaDi diamond suspension to ensure a consistent, mirrorlike finish across each plate. The plates were then systematically made rougher using a range of MetaDi diamond suspensions and pastes with a mean particle diameter between 0.25 and 30 μm to generate a unique roughness profile across each plate. The surface of each plate was then washed with acetone and blown dry using compressed air. Table 6.1 shows the mean particle diameter, in micrometers, of

the diamond suspension/paste used to polish a particular plate. The experimental RMS roughness of each plate was later determined when generating representative surfaces using the DFT method.

Table 6.1 The mean particle diameter (μm) of the diamond suspension/paste used to polish each plate across the amorphous silica and stainless steel substrates.

	Diamond Suspension/Paste Mean Particle Diameter (μm)	
Plate	Amorphous Silica	Stainless Steel
1	1	0.25
2	3	1
3	9	6
4	12	30

6.2.3 Experimental AFM Measurements

A Multimode 8 (Bruker Corporation, Technology Forest, TX) with a Bruker RTESPA-300 probe (nominal values of k_c = 40 N/m and resonance frequency f_o = 300 kHz) was employed in contact mode in air to obtain a set of ten different 10 μm by 10 μm surface height maps of each of the amorphous silica and stainless steel plates, as well as a single sapphire surface (this surface was not polished). Deflection curves (with each complete curve comprised of 64000 data points) were generated with a Bruker MSCT-E silicon nitride probe (nominal values of $R = 10$ nm, k_c = 0.1 N/m, and f_o = 38 kHz) and two polystyrene colloidal probes (NanoAndMore USA Corp, Watsonville, CA) with nominal values of R = 990 ± 99 nm and 1800 ± 180 nm, k_c = 0.1 N/m, and f_o = 38 kHz, interacting with each of the plates and sapphire surface in contact mode with an approach speed of 200 nm/s. The spring constants of the probes were measured experimentally via the thermal tuning method and are provided, with error bars, in Table 6.2.

Table 6.2 Experimental spring constants (reported in N/m) of the three AFM cantilevers

	990 nm Probe	1800 nm Probe	MSCT-E Cantilever
Amorphous Silica	0.1698 ± 0.0002	0.1790 ± 0.0007	0.1931 ± 0.0006
Stainless Steel	0.1687 ± 0.0004	0.1724 ± 0.0016	0.1934 ± 0.0004
Sapphire	0.1702 ± 0.0006	0.1804 ± 0.0007	0.1940 ± 0.0003

The deflection at first contact, d_c, was extracted from each deflection curve following the procedure outlined in ref 79. A total of 125 force measurements were taken at randomly selected and independent locations along the surfaces for each colloidal probe and the MSCT-E cantilever, which were then used to generate the corresponding experimental d_c -distributions. All measurements were taken under dry conditions by passing nitrogen into a humidity-controlled chamber with a relative humidity < 10%. Electrostatic charge was minimized with a Staticmaster Ionizer (Amstat Industries, Inc., Mundelein, IL).

6.3 DFT Representative Images from the AFM Surface Height Scans

As discussed in Chapter 5, it is not feasible to image a portion of a substrate using AFM and also obtain force curves along the same exact portion of the surface. The aforementioned chapter outlined a method for generating representative images from a surface height scan. From the ten independent 10 μm by 10 μm experimental AFM surface scans obtained for each plate across the substrates, ten representative images were generated for a total of 100 images per plate. Figure 6.2 and Figure 6.3 show representative experimental AFM surface scans across each plate for the amorphous silica and stainless steel substrates.

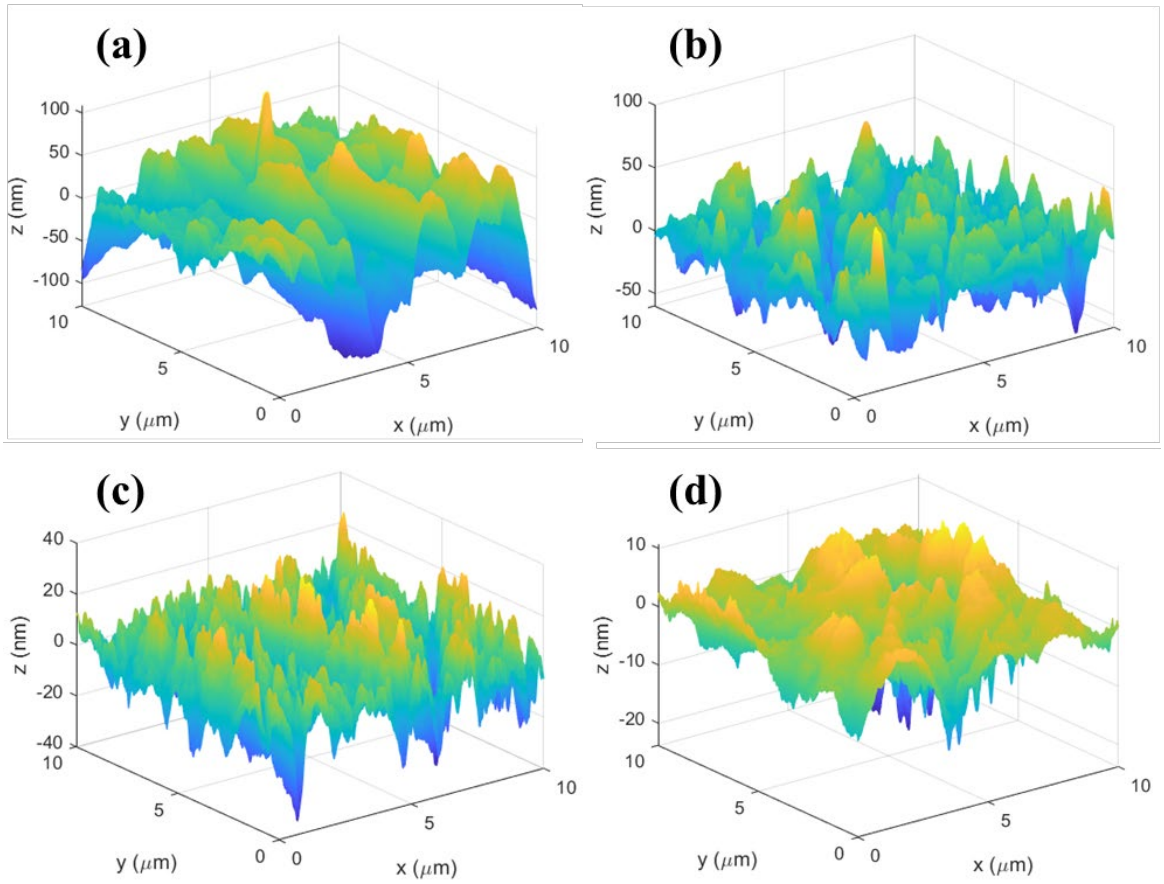

Figure 6.2 Representative 10 by 10 μm experimentally obtained AFM surface scans of an amorphous silica surface, which have an average RMS roughness of (a) 25.9 μm, (b) 16.7 μm, (c) 11.5 μm, (d) 4.6 μm.

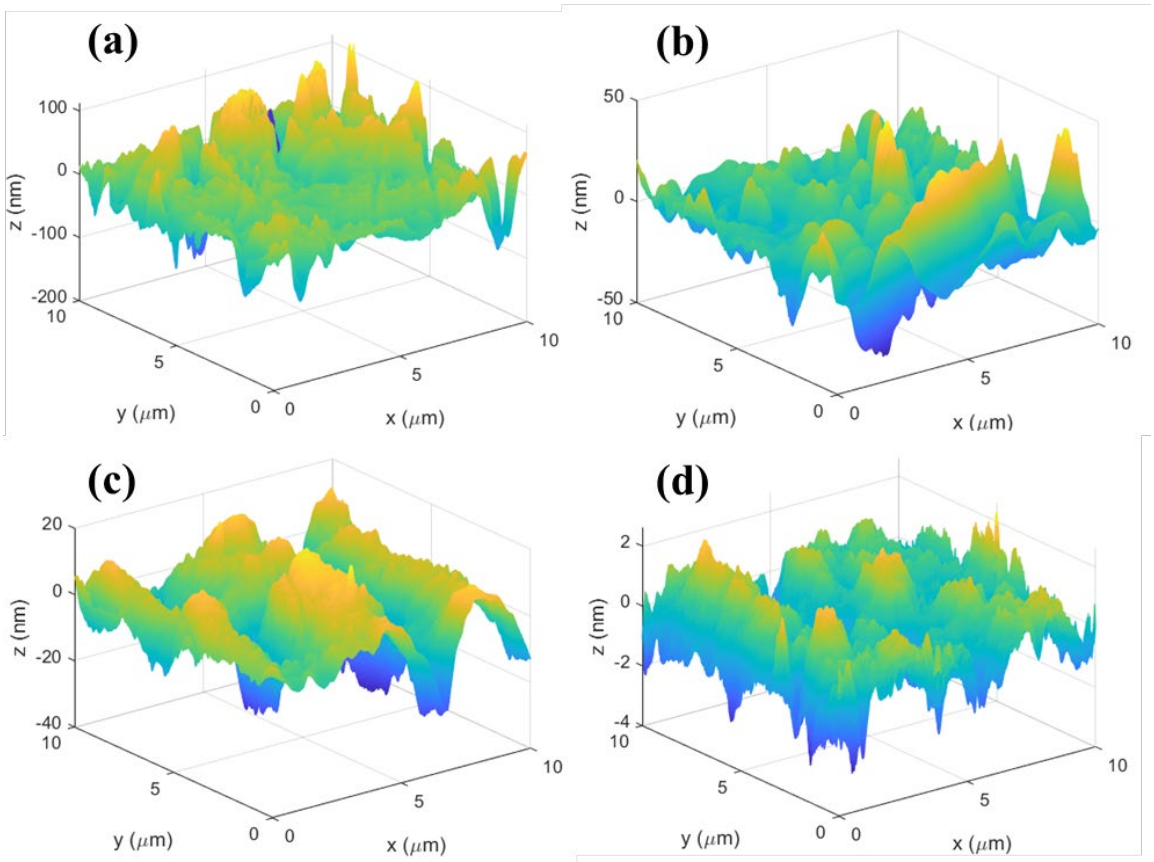

Figure 6.3 Representative 10 by 10 μm experimentally obtained AFM surface scans of a stainless steel surface which have an average RMS roughness of (a) 18.2 μm, (b) 7.2 μm, (c) 5.0 μm, (d) 1.1 μm.

The RMS roughness of each of the ten AFM surface scans for each plate across the amorphous silica and stainless steel substrates was calculated and the average value is given in Table 6.3. The average RMS roughness of the sapphire substrate is 0.4 ± 0.1 nm. Figure 6.4 and Figure 6.5 show corresponding representative DFT reconstructed surface height maps for the AFM surface scans shown in Figure 6.2 and Figure 6.3. The DFT reconstructed surfaces were generated by varying the phase angles of the short wavelength features present on the surface, which for a 10 by 10 μm surface scan comprised of 512 by 512 points, corresponds to long wavelength components greater than approximately 350 nm (see Chapter 5 for a more detailed explanation of

the DFT method). Figure 6.6 shows a (a) representative experimental AFM surface scan of the sapphire surface along with (b) a DFT reconstructed surface.

Table 6.3 Average RMS roughness across ten AFM surface scans for the amorphous silica and stainless steel surfaces.

	Average RMS Roughness (nm)	
Surface	Amorphous Silica	Stainless Steel
1	25.9 ± 17.6	18.2 ± 6.7
2	16.7 ± 3.4	7.2 ± 1.4
3	11.5 ± 3.8	5.0 ± 2.5
4	4.6 ± 1.5	1.1 ± 0.6

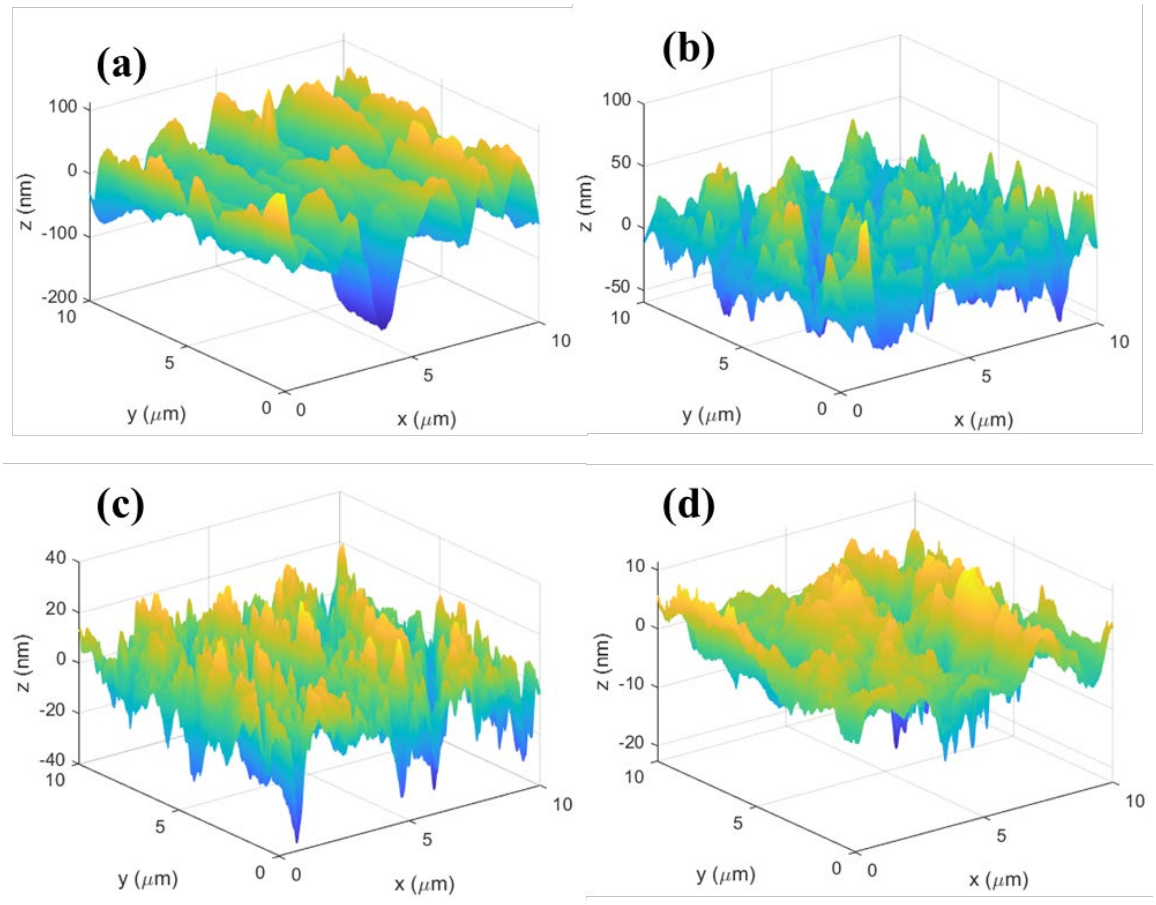

Figure 6.4 Representative 10 by 10 μm reconstructed surfaces obtained using the DFT method corresponding to the amorphous silica AFM surface height scans shown in Figure 6.2. The RMS roughness of each reconstructed surface is identical to the original surface scan.

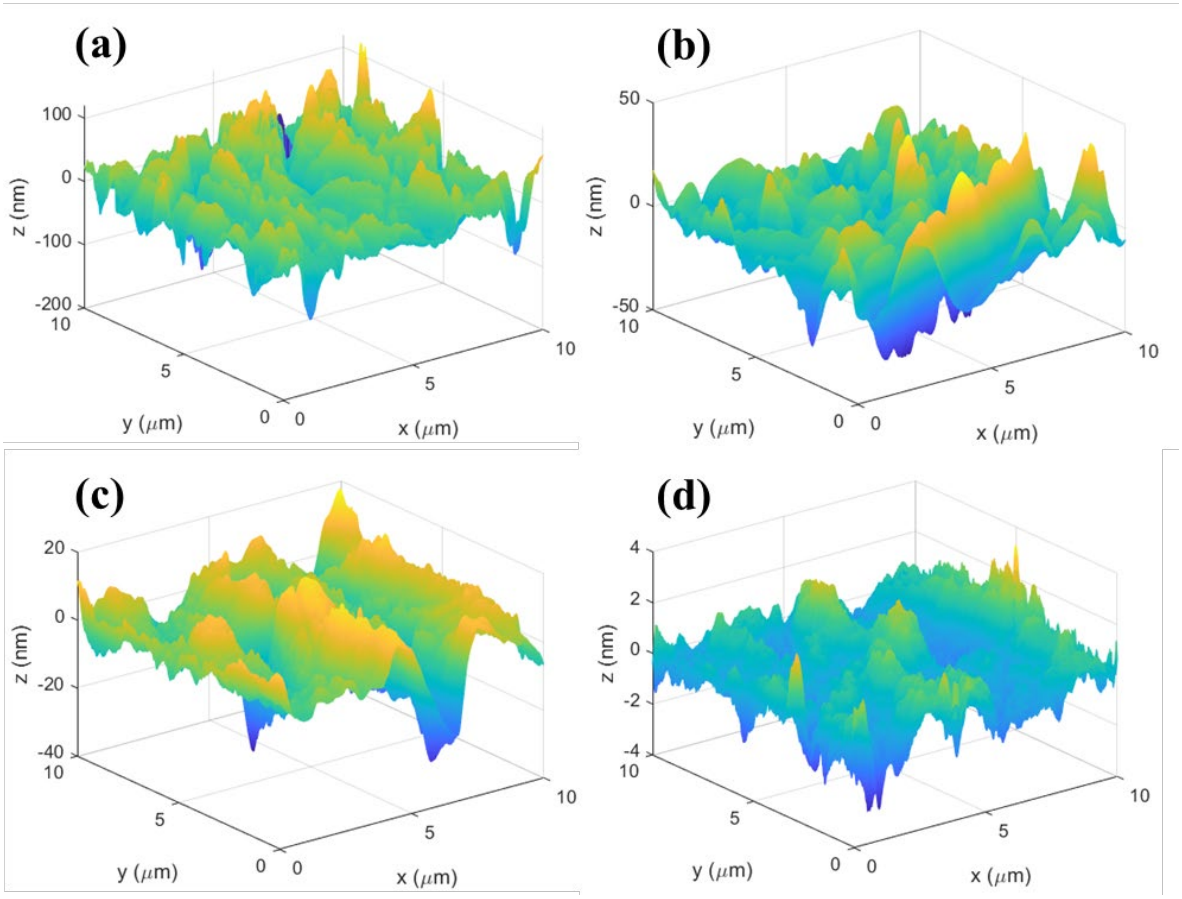

Figure 6.5 Representative 10 by 10 μm reconstructed surfaces obtained using the DFT method corresponding to the stainless steel AFM surface height scans shown in Figure 6.3. The RMS roughness of each reconstructed surface is identical to the original surface scan.

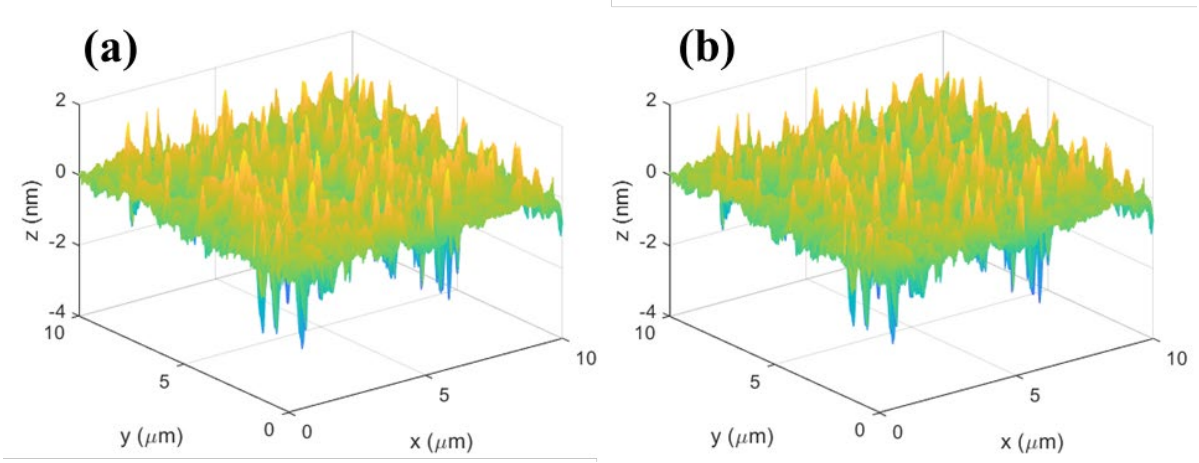

Figure 6.6 (a) A representative 10 by 10 μm experimentally obtained AFM scan of a sapphire surface which has an overall average RMS of 0.4 nm across all 10 surface scans. (b) A reconstructed image of the surface shown in (a) obtained with the discrete Fourier transform method.

All of the amorphous silica and stainless steel AFM image scans exhibit a similar surface feature which appear as long grooves in the surface that result from polishing. These grooves remain fairly intact after generating the representative images because the DFT method preserves the longer wavelength features on the surface while scrambling the smaller wavelength/higher frequency background noise. The sapphire surface exhibits numerous "large" peaks and valleys extending from the mean plane of the surface which are more uniformly distributed. As such, the reconstructed surface looks very similar to the original surface scan because the average amplitude of the background noise (*e.g.* the high frequency/low wavelength components) is very small in comparison to the scale of the larger peaks on the surface.

6.4 Results and Discussion

6.4.1 Calculating the Effective Hamaker Constant for an Experimental Substrate

For each DFT reconstructed image, and for a chosen probe radius, quasi-static model predicted d_c-distributions were obtained for a range of A_{input} values. Due to the uncertainty in the actual radius of a colloidal probe, quasi-static predicted distributions were generated for radii of 891, 990 and 1089 nm, or for radii of 1620, 1800 and 1980 nm. For a given colloidal probe, and for each corresponding radius, 100 separate values of A_{eff} were then determined, and then averaged. The three results (lower, nominal and upper bound) were subsequently averaged to yield a final value of A_{eff} for a given (nominal) probe radius. The minimum value of the relative entropy between the experimental and quasi-static distributions was identified, yielding an estimate of A_{eff} for the given reconstructed image.

In some cases, such as shown in Figure 6.7, a plot of the relative entropy versus A_{input} yields a clear minimum value therefore leading to a single value of A_{eff}. However, instances arise

in which a clear minimum is not apparent, as shown in Figure 6.8, such that choosing a singular value of A_{eff} is difficult. Therefore, a cutoff value of 0.02 greater than the global minimum value for the relative entropy was selected such that all A_{input} values corresponding to these relative entropy values at or below the cutoff were selected as possible values of A_{eff}. The 0.02 cutoff value was chosen based on a separation computation of the relative sum of squares error (SSE) between the experimental and quasi-static distributions. It was found that a 0.02 change in the relative entropy is analogous to approximately a 5% change in the relative SSE between distributions which is a comparatively small difference. Regardless of the chosen value of the cutoff, the minimum and maximum A_{input} values are considered when determining the overall value of A_{eff} to provide a reasonable estimate of the error. From this subset of A_{input} values, the minimum, maximum, and average value were selected, and the corresponding uncertainties computed as follows. For example, in Figure 6.7(a), $A_{min} = 66.5$ zJ and $A_{max} = 67.5$ zJ and in Figure 6.8(a), $A_{min} = 70.1$ zJ and $A_{max} = 71.9$ zJ.

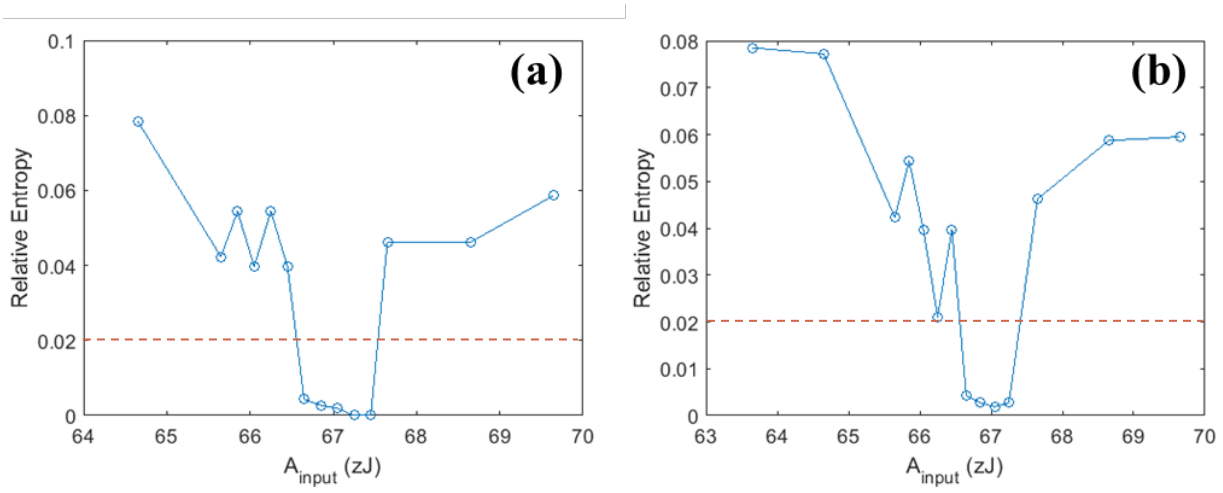

Figure 6.7 Representative plots of the relative entropy versus inputted Hamaker constant, A_{input}, for the (a) 990 nm and (b) 1800 nm colloidal probes. In both cases, a clear minimum value of the relative entropy exists for a specific A_{input}.

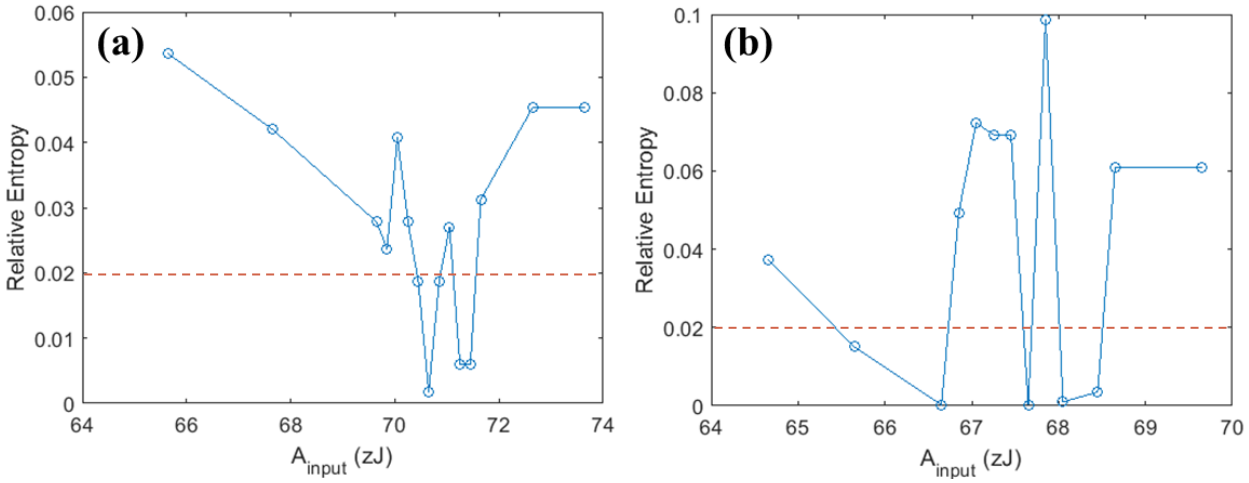

Figure 6.8 Representative plots of the relative entropy versus inputted Hamaker constant, A_{input}, for the (a) 990 nm and (b) 1800 nm colloidal probes. In this case, a clear minimum value of the relative entropy is not obvious leading to the establishment of a cutoff value of 0.02.

For each of the four plates of different RMS roughness for the amorphous silica and stainless steel substrates, ten AFM image scans were taken and for each scan, ten reconstructed surfaces were generated via the DFT method presented in Chapter 5, for a total of 100 reconstructed surfaces per plate. For each reconstructed surface, a range of possible A_{eff} values was determined based on the 0.02 cutoff value for the relative entropy; this range was given by an A_{min} and an A_{max} for a particular reconstructed surface. For example, in Figure 6.7(a) $A_{min} =$ 66.5 zJ and $A_{max} = 67.5$ zJ. Thus, for a given AFM image scan, there were 100 different values of A_{min} and A_{max} that were determined. Then the average of these values, or $A_{min,avg}$ and $A_{max,avg}$ were determined by

$$A_{min,avg} = \frac{1}{N}\sum_{i=1}^{N} A_{min,i}$$
$$A_{max,avg} = \frac{1}{N}\sum_{i=1}^{N} A_{max,i} \quad (6.1)$$

where N = 100 and i is a reconstructed surface. The average uncertainties for a given $A_{min,i}$ and $A_{max,i}$ were then computed by

$$\Delta A_{min} = \sqrt{\frac{1}{N-1}\sum_{i=1}^{N}\left(A_{min,i} - A_{min,avg}\right)^2}$$
$$\Delta A_{max} = \sqrt{\frac{1}{N-1}\sum_{i=1}^{N}\left(A_{max,i} - A_{max,avg}\right)^2} \quad (6.2)$$

Finally, the uncertainties in the above average values were calculated by

$$\Delta A_{min,avg} = \frac{\Delta A_{min}}{\sqrt{N}}$$
$$\Delta A_{max,avg} = \frac{\Delta A_{max}}{\sqrt{N}} \quad (6.3)$$

Thus, for a given image scan, $A_{min} = A_{min,avg} \pm \alpha\Delta A_{min,avg}$ and $A_{max} = A_{max,avg} \pm \alpha\Delta A_{max,avg}$, where α is the Gaussian distribution quantile value corresponding to a confidence interval (*e.g.* 90% or 95%). The average of the two limits was then determined, along with the proper propagation of error, to get the estimated value of A with error for a particular image scan. This procedure was then repeated for each image scan, and each value of A was then averaged to obtain a final estimate of A with the final error for a particular plate. An example calculation of determining A_{eff}, with the proper propagation of error, is as follows for plate 1 using the 990 nm colloidal probe on the amorphous silica surface. For the lower, nominal, and upper values of the colloidal probe radius (891, 990, 1089 nm), A_{min} and A_{max} = 66.5 ± 0.2, 71.7 ± 0.3, 67.2 ± 0.3, 71.6 ± 0.3, and 67.5 ± 0.3, 71.4 ± 0.3 zJ, respectively. The average values of A_{min} and A_{max} are 69.1, 69.4, and 69.5 zJ, respectively. The overall average, or A_{eff} is therefore 69.3 zJ. The overall

error in A_{eff} is computed from the individual errors from the six A_{min} and A_{max} values, or, in general, by

$$\sigma_{A_{eff}}^2 = \sum_{i=1}^{N} \frac{1}{N^2} \sigma_A^2 \tag{6.4}$$

In this case, N = 6 and σ_A^2 corresponds to the individual error for a particular A_{min} or A_{max}. Therefore, the error in A_{eff} is 0.1 zJ or 0.2 zJ for the 90% confidence interval (α = 1.64), and so A_{eff} = 69.3 $\pm$ 0.2 zJ for plate 1 using the 990 nm colloidal probe on the amorphous silica surface. The remaining A_{eff} were similarly calculated and the error propagated in the average values using eq 6.4.

6.4.2 Quantifying the Effective Radius of Curvature of the MSCT-E Cantilever Tip

The model developed in this work considers a perfectly spherical tip while the actual shape of the MSCT-E cantilever is not necessarily spherical. Hence, an effective radius of the cantilever must be determined. Following refs 79 and 80, an effective radius, R_{eff}, of the MSCT-E cantilever was determined by minimizing the relative entropy between the experimental d_c-distribution and aggregate model-predicted distribution from each of the experimental substrates generated using the MSCT-E cantilever. R_{eff} is not required to correspond to the actual radius of curvature of the AFM tip, but approximates the average vdW force between the tip, regardless of shape, and surface.[101]

Following the aforementioned procedure for determining the effective Hamaker constant, a similar process was done to determine R_{eff}. For each AFM surface scan across the three substrates, quasi-static model predicted d_c -distributions were obtained for a range of R_{input} values. In this case, since R is an output parameter, a value of A was required to generate

the model-predicted distributions. As such, A was selected to be 108 zJ, 251 zJ, and 165 zJ for amorphous silica, stainless steel, and sapphire, respectively. These values were calculated using eq 1.4 and for literature established values of A_{11} for the three surfaces and A_{22} for the silicon nitride probe (since the self-Hamaker constant for stainless steel is reported as range of values from 200-500 zJ, 350 zJ was used). Model-predicted d_c-distributions were then generated for each plate across the three substrates and range of R_{input} values using the same set of 100 surfaces as described above. The upper and lower bounds of R_{input} were determined, along with the average value, below the relative entropy cut-off threshold of 0.02 (the relative entropy was minimized between the experimental and model-predicted d_c-distributions across each plate and substrate). Values of R_{eff} across each substrate are summarized in Table 6.4.

Table 6.4 The minimum, maximum and average values of the effective radius, R_{eff}, across the three experimental substrates.

	$R_{eff,min}$	$R_{eff,max}$	$R_{eff,avg}$
Amorphous Silica	176.8 ± 1.4	179.6 ± 1.6	174.5 ± 2.1
Stainless Steel	176.6 ± 1.2	180.4 ± 1.3	176.6 ± 1.8
Sapphire	175.6 ± 0.2	176.6 ± 0.2	175.6 ± 0.3

Table 6.4 shows that the effective radius values are very similar across each of the substrates which validates this calibration procedure. Upon the final averaging of each $R_{eff,avg}$ across the three substrates, $R_{eff} = 176.3 \pm 1.5$ (90% confidence interval). Similarly to the colloidal probes, the effective Hamaker constant using the MSCT-E probe was determined using a radius of 174.8, 176.3, and 177.8 nm across the three substrates.

6.4.3 Determining the Self-Hamaker Constant of Amorphous Silica, Stainless Steel, and Sapphire

Tables 6.5 and 6.6 show average values of A_{eff} along with corresponding error for each cantilever across the four amorphous silica and stainless steel plates. Despite the varying degrees of roughness between the plates, the average values of A_{eff} show excellent agreement which suggests that the new vdW force model, and in turn, the modified approach-to-contact method properly accounts for surface topography in that roughness effects are captured by the model-predicted distribution of deflections at contact. Furthermore, these results support the conclusion reached in Chapter 4 that the quasi-static model sufficiently describes the behavior of the AFM cantilever at reasonably slow (*e.g.* 200 nm/s) approach speeds.

Table 6.5 Average values of A_{eff} for each cantilever tip across the four amorphous silica surfaces of varying roughness profiles (90% confidence interval reported)

	990 nm Probe	1800 nm Probe	MSCT-E Cantilever
Plate 1	69.3 ± 0.2	69.9 ± 0.2	107.4 ± 0.5
Plate 2	69.3 ± 0.2	70.0 ± 0.2	113.6 ± 0.4
Plate 3	67.9 ± 0.2	69.8 ± 0.2	117.4 ± 0.1
Plate 4	69.1 ± 0.2	69.0 ± 0.2	114.2 ± 0.3
Average	68.9 ± 0.3	69.7 ± 0.4	112.8 ± 0.3

Table 6.6 Average values of A_{eff} for each cantilever tip across the four stainless steel surfaces of varying roughness profiles (90% confidence interval reported)

	990 nm Probe	1800 nm Probe	MSCT-E Cantilever
Plate 1	163.1 ± 0.4	162.7 ± 0.2	244.9 ± 0.4
Plate 2	162.0 ± 0.4	162.8 ± 0.2	243.8 ± 0.4
Plate 3	162.1 ± 0.3	162.3 ± 0.3	247.2 ± 0.4
Plate 4	162.6 ± 0.3	162.6 ± 0.3	247.1 ± 0.2
Average	162.5 ± 0.6	162.6 ± 0.4	245.8 ± 0.3

In addition to the results shown in Table 6.5 and Table 6.6, the average values of A_{eff} for each cantilever for the sapphire substrate are 105.5 ± 0.6 zJ, 110.9 ± 0.2 zJ, and 163.1 ± 0.4 zJ

(90% confidence interval) for the 990 and 1800 nm colloidal probes and the MSCT-E cantilever, respectively. (The values of A_{eff} are larger for the MSCT-E cantilever since A_{eff} describes the interaction between two materials and the MSCT-E cantilever is comprised of silicon nitride while the colloidal probes are polystyrene. Hence, A_{22} is a different value and therefore A_{eff}.)

Figure 6.9 shows a representative comparison between the experimental and aggregated quasi-static model predicted d_c-distributions, the latter obtained using the above values of A_{eff} for the (a) 990 and (b) 1800 nm colloidal probes for the amorphous silica substrate. (A given quasi-static distribution is the average of the separate distributions each obtained from the 100 different reconstructed images.) The agreement between these two distributions is very good. Overall, the average deflection and range of deflections between the model-predicted and experimental data is very similar (in addition to the shape of the distributions). Figure 6.10 shows similar results for the stainless steel substrate and Figure 6.11 shows a representative comparison between model-predicted and experimental distributions for the two substrates and MSCT-E cantilever.

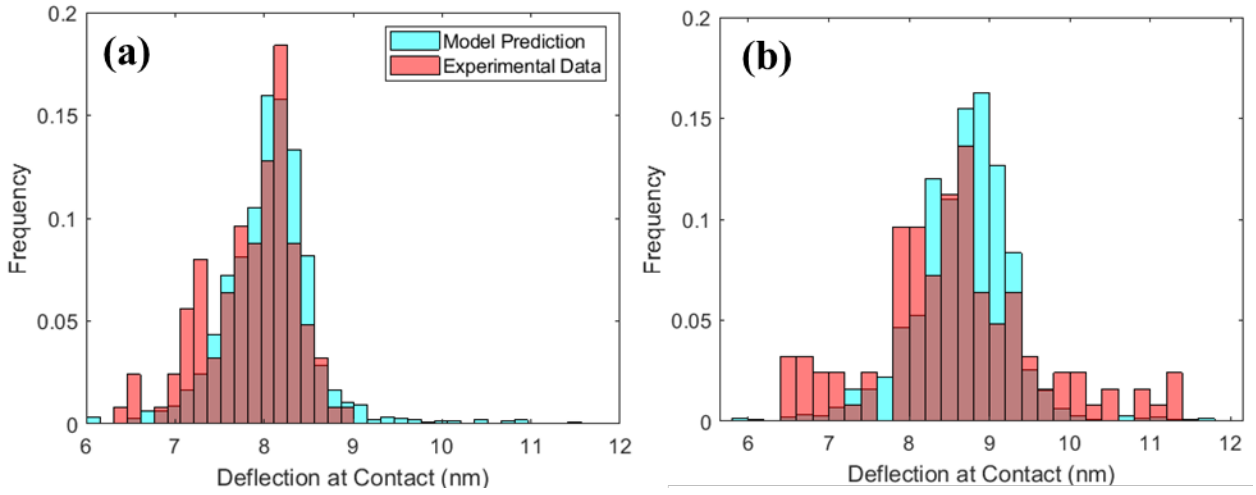

Figure 6.9 Comparison of AFM experimentally obtained (red) and aggregate model predicted (blue) d_c-distributions for an amorphous silica substrate using a (a) 990 nm and (b) 1800 nm colloidal probe. The model predicted distributions are generated using experimentally determined spring constants for each probe and the average A_{eff} minimizing the relative entropy across a range of A_{input} values.

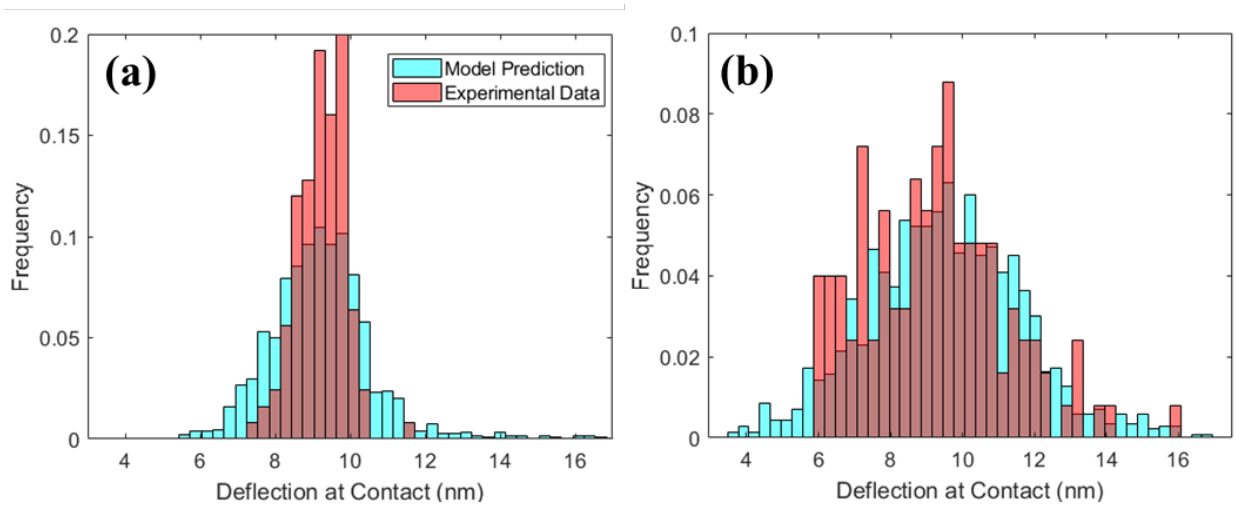

Figure 6.10 Comparison of AFM experimentally obtained (red) and aggregate model predicted (blue) d_c-distributions for a stainless steel substrate using a (a) 990 nm and (b) 1800 nm colloidal probe. The model predicted distributions are generated using experimentally determined spring constants for each probe and the average A_{eff} minimizing the relative entropy across a range of A_{input} values.

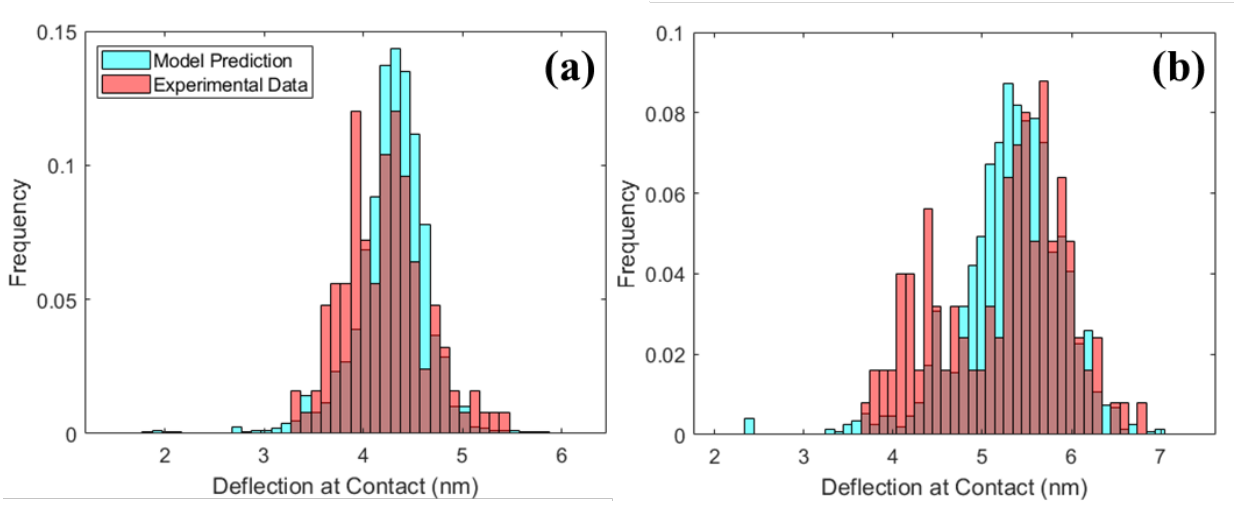

Figure 6.11 Comparison of AFM experimentally obtained (red) and aggregate model predicted (blue) d_c-distributions using the MSCT-E cantilever for the (a) amorphous silica and (b) stainless steel substrates. The model predicted distributions are generated using the experimentally determined spring constant for the cantilever and average value of the effective radius.

Using the obtained average value of A_{eff}, or A_{12}, the self-Hamaker constant, A_{11}, of each substrate was calculated from[38]

$$A_{11} \approx (A_{12})^2/A_{22} \tag{6.5}$$

where A_{22} for the polystyrene colloidal probes was found to be 71 zJ[45] or 79 zJ[41] and 180 zJ for the silicon nitride probe[40]. These literature values were derived using Lifshitz theory and are not provided with error bars (*e.g.* $\sigma_{A_{22}} = 0$). Table 6.7 gives the average value of A_{11} across each cantilever tip and substrate along with error computed using error propagation based on eq 6.5.

Table 6.7 Average values of A_{11} for each cantilever across the three experimental substrates (90% confidence interval reported)

	990 nm Probe		1800 nm Probe		MSCT-E
	A_{12} = 79 zJ	A_{12} = 71 zJ	A_{12} = 79 zJ	A_{12} = 71 zJ	A_{12} = 180 zJ
Silica	60.1 $\pm$ 0.6	66.8 $\pm$ 0.7	61.4 $\pm$ 0.7	68.3 $\pm$ 0.8	70.7 $\pm$ 0.4
Stainless Steel	334.0 $\pm$ 2.5	371.7 $\pm$ 2.8	334.7 $\pm$ 1.8	372.5 $\pm$ 2.0	335.4 $\pm$ 0.9
Sapphire	140.9 $\pm$ 1.5	156.8 $\pm$ 1.7	155.5 $\pm$ 0.7	173.1 $\pm$ 0.7	147.8 $\pm$ 0.7

Upon further averaging of each of the five A_{11}values for each substrate as well as determining the error in each value using error propagation, a final estimate of A_{11} for the silica, stainless steel, and sapphire substrates was 65.5 ± 0.3 zJ, 349.7 ± 1.0 zJ, and 154.8 ± 0.5 zJ which all agree very well with the literature established values of 65[40] and 66 zJ[43] for silica, 200-500 zJ for stainless steel[25], and 150[25] or 152[40] for sapphire.

The uncertainty in the obtained estimate of A_{11} has also been significantly reduced compared to a previous approach-to-contact method[79,80] because of the use of the complete d_c-distribution and the specific surface geometry of the substrate. In this prior method, the surface was modeled using the flat plate surface geometry, which as noted before yields a single value of d_c for any approach speed (*i.e.*, the d_c-distribution resembles a delta function). Along with eq 1.5,

this approach results in the self-Hamaker constant A_{11} being proportional to the sixth power of d_c, or $A_{11} \propto d_c^6$. But as AFM experiments invariably yield a distribution of d_c-values (because of the inherent roughness of the surface), an estimate of A_{11} was obtained by the use of the average value of d_c. The resulting uncertainty in A_{11} was then generated using propagation of error, which indicates that the relative error in the estimate of A_{11} is 6 times that of d_c, or $\delta A_{11}/A_{11} = 6\,\delta d_c/d_c$ (where δA_{11} and δd_c are the assigned uncertainties to the corresponding parameters). Hence, even moderate uncertainties in d_c give rise to somewhat large uncertainties in A_{11}. For example, the average experimental value of d_c from Figure 6.9(a) is 8.0 nm with a standard deviation of 0.58 nm. If one standard deviation is used as an estimate of the uncertainty, then this modest relative error in d_c of 7.25% leads to the sizeable relative error of 43.5% in A_{11}. (The final uncertainties will of course be even larger if more than one standard deviation is used.)

The new method, with its utilization of the full d_c-distribution, lessens the impact of error propagation when at least determining A_{eff}. In particular, the relatively sharp minimum found with the relative entropy directly results in a rather small uncertainty in A_{eff}. For example, one of the main sources of uncertainty in the analysis is the 10% error in the reported radius of the polystyrene probe. Yet, this error ultimately yields uncertainties that are much less than the error reported from the sphere radius. (The other main source of error results from the two different reported values of A_{22}.) The use of the model predicted quasi-static distributions should also give rise to additional errors, as a result of having to generate various representative surface height maps (instead of being able to directly image the surface where the d_c-distributions are experimentally obtained). But these errors, including other unavoidable experimental errors, should be relatively small, at least compared to the two main sources of uncertainty mentioned above.

6.5 Summary

This chapter provided a comprehensive experimental validation of the modified approach-to-contact method in which the self-Hamaker constant of three experimental substrates was determined to be in excellent agreement with prior predictions and with an associated uncertainty that was significantly reduced compared to the previous approach-to-contact method developed by Fronczak *et al.*[79,80] The consistency in A_{eff} between plates for a particular substrate is a key result because it shows that surface roughness has been properly considered in the development of the modified approach-to-contact method. Furthermore, the chosen substrates spanned a range of self-Hamaker constant values which further justifies the applicability of the method for a range of solid materials without the need to modify their surfaces before performing force or imaging experiments. This work shows promise in providing a reliable means of determining the self-Hamaker constant across a broad range of solid materials and applications.

7. CONCLUSIONS AND FUTURE WORK

Particle adhesion occurs due to the presence of intermolecular forces between molecules; vdW forces are of particular interest because they are always present in a system. The strength of the vdW force between a pair of interacting materials is quantified by the Hamaker constant, and this work was concerned with the development of an AFM-based method for determining A across a variety of solid materials. The Hamaker constant can be estimated from several portions of the AFM deflection curve, including the pull-off and approach-to-contact regions. In the approach-to-contact region, which is the focus of this work, the behavior of the AFM cantilever tip is assumed to be quasi-static such that the cantilever is taken to be in mechanical equilibrium at each instant during its approach to the surface. Beyond a critical tip-surface separation distance, however, mechanical equilibrium cannot be maintained, and the tip immediately jumps into contact with the surface; the magnitude of this jump can therefore be related to the Hamaker constant.

Fronczak *et al.*[79,80] developed an approach-to-contact method relating A to the deflection of the tip at first contact with the surface, d_c. While d_c is well defined experimentally, it is dependent on the approach speed. For a sufficiently slow approach speed (*e.g.* 200 nm/s or less) and treating the cantilever as a sphere with effective radius R_{eff}, the self-Hamaker constant may be found using eq 1.7. While preliminary estimates of A_{12} for several solid materials (*e.g.* amorphous silica) were found to be in good agreement with predictions of the Lifshitz approximation, even for the nominally smooth surfaces studied, a distribution of d_c-values was reported. However, the error in the experimentally-determined average value of d_c was greatly propagated in the calculation of the self-Hamaker constants. As such, inherent surface roughness

is the primary reason for the emergence of the broad distribution of deflections at contact, or d_c-distribution. As shown in Chapter 6, the range in d_c-values comprising a d_c-distribution can be quite broad. Therefore, obtaining only a single, average value of d_c from a single set of AFM force experiments is not sufficient as the entire distribution of values must be considered. Therefore, given that the resulting d_c-distribution should be directly influenced by the inherent surface roughness, key improvements to the approach-to-contact AFM method developed by Fronczak *et al.*[79,80] were obtained by explicitly accounting for the topography of the given surface. Moreover, the incorporation of surface roughness into the method, via the direct connection of A to a given surface's characteristic d_c-distribution, lead to more accurate estimates of the Hamaker constant with a significant reduction in their uncertainties.

The development of the modified approach-to-contact method first began with the derivation of a new expression describing the vdW force between an AFM cantilever tip and surface of arbitrary roughness. Corresponding critical point conditions were then derived under the quasi-static assumption to determine d_c along any point on a surface. Because of surface roughness, different values of d_c are obtained as the tip accesses spatially separate surface positions and as the tip attempts to access the same surface position but cannot do so exactly due to the inevitable horizontal drift of the cantilever. Consequently, a characteristic d_c-distribution was observed for a given surface and chosen cantilever properties, providing a signature of the underlying surface roughness. A thorough study was completed to understand the effects of surface geometry on the resulting d_c-distributions, in the quasi-static limit, for numerous surface height functions. Contact loci (one-dimensional) and contact mesh plots (two-dimensional) were obtained illustrating the position of the sphere when in contact with the surface. The presence of

small-scale roughness serves to vary the amount of substrate material that is close to sphere and therefore influences the magnitude of the vdW force and ultimately d_c.

A model describing the dynamic behavior of the cantilever as it approaches and interacts with an arbitrary surface was then developed. When the cantilever interacts with a perfectly flat plate, the resulting ratio of d_c to its value in the quasi-state limit, $d_{c,qs}$, approaches unity as the cantilever approach speed decreases. This trend was due to the following reasons. First, the speed of the tip, however large it may become just before the tip contacts the surface, remains finite (in contrast to the tip immediately jumping to the surface upon reaching the critical point in the quasi-static model). Second, the platform is in constant motion (in contrast to the fixed location of the platform once the critical point is reached in the quasi-static model). Hence, d_c for the dynamic model was less than $d_{c,qs}$.

A similar conclusion held for more complicated surfaces for which a comparison was made between d_c-distributions obtained using the dynamic model versus the quasi-static limit. The relative entropy was computed between the two distributions to provide a quantitatively meaningful analysis on the importance of inertial effects. For a range of different inputted values of the Hamaker constant, or A_{input}, an effective Hamaker constant, A_{eff}, was determined by minimizing the relative entropy between the dynamic and quasi-static d_c-distributions. For sufficiently slow approach speeds, for which A_{eff}/A is close enough to one, the quasi-static model provided an accurate description of the behavior of the AFM cantilever tip. Hence, there is no need to invoke the more computationally intensive dynamic model. In other words, at these approach speeds, inertial effects in an AFM experiment should be essentially unobservable.

A method utilizing the discrete Fourier transform was then developed to generate representative surfaces from an existing AFM surface height map while maintaining similar

roughness statistics. The need for this DFT method arose from the limitation that AFM force measurements and imaging could not be completed along the same exact portion of a substrate since the modified approach-to-contact method requires a comparison between model-predicted and experimental d_c-distributions. Two variations of the surface reconstruction method were derived; one in which the range in surface variations was small (*e.g.* for relatively smooth surfaces) and one for surfaces containing many large peaks extending greatly beyond the average variations in the surface. It was found that in both cases, the resulting statistics describing the surface such as RMS roughness, skewness, and kurtosis, agreed very well between the original and reconstructed surfaces. Finally, a study revealed that while the surface map obtained through AFM imaging was actually the contact mesh of the underlying surface, for a fine tip probe radius (*e.g.* 10 nm), the distinction between the contact mesh and actual surface was insignificant for the experimental substrates considered in this work.

Finally, a robust experimental validation of the modified approach-to-contact method was completed for which the self-Hamaker constant of amorphous silica, stainless steel, and sapphire was determined. It was found that the self-Hamaker constant values were consistent between sample plates of varying surface topography (and RMS roughness) across each material. This consistency is a key result because it shows that surface roughness has been properly considered in the development of the modified approach-to-contact method. Furthermore, the average self-Hamaker constant values across the three materials were in excellent agreement with Lifshitz determined values. Overall, the novel approach-to-contact method developed herein provides a reliable means of determining the self-Hamaker constant across a broad range of solid materials.

There are several aspects of the modified approach-to-contact method developed in this work that could be further considered. First, while the method is valid for determining the

Hamaker constant of materials in air, it would be worthwhile to consider an extension to fluid environments. There are several systems of interest in which vdW interactions occur across an intervening liquid medium, and for which accurate knowledge of these corresponding Hamaker constants is important (*e.g.* aggregation of colloidal particles in aqueous dispersion[113–115], structural investigations of living cells[116–118], and physical properties of pharmaceutical products in solution[119,120]). The extension of the method to such systems would be worthwhile, where the cantilever tip moving toward the substrate would now also experience hydrodynamic forces from the intervening medium. Hydrodynamic effects may remain consequential over a broad range of cantilever approach speeds, such that the quasi-static model only becomes a valid description of the cantilever behavior at very low (and impractical) approach speeds.

These non-equilibrium viscous interactions do not affect the quasi-static behavior of the cantilever tip but would have to be included in the dynamic analysis of the tip motion. For the fluid environments considered here, the Reynolds number would most likely be low such that motion of the cantilever could be described by the Stokes flow regime.[121,122] Equations describing Stokes flow (*e.g.* a momentum balance) would need to be derived from the Navier-Stokes equations and included as additional terms in the dynamic model.[121,122] Experiments would need to be carried out in an AFM fluid cell, and a potential starting point would be to determine the effect of cantilever approach speed for a colloidal probe (since the radius is well defined) interacting with a smooth surface like amorphous silica. Figure 7.1 shows an example setup of an AFM augmented with a fluid cell which allows for force and imaging experiments to be conducted while the experimental substrate and cantilever probe are submerged in a liquid.

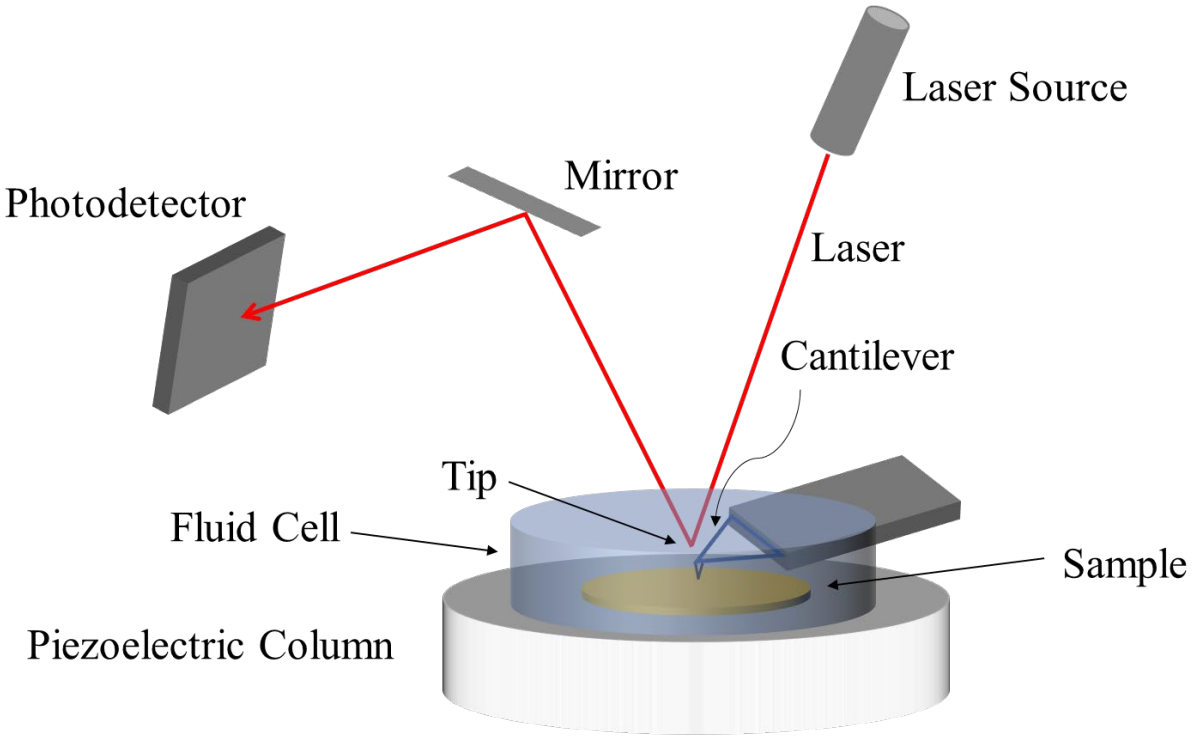

Figure 7.1 Schematic of an AFM augmented with a fluid cell which allows for force and imaging experiments to be conducted in a fluid environment.

Beyond applications to fluid environments, it would also be worthwhile to consider extending the method to analyzing deformable materials in, for example, biological and defense applications. For example, in biology, atomic force microscopy can be utilized to characterize biomechanical properties in cells as well as assess cell adhesion.[11] In the defense industry, there is a growing importance towards understanding how to accurately detect trace explosives that may appear on surfaces.[9] While some work has been done by Fronczak *et al.*[123] towards determining the Hamaker constant of trace explosives that include TNT and RDX, it would be of interest to experiment on these surfaces while taking surface roughness into consideration. Due to the deformable nature of cells and trace explosive residue, a reasonable attempt at quantifying the Hamaker constant from the modified approach-to-contact model could be made. However, a study will need to be made examining the impact of surface mechanics on contact deformation in order

to proceed because the deflection at first contact for deformable materials may be difficult to obtained accurately through experiments.

The impact of surface deformation could be directly incorporated into the approach-to-contact method through a contact mechanics model including the classic Hertz model describing the contact between two spheres or a sphere and a half space, as well as the JKR model which expands on the Hertz model and considers the adhesive contact between two surfaces.[87] A challenge in utilizing the approach-to-contact model for deformable surfaces lies in determining the deflection at contact experimentally. Figure 7.2 shows a representative force curve of an AFM cantilever approaching and contacting a deformable material. Unlike the solid materials discussed in this work, for which the maximum deflection of the cantilever is well defined, d_c may be more difficult to extract from experimental force curve data. The inclusion of contact models may be able to help predict the degree of deformation of the surface, leading to a more accurate determination of d_c. Regardless, experiments should be run at slow approach speeds to ensure minimal deformation of the surface.

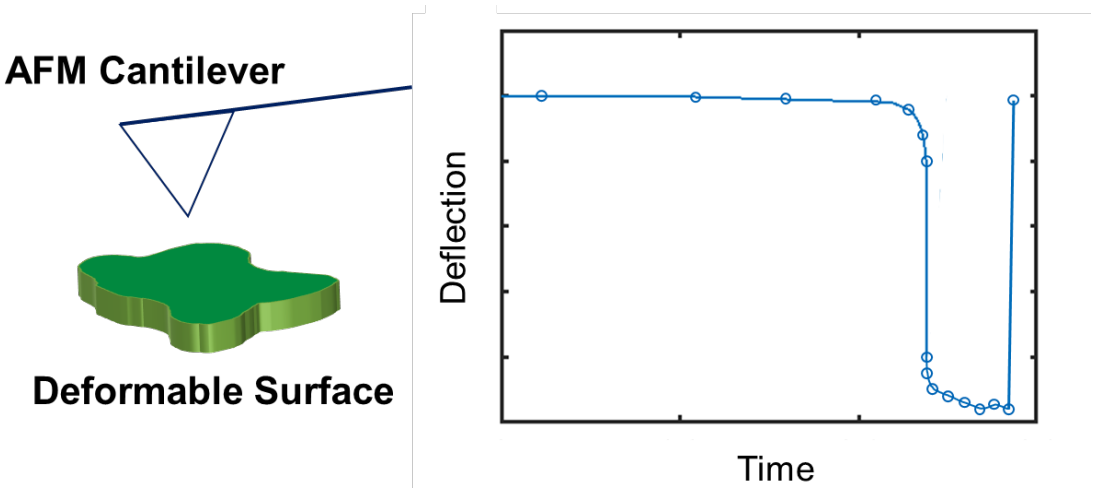

Figure 7.2 A representative force curve showing the deflection of the cantilever interacting with a deformable material.

Another future consideration includes the incorporation of surface roughness on the AFM cantilever, modeled in this work as a smooth sphere. Similarly to the surface height functions, roughness on the sphere would be modeled with a separate "height function", thereby requiring modification of the vdW force model developed in Chapter 2. The introduction of roughness on the sphere would further vary the vdW force as the sphere makes contact with different portions of the surface, as compared to the smooth sphere analysis. Figure 7.3 illustrates an example of a sphere, augmented with surface roughness, interacting with a (a) smooth and (b) rough plate. Depending on the relative size of the roughness on the surface of the sphere versus the surface, the magnitude of the vdW force, and in turn the deflection at contact, will either increase if the contact area increases, or decrease if the contact area decreases. For the surface height functions described in Chapter 3, the shape and magnitude of the resulting d_c-distributions will be influenced by the roughness scale on the sphere. Again, if the roughness scales are similar, higher deflections may be observed if the sphere and surface align in such a way that the contact area is larger (smaller deflections may also result if the area of contact deceases between the sphere and surface).

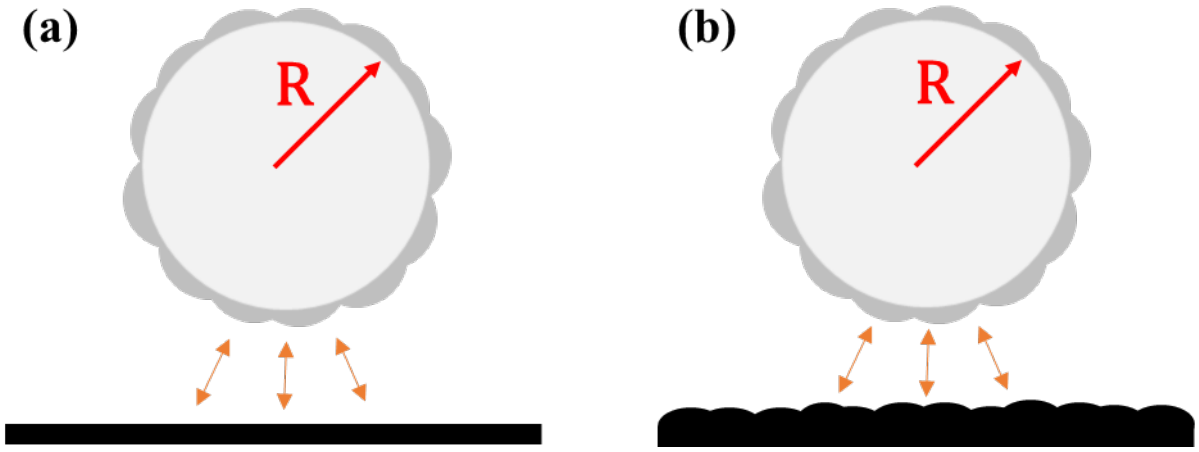

Figure 7.3 Illustration of a sphere, augmented with surface roughness, interacting with a (a) perfectly flat plate and (b) a plate with roughness.

The introduction of roughness on the sphere and extending the analysis to fluid environments as well as to deformable materials would provide a robust AFM based method to determine the self-Hamaker constant of a whole range of materials for a wide variety of applications.

REFERENCES

(1) Chattoraj, S.; Daugherity, P.; McDermott, T.; Olsofsky, A.; Roth, W. J.; Tobyn, M. Sticking and Picking in Pharmaceutical Tablet Compression: An IQ Consortium Review. *J. Pharm. Sci.* **2018**, *107* (9), 2267–2282.

(2) Bunker, M.; Zhang, J.; Blanchard, R.; Roberts, C. Characterising the Surface Behavior of Tablet Tooling Components by Atomic Force Microscopy. *Drug Dev. Ind. Pharm.* **2011**, *37* (8).

(3) Quesnel, D. J.; Rimai, D. S. Finite Element Modeling of Particle Adhesion: A Surface Energy Formalism. *J. Adhes.* **2000**, *74* (1–4), 177–194.

(4) Cabiscol, R.; Shi, H.; Wünsch, I.; Magnanimo, V.; Finke, J. H.; Luding, S.; Kwade, A. Effect of Particle Size on Powder Compaction and Tablet Strength Using Limestone. *Adv. Powder Technol.* **2020**, *31* (3), 1280–1289.

(5) Badal Tejedor, M.; Nordgren, N.; Schuleit, M.; Millqvist-Fureby, A.; Rutland, M. W. AFM Colloidal Probe Measurements Implicate Capillary Condensation in Punch-Particle Surface Interactions during Tableting. *Langmuir* **2017**, *33* (46), 13180–13188.

(6) Bowling, R. A. An Analysis of Particle Adhesion on Semiconductor Surfaces. *J. Electrochem. Soc. Solid State Sci. Technol.* **1985**, *132* (9), 2208–2214.

(7) Hattori, T. *Ultraclean Surface Processing of Silicon Wafers*; Springer-Verlag Berlin Heidelberg, 1995.

(8) Park, J.-G.; Lee, S.-H.; Ryu, J.-S.; Hong, Y.-K.; Kim, T.-G.; Busnaina, A. A. Interfacial and Electrokinetic Characterization of IPA Solutions Related to Semiconductor Wafer Drying and Cleaning. *J. Electrochem. Soc.* **2006**, *153* (9), G811.

(9) Chaffee-Cipich, M. N.; Sturtevant, B. D.; Beaudoin, S. P. Adhesion of Explosives. *Anal. Chem.* **2013**, *85* (11), 5358–5366.

(10) Christenson, H. K. DLVO (Derjaguin-Landau-Verwey-Overbeek) Theory and Solvation Forces between Mica Surfaces in Polar and Hydrogen-Bonding Liquids. *J. Chem. Soc. Faraday Trans. 1 Phys. Chem. Condens. Phases* **1984**, *80* (7), 1933–1946.

(11) Vahabi, S.; Nazemi Salman, B.; Javanmard, A. Atomic Force Microscopy Application in Biological Research: A Review Study. *Iran. J. Med. Sci.* **2013**, *38* (2), 76–83.

(12) Williamson, D. M.; Hamilton, N. R.; Palmer, S. J. P.; Jardine, A. P.; Leppard, C. Thermodynamic Work of Adhesion Measurements of Polymer Bonded Explosive Constituents via the Wilhelmy Plate Technique and Their Application to AFM Pull-off Experiments. *J. Phys. Conf. Ser.* **2014**, *500* (PART 11).

(13) Verkouteren, J. R.; Coleman, J. L.; Fletcher, R. A.; Smith, W. J.; Klouda, G. A.; Gillen, G. A Method to Determine Collection Efficiency of Particles by Swipe Sampling. *Meas. Sci. Technol.* **2008**, *19* (11).

(14) Heller, W.; Pugh, T. L. "Steric" Stabilization of Colloidal Solutions by Adsorption of Flexible Macromolecules. *J. Polym. Sci.* **1960**, *47* (149), 203–217.

(15) Verkouteren, J. R. Particle Characteristics of Trace High Explosives: RDX and PETN. *J. Forensic Sci.* **2007**, *52* (2), 335–340.

(16) Rhodes, M. *Introduction to Particle Technology*; John Wiley & Sons, Inc., 2008.

(17) Polizzi, M. A.; Franchville, J.; Hilden, J. L. Assessment and Predictive Modeling of Pharmaceutical Powder Flow Behavior in Small-Scale Hoppers. *Powder Technol.* **2016**, *294*, 30–42.

(18) Klinzing, G. E.; Rizk, F.; Marcus, R.; Leung, L. S. *Pneumatic Conveying of Solids: A Theoretical and Practical Approach*; Springer-Verlag Berlin Heidelberg, 2010.

(19) Knight, P. Challenges in Granulation Technology. *Powder Technol.* **2004**, *140* (3), 156–162.

(20) Liu, K. S. Some Factors Affecting Sieving Performance and Efficiency. *Powder Technol.* **2009**, *193* (2), 208–213.

(21) Mullins, M. E.; Michaels, L. P.; Menon, V.; Locke, B.; Ranade, M. B. Effect of Geometry on Particle Adhesion. *Aerosol Sci. Technol.* **1992**, *17* (2), 105–118.

(22) Perez-Gandarillas, L.; Perez-Gago, A.; Mazor, A.; Kleinebudde, P.; Lecoq, O.; Michrafy, A. Effect of Roll-Compaction and Milling Conditions on Granules and Tablet Properties. *Eur. J. Pharm. Biopharm.* **2016**, *106*, 38–49.

(23) Zinchuk, A. V.; Mullarney, M. P.; Hancock, B. C. Simulation of Roller Compaction Using a Laboratory Scale Compaction Simulator. *Int. J. Pharm.* **2004**, *269* (2), 403–415.

(24) Podczeck, F. *Particle-Particle Adhesion in Pharmaceutical Powder Handling*; Imperial College Press, 1998.

(25) Israelachvili, J. N. *Intermolecular and Surface Forces*, 3rd ed.; Elsevier, 2011.

(26) Butt, H. J.; Kappl, M. Normal Capillary Forces. *Adv. Colloid Interface Sci.* **2009**, *146* (1–2), 48–60.

(27) Gady, B.; Reifenberger, R.; Rimai, D. S.; DeMejo, L. P. Contact Electrification and the Interaction Force between a Micrometer-Size Polystyrene Sphere and a Graphite Surface. *Langmuir* **1997**, *13* (9), 2533–2537.

(28) Hartley, P. G.; Scales, P. J. Electrostatic Properties of Polyelectrolyte Modified Surfaces Studied by Direct Force Measurement. *Langmuir* **1998**, *14* (24), 6948–6955.

(29) Butt, H. J. Measuring Electrostatic, van Der Waals, and Hydration Forces in Electrolyte Solutions with an Atomic Force Microscope. *Biophys. J.* **1991**, *60* (6), 1438–1444.

(30) Krupp, H. Particle Adhesion Theory and Experiment. *Adv. Colloid Interface Sci.* **1967**, *1* (2), 111–239.

(31) Gillespie, T.; Settineri, W. J. The Effect of Capillary Liquid on the Force of Adhesion between Spherical Solid Particles. *J. Colloid Interface Sci.* **1967**, *24* (2), 199–202.

(32) Derjaguin, B. V.; Aleinikova, I. N.; Toporov, Y. P. On the Role of Electrostatic Forces in the Adhesion of Polymer Particles to Solid Surfaces. *Powder Technol.* **1969**, *2* (3), 154–158.

(33) Silberberg, M.; Amateis, P. *Chemistry: The Molecular Nature of Matter and Change*; McGraw-Hill Education, 2018.

(34) Cooper, K.; Gupta, A.; Beaudoin, S. Simulation of the Adhesion of Particles to Surfaces. *J. Colloid Interface Sci.* **2001**, *234* (2), 284–292.

(35) Hamaker, H. C. The London-Van Der Waals Attraction Between Sphereical Particles. **1937**, No. 1.

(36) London, F. The General Theory o f Molecular Forces. *Trans. Faraday Soc.* **1937**, *33* (8), 8–26.

(37) Reilly, A. M.; Tkatchenko, A. Van Der Waals Dispersion Interactions in Molecular Materials: Beyond Pairwise Additivity. *Chem. Sci.* **2015**, *6* (6), 3289–3301.

(38) Hiemenz, P. C.; Rajagopalan, R. *Principles of Colloid and Surface Chemistry*, 3rd ed.; Marcel Dekker, Inc, 1997.

(39) Lifshitz, E. The Theory of Molecular Attractive Forces between Solids. *Sov. Phys. JETP* **1956**, *2* (l).

(40) Bergström, L. Hamaker Constants of Inorganic Materials. *Adv. Colloid Interface Sci.* **1997**, *70* (1–3), 125–169.

(41) Parsegian, V. A.; Weiss, G. H. Spectroscopic Parameters for Computation of van Der Waals Forces. *J. Colloid Interface Sci.* **1981**, *81* (1), 285–289.

(42) Hough, D. B.; White, L. R. The Calculation of Hamaker Constants from Liftshitz Theory with Applications to Wetting Phenomena. *Adv. Colloid Interface Sci.* **1980**, *14* (1), 3–41.

(43) Ackler, H. D.; French, R. H.; Chiang, Y. M. Comparisons of Hamaker Constants for Ceramic Systems with Intervening Vacuum or Water: From Force Laws and Physical Properties. *J. Colloid Interface Sci.* **1996**, *179* (2), 460–469.

(44) French, R. H.; Cannon, R. M.; DeNoyer, L. K.; Chiang, Y. M. Full Spectral Calculation of Non-Retarded Hamaker Constants for Ceramic Systems from Interband Transition Strengths. *Solid State Ionics* **1995**, *75* (C), 13–33.

(45) French, R. H.; Winey, K. I.; Yang, M. K.; Qiu, W. Optical Properties and van Der Waals-London Dispersion Interactions of Polystyrene Determined by Vacuum Ultraviolet Spectroscopy and Spectroscopic Ellipsometry. *Aust. J. Chem.* **2007**, *60* (4), 251–263.

(46) Binnig, G.; Quate, C. F.; Gi, E. L.; Gerber, C. Atomic Force Microscope.

(47) Martin, Y.; Wickramasinghe, H. K. Magnetic Imaging by “Force Microscopy” with 1000 Å Resolution. *Appl. Phys. Lett.* **1987**.

(48) Israelachvili, J.; Tabor, D. The Measurement of van Der Waals Dispersion Forces in the Range 1.5 to 130 Nm. *Proc. R. Soc. London A Math. Phys. Eng. Sci.* **1972**, *331* (1584), 19–38.

(49) Thomas, M. C.; Beaudoin, S. P. An Enhanced Centrifuge-Based Approach to Powder Characterization: Experimental and Theoretical Determination of a Size-Dependent Effective Hamaker Constant Distribution. *Powder Technol.* **2017**, *306*, 96–102.

(50) Owens, D. K.; Wendt, R. C. Estimation of the Surface Free Energy of Polymers. *J. Appl. Polym. Sci.* **1969**, *13* (8), 1741–1747.

(51) Kosgodagan Acharige, S.; Laurent, J.; Steinberger, A. Capillary Force on a Tilted Cylinder: Atomic Force Microscope (AFM) Measurements. *J. Colloid Interface Sci.* **2017**, *505*, 1118–1124.

(52) Korayem, M. H.; Kavousi, A.; Ebrahimi, N. Dynamic Analysis of Tapping-Mode AFM Considering Capillary Force Interactions. *Sci. Iran.* **2011**, *18* (1 B), 121–129.

(53) Jeffery, S.; Oral, A.; Pethica, J. B. Quantitative Electrostatic Force Measurement in AFM. *Appl. Surf. Sci.* **2000**, *157* (4), 280–284.

(54) Cheng, S.; Robbins, M. O. Capillary Adhesion at the Nanometer Scale. *Phys. Rev. E - Stat. Nonlinear, Soft Matter Phys.* **2014**, *89* (6), 1–14.

(55) Farshchi-Tabrizia, M.; Kappl, M.; Butt, H. J. Influence of Humidity on Adhesion: An Atomic Force Microscope Study. *J. Adhes. Sci. Technol.* **2008**, *22* (2), 181–203.

(56) Ando, Y. The Effect of Relative Humidity on Friction and Pull-off Forces Measured on Submicron-Size Asperity Arrays. *Wear* **2000**, *238* (1), 12–19.

(57) Yang, S.; Zhang, H.; Nosonovsky, M.; Chung, K. H. Effects of Contact Geometry on Pull-off Force Measurements with a Colloidal Probe. *Langmuir* **2008**, *24* (3), 743–748.

(58) Xiao, X.; Qian, L. Investigation of Humidity-Dependent Capillary Force. *Langmuir* **2000**, *16* (21), 8153–8158.

(59) Bachmann, D.; Hierold, C. Determination of Pull-off Forces of Textured Silicon Surfaces by AFM Force Curve Analysis. *J. Micromechanics Microengineering* **2007**, *17* (7), 1326–1333.

(60) Escobar, J. V.; Garza, C.; Castillo, R. Measuring Adhesion on Rough Surfaces Using Atomic Force Microscopy with a Liquid Probe. *Beilstein J. Nanotechnol.* **2017**, *8* (1), 84.

(61) Kumar, A.; Staedler, T.; Jiang, X. Role of Relative Size of Asperities and Adhering Particles on the Adhesion Force. *J. Colloid Interface Sci.* **2013**, *409*, 211–218.

(62) Frybort, S.; Obersriebnig, M.; Müller, U.; Gindl-Altmutter, W.; Konnerth, J. Variability in Surface Polarity of Wood by Means of AFM Adhesion Force Mapping. *Colloids Surfaces A Physicochem. Eng. Asp.* **2014**, *457* (1), 82–87.

(63) Jiang, Y.; Turner, K. T. Measurement of the Strength and Range of Adhesion Using Atomic Force Microscopy. *Extrem. Mech. Lett.* **2016**, *9*, 119–126.

(64) Ducker WA; Senden TJ; Pashley PA. Direct Measurement of Colloidal Forces Using an Atomic Force Microscope. *Nature* **1991**, *353* (353), 2239.

(65) Schaefer, D. M.; Carpenter, M.; Reifenberger, R.; Demejo, L. P.; Rimai, D. S. Surface Force Interactions between Micrometer-Size Polystyrene Spheres and Silicon Substrates Using Atomic Force Techniques. *J. Adhes. Sci. Technol.* **1994**, *8* (3), 197–210.

(66) Lomboy, G.; Sundararajan, S.; Wang, K.; Subramaniam, S. A Test Method for Determining Adhesion Forces and Hamaker Constants of Cementitious Materials Using Atomic Force Microscopy. *Cem. Concr. Res.* **2011**, *41* (11), 1157–1166.

(67) Beach, E. R.; Tormoen, G. W.; Drelich, J.; Han, R. Pull-off Force Measurements between Rough Surfaces by Atomic Force Microscopy. *J. Colloid Interface Sci.* **2002**, *247* (1), 84–99.

(68) Tormoen, G. W.; Drelich, J.; Nalaskowski, J. A Distribution of AFM Pull-off Forces for Glass Microspheres on a Symmetrically Structured Rough Surface. *J. Adhes. Sci. Technol.* **2005**.

(69) Katainen, J.; Paajanen, M.; Ahtola, E.; Pore, V.; Lahtinen, J. Adhesion as an Interplay between Particle Size and Surface Roughness. *J. Colloid Interface Sci.* **2006**, *304* (2), 524–529.

(70) Hodges, C. S.; Cleaver, J. A. S.; Ghadiri, M.; Jones, R.; Pollock, H. M. Forces between Polystyrene Particles in Water Using the AFM: Pull-off Force vs Particle Size. *Langmuir* **2002**, *18* (15), 5741–5748.

(71) Jang, J.; Sung, J.; Schatz, G. C. Influence of Surface Roughness on the Pull-off Force in Atomic Force Microscopy. *J. Phys. Chem. C* **2007**, *111* (12), 4648–4654.

(72) Drelich, J.; Tormoen, G. W.; Beach, E. R. Determination of Solid Surface Tension from Particle-Substrate Pull-off Forces Measured with the Atomic Force Microscope. *Journal of Colloid and Interface Science*. 2004.

(73) Biggs, S.; Spinks, G. Atomic Force Microscopy Investigation of the Adhesion between a Single Polymer Sphere and a Flat Surface. *J. Adhes. Sci. Technol.* **1998**, *12* (5), 461–478.

(74) Weisenhorn, A. L.; Gotzos, V.; Butt, H.-J.; Khorsandi, M.; Kasas, S. Deformation and Height Anomaly of Soft Surfaces Studied with an AFM. *Nanotechnology* **2002**, *4* (2), 106–113.

(75) Butt, H. J.; Cappella, B.; Kappl, M. Force Measurements with the Atomic Force Microscope: Technique, Interpretation and Applications. *Surf. Sci. Rep.* **2005**.

(76) Gady, B.; Schleef, D.; Reifenberger, R.; Rimai, D. S. The Interaction between Micrometer-Size Particles and Flat Substrates: A Quantitative Study of Jump-to-Contact. *J. Adhes.* **1998**.

(77) Das, S.; Sreeram, P. A.; Raychaudhuri, A. K. A Method to Quantitatively Evaluate the Hamaker Constant Using the Jump-into-Contact Effect in Atomic Force Microscopy. *Nanotechnology* **2007**.

(78) Wu, J. J. The Jump-to-Contact Distance in Atomic Force Microscopy Measurement. *J. Adhes.* **2010**.

(79) Fronczak, S. G.; Dong, J.; Browne, C. A.; Krenek, E. C.; Franses, E. I.; Beaudoin, S. P.; Corti, D. S. A New "Quasi-Dynamic" Method for Determining the Hamaker Constant of Solids Using an Atomic Force Microscope. *Langmuir* **2017**, *33* (3), 714–725.

(80) Fronczak, S. G.; Browne, C. A.; Krenek, E. C.; Beaudoin, S. P.; Corti, D. S. Non-Contact AFM Measurement of the Hamaker Constants of Solids: Calibrating Cantilever Geometries. *J. Colloid Interface Sci.* **2018**, *517*, 213–220.

(81) Kindt, J. H.; Thompson, J. B.; Viani, M. B.; Hansma, P. K. Atomic Force Microscope Detector Drift Compensation by Correlation of Similar Traces Acquired at Different Setpoints. *Rev. Sci. Instrum.* **2002**, *73* (6), 2305–2307.

(82) Churnside, A. B.; Perkins, T. T. Ultrastable Atomic Force Microscopy: Improved Force and Positional Stability. *FEBS Lett.* **2014**, *588* (19), 3621–3630.

(83) Zhan, Z.; Yang, Y.; Li, W. J.; Dong, Z.; Qu, Y.; Wang, Y.; Zhou, L. AFM Operating-Drift Detection and Analyses Based on Automated Sequential Image Processing. *2007 7th IEEE Int. Conf. Nanotechnol. - IEEE-NANO 2007, Proc.* **2007**, No. d, 748–753.

(84) Husain, M.; Boudier, T.; Paul-Gilloteaux, P.; Casuso, I.; Scheuring, S. Software for Drift Compensation, Particle Tracking and Particle Analysis of High-Speed Atomic Force Microscopy Image Series. *J. Mol. Recognit.* **2012**, *25* (5), 292–298.

(85) Jaschke, M.; Butt, H. J. Calculation of Thermal Noise in Atomic Force Microscopy. *Nanotechnology* **1995**, *6* (1), 1–7.

(86) Freund, L.; Suresh, S. *Thin Film Materials: Stress, Defect Formation and Surface Evolution*; Cambridge University Press, 2004.

(87) Popov, V. L.; Heß, M.; Willert, E. *Handbook of Contact Mechanics*; 2019.

(88) Jaiswal, R. P.; Kumar, G.; Kilroy, C. M.; Beaudoin, S. P. Modeling and Validation of the van Der Waals Force During the Adhesion of Nanoscale Objects to Rough Surfaces: A Detailed Description. *Langmuir* **2009**, *25* (18), 10612–10623.

(89) Jaiswal, R. P. Adhesion between Particles and Nano-Structured Films, Purdue University, 2008.

(90) London, F. The General Theory of Molecular Forces. *Trans. Faraday Soc.* **1937**, *33*, 8b–26.

(91) Hamaker, H. C. The London-van Der Waals Attraction between Spherical Particles. *Physica* **1937**, *IV* (10), 1058–1072.

(92) Gradshteyn, I. S.; Ryzhik, I. M. *Table of Integrals, Series, and Products*; Academic Press: San Diego, CA, 1965.

(93) Gady, B.; Schleef, D.; Reifenberger, R.; Rimai, D.; DeMejo, L. Identification of Electrostatic and van Der Waals Interaction Forces between a Micrometer-Size Sphere and a Flat Substrate. *Phys. Rev. B - Condens. Matter Mater. Phys.* **1996**, *53* (12), 8065–8070.

(94) Fritzsche, J.; Peuker, U. A. Modeling Adhesive Force Distributions on Highly Rough Surfaces. *Powder Technol.* **2016**.

(95) Laitinen, O.; Bauer, K.; Niinimäki, J.; Peuker, U. A. Validity of the Rumpf and the Rabinovich Adhesion Force Models for Alumina Substrates with Nanoscale Roughness. *Powder Technol.* **2013**.

(96) Schaefer, D. M.; Carpenter, M.; Gady, B.; Reifenberger, R.; Demejo, L. P.; Rimai, D. S. Surface Roughness and Its Influence on Particle Adhesion Using Atomic Force Techniques. *J. Adhes. Sci. Technol.* **1995**, *9* (8), 1049–1062.

(97) Fuller, KNG, Tabor, F. The Effect of Surface Roughness on the Adhesion of Elastic Solids. *Proc R Soc L.* **1975**, *345*, 327–342.

(98) Eichenlaub, S.; Kumar, G.; Beaudoin, S. A Modeling Approach to Describe the Adhesion of Rough Asymmetric Particles to Surfaces. *J. Colloid Interface Sci.* **2006**, *299* (2), 656–664.

(99) Jaiswal, R. P.; Beaudoin, S. P. Approximate Scheme for Calculating van Der Waals Interactions between Finite Cylindrical Volume Elements. *Langmuir* **2012**, *28* (22), 8359–8370.

(100) Zill, D. G. *Advanced Engineering Mathematics*; Jones & Bartlett Learning, LLC, 2018.

(101) Stevenson, M. C.; Beaudoin, S. P.; Corti, D. S. Toward an Improved Method for Determining the Hamaker Constant of Solid Materials Using Atomic Force Microscopy. I. Quasi-Static Analysis for Arbitrary Surface Roughness. *J. Phys. Chem. C* **2019**.

(102) Leal, L. G. *Advanced Transport Phenomena*; Cambridge University Press: New York, 2007.

(103) Stevenson, M. C.; Beaudoin, S. P.; Corti, D. S. Toward an Improved Method for Determining the Hamaker Constant of Solid Materials Using Atomic Force Microscopy. II. Dynamic Analysis and Preliminary Validation. *J. Phys. Chem. C.*, In Review.

(104) Kullback, S.; Leibler, R. A. On Information and Sufficiency. *Ann. Math. Stat.* **1951**, 79–86.

(105) Kullback, S. *Information Theory and Statistics*; John Wiley & Sons, Inc., 1959.

(106) MacKay, D. J. C. *Information Theory, Inference and Learning Algorithms*; Cambridge University Press, 2003.

(107) Kurt, W. *Bayesian Statistics the Fun Way: Understanding Statistics and Probability with Star Wars, LEGO, and Rubber Ducks*; No Starch Press, 2019.

(108) Jaiswal, R. P.; Kumar, G.; Kilroy, C. M.; Beaudoin, S. P. Modeling and Validation of the van Der Waals Force During the Adhesion of Nanoscale Objects to Rough Surfaces: A Detailed Description. *Langmuir* **2009**, *25* (18), 10612–10623.

(109) Eichenlaub, S.; Gelb, A.; Beaudoin, S. Roughness Models for Particle Adhesion. *J. Colloid Interface Sci.* **2004**, *280* (2), 289–298.

(110) Smith III, J. *Mathematics of the Discrete Fourier Transform (DFT)*; W3K Publishing, 2008.

(111) Amidror, I. *Mastering the Discrete Fourier Transform in One, Two or Several Dimensions*; Springer-Verlag London, 2013.

(112) Ogunnaike, B. *Random Phenomena: Fundamentals of Probability and Statistics for Engineers*; Taylor & Francis Group, LLC, 2010.

(113) Dobryden, I.; Mensi, E.; Holmgren, A.; Almqvist, N. Surface Forces between Nanomagnetite and Silica in Aqueous Ca2+ Solutions Studied with Afm Colloidal Probe Method. *Colloids and Interfaces* **2020**, *4* (3).

(114) Sinha, P.; Szilagyi, I.; Montes Ruiz-Cabello, F. J.; Maroni, P.; Borkovec, M. Attractive Forces between Charged Colloidal Particles Induced by Multivalent Ions Revealed by Confronting Aggregation and Direct Force Measurements. *J. Phys. Chem. Lett.* **2013**, *4* (4), 648–652.

(115) Ruiz-Cabello, F. J. M.; Trefalt, G.; Csendes, Z.; Sinha, P.; Oncsik, T.; Szilagyi, I.; Maroni, P.; Borkovec, M. Predicting Aggregation Rates of Colloidal Particles from Direct Force Measurements. *J. Phys. Chem. B* **2013**, *117* (39), 11853–11862.

(116) Shi, Y.; Cai, M.; Zhou, L.; Wang, H. The Structure and Function of Cell Membranes Studied by Atomic Force Microscopy. *Semin. Cell Dev. Biol.* **2018**, *73*, 31–44.

(117) Braet, F.; Seynaeve, C.; De Zanger, R.; Wisse, E. Imaging Surface and Submembranous Structures with the Atomic Force Microscope: A Study on Living Cancer Cells, Fibroblasts and Macrophages. *J. Microsc.* **1998**, *190* (3), 328–338.

(118) Amarouch, M. Y.; El Hilaly, J.; Mazouzi, D. AFM and FluidFM Technologies: Recent Applications in Molecular and Cellular Biology. *Scanning* **2018**, *2018*.

(119) Parker, A. S.; Taylor, L. S.; Beaudoin, S. P. The Role of Surface Energy Heterogeneity on Crystal Morphology during Solid-State Crystallization at the Amorphous Atazanavir-Water Interface. *CrystEngComm* **2020**, *22* (18), 3179–3187.

(120) Moseson, D. E.; Parker, A. S.; Beaudoin, S. P.; Taylor, L. S. Amorphous Solid Dispersions Containing Residual Crystallinity: Influence of Seed Properties and Polymer Adsorption on Dissolution Performance. *Eur. J. Pharm. Sci.* **2020**, *146* (February), 105276.

(121) Wilkes, J. *Fluid Mechanics for Chemical Engineers*; Pearson Education Inc., 2006.

(122) Bird, B.; Stewart, W.; Lightfoot, E. *Transport Phenomena*; John Wiley & Sons, Inc., 2002.

(123) Fronczak, S. G. A New Method for Determining Hamaker Constants of Solids Based on the Dynamic Approach Behavior of an Atomic Force Microscope. Purdue Univesity, 2015.

APPENDIX: SELECTED MATLAB CODES

A1.1 Minimum Distance Method/QS/Dynamic Model MATLAB Code

```
%%%%%%%%%%%%%%%%%%%%%%%%%%%%%%%%%%%%%%%%%%%%%%%%%%%%%%%%%%%%%%%%%%%%%%%%%%%%
% This code utilizes the minimum distance method to determine the         %
% point of first contact between the cantilever (sphere) and surface      %
% for each point in an (xs,ys) matrix.  Upon determining the contact      %
% points, the code then calculates zs,crit, zp,crit, and dc,qs.  Then,    %
% a force matrix is generated, and the dynamic model is solved for the    %
% corresponding (xs,ys) points.                                           %
%                                                                         %
% In this example, the surface height function h(x,y) is defined as       %
% h(x,y) = cos(x) + cos(y).  The radius of the sphere is 1 micron and     %
% the cantilever velocity is 200 nm/s.                                    %
%                                                                         %
% This code can also be run to analyze surface height functions of        %
% the form h(x) (where y is constant along the entire surface).           %
%%%%%%%%%%%%%%%%%%%%%%%%%%%%%%%%%%%%%%%%%%%%%%%%%%%%%%%%%%%%%%%%%%%%%%%%%%%%

clear; clc
warning('off','all');

sphere_radius = 1; % Sphere radius, in microns
vc = 200E-9; % cantilever velocity, in nm/s
xs = linspace(0,2*pi(),30)/sphere_radius; % xs vector
ys = linspace(0,2*pi(),30)/sphere_radius; % ys vector

zpo = 10; % initial position of platform above surface
freq = 1; % wavelength component of surface height function
amplitude = 0.5; % amplitude component of surface height function

for rpq = 1:length(xs)
for pqr = 1:length(ys)
    % define vectors to evaluate surface height function over
    x_eval_sphere = linspace(xs(rpq)-1,xs(rpq)+1,2000);
    y_eval_sphere = linspace(ys(pqr)-1,ys(pqr)+1,2000);
    % grid of points to evaluate surface height function over
    [x_mesh,y_mesh] = meshgrid(x_eval_sphere,y_eval_sphere);
    % surface height function
    z_mesh = amplitude*cos(freq*x_mesh) + amplitude*cos(freq*y_mesh);
    % evaluate half-sphere at mesh points defined above
    z_sphere = zpo - sqrt(1-(x_mesh-xs(rpq)).^2-(y_mesh-ys(pqr)).^2);
    % remove imaginary values from z_sphere
    real_zsphere = real(z_sphere);
    % Calculate difference between surface and sphere and get min value
    % and location
    g_matrix = real_zsphere-z_mesh;
    [M_x,I_x] = min(min(g_matrix,[],1));
    [M_y,I_y] = min(min(g_matrix,[],2));
    % 1st point of contact on the surface - x
    x_contact(pqr,rpq) = x_eval_sphere(I_x);
    % 1st point of contact on the surface - y
```

```
    y_contact(pqr,rpq) = y_eval_sphere(I_y);
    % Define smaller x,y range and generate updated x,y contact points
    range_set = 1;
    lower_bound_x = x_eval_sphere(I_x-range_set);
    upper_bound_x = x_eval_sphere(I_x+range_set);
    lower_bound_y = y_eval_sphere(I_y-range_set);
    upper_bound_y = y_eval_sphere(I_y+range_set);

    x_eval_sphere_updated = linspace(lower_bound_x,upper_bound_x,1000);
    y_eval_sphere_updated = linspace(lower_bound_y,upper_bound_y,1000);
    [x_mesh_updated,y_mesh_updated] =
meshgrid(x_eval_sphere_updated,y_eval_sphere_updated);

    z_mesh_updated = amplitude*cos(freq*x_mesh_updated) +
amplitude*cos(freq*y_mesh_updated);

    z_sphere_updated = zpo - sqrt(1-(x_mesh_updated-xs(rpq)).^2-
(y_mesh_updated-ys(pqr)).^2);

    g_matrix_updated = real(z_sphere_updated)-z_mesh_updated;
    [M_x_updated,I_x_updated] = min(min(g_matrix_updated,[],1));
    [M_y_updated,I_y_updated] = min(min(g_matrix_updated,[],2));
    % Determine the x,y final contact points
    x_contact_updated(pqr,rpq) = x_eval_sphere_updated(I_x_updated);
    y_contact_updated(pqr,rpq) = y_eval_sphere_updated(I_y_updated);

    % Get zs,contact
    syms x y
    h = amplitude*cos(freq*x) + amplitude*cos(freq*y);
    % differentiate h with respect to x and y
    h_prime_x = diff(h,x);
    h_prime_y = diff(h,y);
    h_subs_1 = subs(h,x,x_contact_updated(pqr,rpq));
    h_subs_2 = subs(h_subs_1,y,y_contact_updated(pqr,rpq));
    h = double(h_subs_2);
    % Calculate zs,contact
    zs_contact_syms = h +
1./(1+(subs(h_prime_x,x,x_contact_updated(pqr,rpq))).^2+...
        (subs(h_prime_y,y,y_contact_updated(pqr,rpq))).^2).^0.5;
    zs_contact(pqr,rpq) = double(zs_contact_syms);
end
end

% Get zs,crit
R  = sphere_radius*1E-6; % Sphere radius in m
A  = 1.0E-19; % Hamaker constant in J
kc = 0.1; % Cantilever spring constant in N/m
res_freq = 38e3; % Resonant frequency in kHz
m  = kc /(res_freq*2*pi())^2;  % cantilever mass in kg
b = 1; % integral bounds

syms zs_crit
syms x y

% for each xs, ys, determine zs,crit
```

```
for j = 1:length(xs)
for i = 1:length(ys)
    eqn3 = @(zs_crit) simp2D(@(x,y) (8/pi())*(A/kc/R^2).*(zs_crit-...
        (amplitude*cos(freq*x) + amplitude*cos(freq*y)).*((x-xs(j)).^2+...
        (y-ys(i)).^2+((amplitude*cos(freq*x) + amplitude*cos(freq*y)))-...
        zs_crit).^2-1).^(-4), xs(j)-b, xs(j)+b, ys(i)-b, ys(i)+...
        b,1000,1000) - 1;
    options = optimoptions('fsolve', 'OptimalityTolerance', 1E-20, 'Display',
'off');
    eqn_int(j,i) = fsolve(@(zs_crit) eqn3(zs_crit), zs_contact(j,i)+.1,
options);
    zs_crit_vect(j,i) = eqn_int(j,i);
    disp(i)
end
end

% for each xs, ys, determine zp,crit
syms zp_crit
for j = 1:length(xs)
for i = 1:length(ys)
    eqn4 = @(zp_crit) simp2D(@(x,y) -(4/3/pi()).*(A/kc/R^2).*((x-
xs(j)).^2+...
        (y-ys(i)).^2+((amplitude*cos(freq*x) +amplitude*cos(freq*y))...
        -zs_crit_vect(j,i)).^2-1).^(-3),xs(j)-b, xs(j)+b, ys(i)-b, ys(i)...
        +b,1000,1000) - zs_crit_vect(j,i) + zp_crit - 1;
    options = optimoptions('fsolve', 'OptimalityTolerance', 1E-20, 'Display',
'off');
    eqn_int2(j,i) = fsolve(@(zp_crit) eqn4(zp_crit), zs_crit_vect(j,i)+2,
options);
    zp_crit_vect(j,i) = eqn_int2(j,i);
    disp(i)
end
end
% In the quasi-static limit, zp,contact = zp,crit
zp_contact_vect = zp_crit_vect;
% Determine dc,qs
dc_quasi_static_mat = -(zp_contact_vect - zs_contact - 1);

% Generate force matrix needed to solve the dynamic model
zMax = zpo; % Starting point above the surface of the sphere

% Generate values for gInt which is the "integrating function" that will
% be interpolated when solving the ODE
zStepSize = 0.001; % Step size of the integrating function
for jj = 1:length(xs)
    for ii = 1:length(ys)
        zMin(jj,ii) = zs_contact(jj,ii); % Point at which the sphere touches
the surface
        zStepCount(jj,ii) = round((zMax-zMin(jj,ii))/zStepSize,0);
    end
end
% Find max size of matrix
max_size = max(max(zStepCount));
Force_Matrix = zeros(max_size,2*length(xs)*length(ys));
count = 1;
% Numerical Integration of "full expression" with pre-factors
```

```
for jj = 1:length(xs)
    for ii = 1:length(ys)
        for nn=1:(zStepCount(ii,jj))
            zVal = zMin(ii,jj) + nn*zStepSize;
            f = @(q,p) (-4/3/pi())*(A/kc/R^2)*((q-xs(jj)).^2+(p-
ys(ii)).^2+...
                ((amplitude*cos(freq*q) + amplitude*cos(freq*p))-zVal).^2-
1).^(-3);
            a = quad2d(f, xs(jj)-1, xs(jj)+1, ys(ii)-1, ys(ii)+1,'RelTol',
1E-8, 'AbsTol', 1E-8) ;
            Force_Matrix(nn,count) = zVal; % Step
            Force_Matrix(nn,count+1)= a; % Value @step
        end
        count = count + 2;
    end
end

count = 1;
% Solve the dynamic model at each xs,ys
for mm = 1:length(xs)
    for n = 1:length(ys)
        b = 1;
        astar = vc*sqrt(m)/(R*sqrt(kc)); %SCALED %For use in the ODE
        bstar = A/(kc*R^2)/pi(); %SCALED %For use in the ODE
        % Simulation stops here (overall)
        Tfinal = ((zpo-zs_contact(n,mm)-1)*R/vc)*2*pi()*res_freq;

        % Intital mechanical equilibirum, Solve force balance for F_NET = 0
        syms zs_scaled_stat
        eqn5 = @(zs_scaled_stat) simp2D(@(x,y) -(4/3/pi()).*(A/kc/R^2).*...
            ((x-xs(mm)).^2+(y-ys(n)).^2+((amplitude.*cos(freq.*x) +...
            amplitude.*cos(freq.*y))-zs_scaled_stat).^2-1).^(-3),xs(mm)-b,...
            xs(mm)+b, ys(n)-b, ys(n)+b,1000,1000) - zs_scaled_stat + zpo - 1;
        options = optimoptions('fsolve', 'OptimalityTolerance', 1E-10,
'Display', 'iter','Display', 'off');
        eqn_int3 = fsolve(@(zs_scaled_stat) eqn5(zs_scaled_stat), zpo,
options);
        zs_scaled_stat = eqn_int3;
        Initial_Position = zs_scaled_stat;
        Initial_Velocity = -astar;
        Initial_Timestart = 0;
        Initial_Timeend = Tfinal;
        tolerance = 1E-20;
        t = []; % Initialize empty vector t
        y = []; % Same for y
        Timestart = Initial_Timestart;
        Timeend   = Tfinal;
        % RUN ODE
        % ODE Settings - Vary with time/position
        tSpan= [Timestart,Timeend]; % Time interval with time step
        InitialConditions    =   zeros(2,1);
        InitialConditions(1) =   Initial_Position; % Position or zs
        InitialConditions(2) =   Initial_Velocity; % Velocity or slope

        options = odeset('RelTol', tolerance, 'AbsTol',[tolerance
tolerance]);
```

```
        % Note: a is time (t) and b is position/velocity (y)
        g1 = nonzeros(Force_Matrix(:,count));
        g1 = [zs_contact(n,mm);g1];
        count = count + 1;
        g2 = nonzeros(Force_Matrix(:,count));
        g2 = 1./g2;
        g2 = [0;g2];
        g = [g1,g2];
        % Solve using ode23t
        [a,b] = ode23t(@(a,b)
odefunction(a,b,zpo,astar,g),tSpan,InitialConditions,options);
        t = [t,a']; % Add latest run to overall t vector
        y = [y,b']; % Add latest run to overlal y vector
        % Scenario One: Just "Jump to Final Contact"
        % Correct for contact @ final point
        t_jump = a;
        y_jump = b;
        % add last time point to t for instanenous jump
        last_tp = t(end);
        t_jump(end+1) = t(end);
        y_jump(end+1,1) = zs_contact(n,mm);
        zp_end = zpo -(vc/R*sqrt(m/kc))*t_jump(end);
        dc_instant_jump = (y_jump(end,1)-zp_end+1)*R*1E9;
        y_jump(end,2) = dc_instant_jump;
        % Scenario Two: Cantilever travels at last velocity until
        % making contact with surface
        t_velocity = t;
        y_velocity = y;
        velocity = y_velocity(2,end);
        dist_1 = y_velocity(1,end);
        dist_2 = zs_contact(n,mm);
        delta_d = abs(dist_2-dist_1);
        timeframe = delta_d/(-1*y_velocity(2,end));
        y_velocity(1,end+1) = zs_contact(n,mm);
        y_velocity(2,end) = y_velocity(2,end-1);
        zp_end2 = zpo -(vc/R*sqrt(m/kc))*t_velocity(end) -
(vc/R*sqrt(m/kc))*timeframe;
        dc_velocity = (y_velocity(1,end)-zp_end2+1)*R*1E9;
        dc_SIM_FINAL = (dc_instant_jump+dc_velocity)/2;
        dc_SIM_FINAL_vector(n,mm) = dc_SIM_FINAL;
        count = count + 1;
        zpstar = zpo-(vc/R*sqrt(m/kc))*t;
        dc = (b(:,1)-zpstar'+1)*R;
        dc(end+1) = dc_SIM_FINAL/1E9;
        t_reg = sqrt(m/kc)*t_jump;
        clear zs_scaled_stat a b g
    end
end
```

A1.2 odefunction MATLAB Code

```
%%%%%%%%%%%%%%%%%%%%%%%%%%%%%%%%%%%%%%%%%%%%%%%%%%%%%%%%%%%%%%%%%%%%%%%%%%%%
% This code accompanies the MDM/QS/dynamic model code.  This function    %
% utilizes an interpolating scheme to solve the ODE at the points        %
% defined in the force matrix, g.  The function decomposes the ODE into  %
% a series of first order ODES.                                          %
%%%%%%%%%%%%%%%%%%%%%%%%%%%%%%%%%%%%%%%%%%%%%%%%%%%%%%%%%%%%%%%%%%%%%%%%%%%%

function dydt = odefunction(a,b,zpo,astar,g)
dydt = zeros(2,1);
gInt = interp1(g(:,1),g(:,2),b(1),'pchip');
dydt(1)= b(2);
dydt(2) = (1./gInt)-b(1)-astar*a+zpo-1;
end
```

A1.3 Surface Reconstruction MATLAB Code

```
%%%%%%%%%%%%%%%%%%%%%%%%%%%%%%%%%%%%%%%%%%%%%%%%%%%%%%%%%%%%%%%%%%%%%%%%%%%%
% This code generates representative surface scans via a discrete        %
% Fourier transform algorithm. An n by n surface is first loaded and     %
% normalized by the mean.  Then the DFT is taken and the frequency       %
% components are randomized based on the chosen cut-off value.  The new  %
% surface is then generated by performing an inverse DFT and the         %
% corresponding amplitude spectrum is outputted, along with a mesh       %
% plot of the two surfaces.                                              %
%%%%%%%%%%%%%%%%%%%%%%%%%%%%%%%%%%%%%%%%%%%%%%%%%%%%%%%%%%%%%%%%%%%%%%%%%%%%

clear all; close all; clc;

data = load('Raw_data.txt'); % load raw data from AFM surface scan
scan_size = 10; % select scan size, in microns
points = 512; % select number of points comprising the data matrix
matrix_size = sqrt(length(data)); % finds the size of the square image
% creates a matrix of zeros as large as image size
data_matrix = zeros([matrix_size, matrix_size]);

k = 1; % indexes position in column file

for i = 1:1:matrix_size % x direction
    for j = 1:1:matrix_size % y direction
        data_matrix(i,j) = data(k); % assigns
        k = k + 1;
    end
end
% normalize by the mean
data_matrix = data_matrix + abs(min(min(data_matrix)));
data_matrix = data_matrix/1000;

cutoff = 20; % select a cut-off value for the wavelength components
N = length(data_matrix); % window length/data length
Y1_o = fft2(data_matrix)/(N*N); % take fft
N1 = ceil(N/2);

nc = Y1_o(2:points, 2:points);
zf_new = zeros(points-1,points-1);

% Generate conjugate pairs
lower = tril(nc);
for xx = 1:points-1
    for yy = 1:points-1
        if xx == yy
            continue
        else
            rand_phi = rand(1,1)*2*pi();
            phase_shift = rand_phi;
            shift = -phase_shift/(2*pi())*N;
            w = 2*pi()/N*(yy);
            w = 1;
            if xx || yy > cutoff
                shift = 0;
```

```
            end
            zf_new(yy,xx) = nc(yy,xx) * exp(-1i*shift*w);
        end
    end
end
zf_new = tril(zf_new);
for xx = 1:(points/2)-1
    for yy = 1:(points/2)-1
        if xx == yy
            rand_phi = rand(1,1)*2*pi();
            phase_shift = rand_phi;
            shift = -phase_shift/(2*pi())*N;
            w = 2*pi()/N*(yy);
            w = 1;
            if xx > cutoff
                shift = 0;
            end
            zf_new(yy,xx) = nc(yy,xx) * exp(-1i*shift*w);
        end
    end
end
zf_new(points/2,points/2) = nc(points/2,points/2);
space = 2;
for xx = (points/2)+1:points-1
    for yy = (points/2)+1:points-1
        if xx == yy
            zf_new(xx,yy) = conj(zf_new(xx-space,yy-space));
            space = space + 2;
        end
    end
end

for xx = 1:points-1
    for yy = 1:points-1
        if xx == yy
            continue
        else
            zf_new_hold(xx,yy) = conj(zf_new(points-xx,points-yy));
        end
    end
end

for xx = 1:points-1
    for yy = 1:points-1
        if xx == yy
            continue
        else
            zf_new(xx,yy) = zf_new(xx,yy) + zf_new_hold(xx,yy);
        end
    end
end

temp = Y1_o;
for ii = 2:points
    for jj = 2:points
        temp(ii,jj) = 0;
```

```
    end
end
for yy = 2:points
    for xx = 2:points
        temp(yy,xx) = zf_new(yy-1,xx-1);
    end
end
zf_new = temp;
% generate random for the first row and columns leaving (1,1) unchanged
for yy = 2:points/2
    rand_phi = rand(1,1)*2*pi();
    phase_shift = rand_phi;
    shift = -phase_shift/(2*pi())*N;
    w = 2*pi()/N*(yy);
    w = 1;
    if yy > cutoff
        shift = 0;
    end
    temp_first_row(1,yy) = Y1_o(1,yy) * exp(-1i*shift*w);
end
temp_imag_first_row = -imag(flip(temp_first_row(2:end)));
temp_real_first_row = real(flip(temp_first_row(2:end)));
temp_complex_first_row = complex(temp_real_first_row,temp_imag_first_row);
first_row = [temp_first_row Y1_o(1,(points/2)+1) temp_complex_first_row];

for zz = 2:points/2
    rand_phi = rand(1,1)*2*pi();
    phase_shift = rand_phi;
    shift = -phase_shift/(2*pi())*N;
    w = 2*pi()/N*(yy);
    w = 1;
    if zz > cutoff
        shift = 0;
    end
    temp_first_column(zz,1) = Y1_o(zz,1) * exp(-1i*shift*w);
end
temp_imag_first_column = -imag(flip(temp_first_column(2:end)));
temp_real_first_column = real(flip(temp_first_column(2:end)));
temp_complex_first_column = complex(temp_real_first_column,...
    temp_imag_first_column);
first_column = [temp_first_column; Y1_o((points/2)+1,1);...
    temp_complex_first_column];

first_element = Y1_o(1,1);
first_mid_row_element = Y1_o(1,(points/2)+1);
first_mid_column_element = Y1_o((points/2)+1,1);

zf_new(1,:) = first_row;
zf_new(:,1) = first_column;
zf_new(1,1) = first_element;
% final surface
Y1 = real(ifft2(zf_new))*(N*N);
% check the RMS of the original and new surfaces
RMS_original = std(data_matrix,0,'all');
RMS_new = std(Y1,0,'all');
NN = linspace(1,points,points);
```

```
amplitudes_original = abs(Y1_o);
amplitudes_new = abs(zf_new);
difference = amplitudes_original-amplitudes_new;
% generate the amplitude spectrum
figure(1)
stem3(NN(1:points/2)-1,NN(1:points/2)-1,2*...
    amplitudes_original(1:points/2,1:points/2))
xlabel('u')
ylabel('v')
zlabel('Amplitude')
set(gcf,'color','w');
title('Amplitude Spectrum')
% generate a mesh plot showing both surfaces
figure(2)
mesh(x_mesh,y_mesh,data_matrix, 'EdgeColor','#CDCAC9')
xlabel('x (\mum)')
ylabel('y (\mum)')
zlabel('z (nm)')
set(gcf,'color','w');
hold on
mesh(x_mesh,y_mesh,Y1)
xlabel('x (\mum)')
ylabel('y (\mum)')
zlabel('z (nm)')
set(gcf,'color','w');
```